

10-7-2020 2:30 PM

## Material Properties and Heat Transfer Parameters in Compression Molding of Glass Mat Thermoplastics

Cheng Xu, *The University of Western Ontario*

Supervisor: Hrymak, Andrew N., *The University of Western Ontario*

Co-Supervisor: Henning, Frank, *Karlsruhe Institute of Technology*

A thesis submitted in partial fulfillment of the requirements for the Master of Engineering Science degree in Chemical and Biochemical Engineering

© Cheng Xu 2020

Follow this and additional works at: <https://ir.lib.uwo.ca/etd>



Part of the [Chemical Engineering Commons](#), and the [Materials Science and Engineering Commons](#)

---

### Recommended Citation

Xu, Cheng, "Material Properties and Heat Transfer Parameters in Compression Molding of Glass Mat Thermoplastics" (2020). *Electronic Thesis and Dissertation Repository*. 7436.  
<https://ir.lib.uwo.ca/etd/7436>

This Dissertation/Thesis is brought to you for free and open access by Scholarship@Western. It has been accepted for inclusion in Electronic Thesis and Dissertation Repository by an authorized administrator of Scholarship@Western. For more information, please contact [wlsadmin@uwo.ca](mailto:wlsadmin@uwo.ca).

# Abstract

The compression molding of glass mat thermoplastics (GMT) allows high volume manufacture of composite parts with a short production cycle. Computer simulation is often used to assist process development and optimization. Reliable simulation depends on input of material property parameters and accurate prediction of heat transfer. This thesis developed experimental methods to characterize material property and heat transfer process parameters. Results were obtained by applying the methods to a selected commercial GMT sheet. Heat transfer coefficients including convection coefficients during pre-heating and transfer, as well as contact conductance at sheet-mold interface were estimated by a parameter-fitting approach. Viscoelastic parameters of the composite were characterized by oscillatory torsion bar, which can be used to model the draping behavior. The elastic modulus and viscosity were fitted by a Williams-Landel-Ferry (WLF) and Cross-WLF model, respectively. Flow behavior of a stacked charge was also characterized by a 1-D squeeze flow model, where the apparent viscosity was fitted by a temperature dependent power-law model.

## Keywords

Glass mat thermoplastic, compression molding, material characterization, heat transfer, draping, squeeze flow

## Summary for Lay Audience

In the automotive industry, light-weighting has become one of the top priorities as it provides better fuel efficiency and handling. Polymer composites are widely used in car manufacturing for this purpose. In general, it refers to a material that is composed of a polymer matrix (e.g. PP, PA) and fiber reinforcement (e.g. glass or carbon fiber). Automobile parts made of polymer composites not only enables light-weighting, but also possesses good mechanical strength. The process of forming raw composite material into desired part geometry is called molding. Various molding techniques have been developed, such as the compression molding, the resin transfer molding or the thermoforming.

To build a molding process for part production, it is often required to also establish a continuous and functional virtual process chain by means of computer simulation. Simulation results may accelerate and optimize the development of real process chain. One of the keys to reliable simulation output is the accurate input parameters. In terms of molding simulations, these parameters include material properties and heat transfer coefficients. Therefore, the characterization of these parameters is increasingly gaining interest by the industry.

## Co-Authorship Statement

Chapter 3 of this thesis was reproduced from a conference publication. The abstract of the paper was accepted at SPE ACCE 2020. The full paper has been submitted and is currently under review. The title of the paper, the names of the co-authors and the contribution made by each co-author are listed below.

**Title:** CHARACTERIZATION OF HEAT TRANSFER PARAMETERS IN THE COMPRESSION MOLDING OF GLASS MAT THERMOPLASTICS

**Submitted to:** SPE ACCE 2020

**Authors:** Cheng Xu, Stanislav Ivanov, Ryan Gergely, Dominik Dörr, Andrew Hrymak, Frank Henning

**Contributions:** Cheng Xu, Stanislav Ivanov, Dominik Dörr and Prof. Hrymak discussed and developed the experimental method presented in the paper. Stanislav helped with the experimental set-ups using the equipment at Fraunhofer Project Center (FPC). Cheng carried out data recording, data analysis and paper draft writing. Prof. Hrymak, Prof. Henning and Ryan Gergely provided guidance and supports through the research process. They also provided comments for revisions made on the paper draft.

## Acknowledgments

First and foremost, I would like to thank my supervisor Prof. Andrew Hrymak, my co-supervisor Prof. Frank Henning for their patient guidance and wise suggestions on my works.

I would also like to thank Stanislav Ivanov, the research engineer at Fraunhofer Project Center (FPC), as well as all other staff at FPC for their help on conducting some of the experiments.

I would like to thank Ryan Gergely from General Motors for his advice on experimental works and results.

I would like to thank Dominik Dörr who helped with the development of some experimental design and the fitting of some experimental results.

Last but not least, I want to thank my parents for their continuous support on pursuing the master's degree.

# Table of Contents

Abstract .....	ii
Summary for Lay Audience.....	iii
Co-Authorship Statement.....	iv
Acknowledgments.....	v
Table of Contents .....	vi
List of Tables .....	ix
List of Figures .....	x
List of Appendices .....	xiv
Chapter 1 .....	1
1 Introduction .....	1
1.1 Background .....	1
1.2 Objectives .....	2
1.3 Thesis Structure .....	3
Chapter 2 .....	4
2 Review.....	4
2.1 Heat Transfer in Thermoplastic Composite Forming Process .....	4
2.2 Draping Behavior of Thermoplastic Composite Sheets.....	5
2.3 Flow Behavior of Thermoplastic Composites .....	11
Chapter 3 .....	16
3 Characterize Heat Transfer Parameters in Compression Molding of Glass Mat Thermoplastics .....	16
3.1 Methods.....	17
3.1.1 Materials and Sample Preparation .....	17
3.1.2 Experimental Set-up.....	19
3.1.3 Thermal Modeling .....	21

3.1.4	Parameter Estimation .....	25
3.1.5	Parameter Validation .....	29
3.2	Results and Discussion .....	29
3.2.1	Pre-Heating Stage .....	29
3.2.2	Cooling Stages .....	31
3.2.3	Estimated Parameters.....	33
3.3	Applications in Process Chain .....	34
3.4	Conclusions.....	37
Chapter 4.....		38
4	Material Characterization for Draping Simulations.....	38
4.1	Material and Property Anisotropy Examination .....	40
4.2	Sample Preparation and Experimental Procedures .....	44
4.3	Data Analysis .....	46
4.4	Characterization Results and Discussions .....	52
4.5	Generation of Material Cards.....	58
4.6	Comparison of Different Methods.....	61
4.7	Conclusions.....	63
Chapter 5.....		64
5	Material Characterization for Flow Simulations.....	64
5.1	Sample Preparation and Experimental Set-up .....	65
5.2	Data Analysis .....	66
5.3	Results and Discussion .....	70
5.4	Generation of Materials Cards .....	72
5.5	Conclusions.....	74
Chapter 6.....		76
6	Conclusions and Future Work.....	76

References .....	77
Appendices.....	84
Curriculum Vitae .....	86



## List of Tables

Table 3-1: Heat transfer types at sheet surfaces during each process stage.....	17
Table 3-2: Characteristics of Tepex Flowcore.....	18
Table 3-3: Rules for determining values of $n$ and $c$ .....	26
Table 3-4: Heat capacity of Tepex Flowcore measured at Moldex3D Material Testing Lab	27
Table 3-5: Thermal conductivity of Tepex Flowcore measured at Moldex3D Material Testing Lab .....	27
Table 3-6: Summary of estimated heat transfer parameters .....	34
Table 3-7: Simulated conditions and corresponding time to complete solidification after the mold closes.....	36
Table 4-1: After-flow dimensions measured in two objective directions.....	41
Table 4-2: Detailed test matrix for oscillatory torsion bar tests.....	45
Table 4-3: Results from all 90 direction specimens tested at 230 °C .....	52
Table 4-4: Fixed and fitted parameters used for elastic modulus and viscosity data .....	59
Table 4-5: Fitted parameters for 90 direction and 0 direction .....	61
Table 5-1: Test matrix of squeeze flow .....	66
Table 5-2: Fitted power-law parameters for all stack types and flow directions.....	74

## List of Figures

Figure 1-1: General stages of the compression molding process for thermoplastic composites .....	2
Figure 2-1: Deformation micro-mechanisms contributing to draping (left) intra-ply shear and (right) inter-ply friction [13] .....	6
Figure 2-2: Intra-ply shearing fixtures developed by (left) Haanappel et al. [17] and (right) Saches and Akkerman [24] .....	7
Figure 2-3: Abaqus simulation of the experiments in Figure 2-2 [25] .....	7
Figure 2-4: Torque vs. deformation angle curves for the GMT material in (left) torsion experiment and (right) bending experiment [5] .....	8
Figure 2-5: Experimental set-up developed by (left) Groves et al. [19] and (Right) Scherer et al. [26] .....	9
Figure 2-6: Experimental set-ups to measure tool-ply and inter-ply friction: (left) horizontal apparatus from TU Dresden and (right) vertical apparatus from University of Twente [28].	10
Figure 2-7: Ellipse formed by squeeze flow of anisotropic GMT materials (Dweib and O Br'adaigh [33]).....	12
Figure 2-8: The rheology tool developed by Hohberg et al. [24] .....	14
Figure 3-1: Thermocouple placement during consolidation of experimental samples.....	19
Figure 3-2: Forced convection oven (opened) .....	19
Figure 3-3: Flat mold used (bottom half).....	20
Figure 3-4: Experimental set-up to collect sample core temperature during (a) pre-heating stage (b) open-mold cooling stage and (c) closed-mold cooling stage .....	21
Figure 3-5: A section of the sample along x axis with thickness $\Delta x$ .....	22

Figure 3-6: Plot of heat capacity data in Table 3-4, peak indicates the recrystallization temperature range of the material .....	28
Figure 3-7: Abaqus simulation for open-mold cooling stage .....	28
Figure 3-8: Abaqus simulation of closed-mold cooling stage .....	29
Figure 3-9: Simulated core temperature compared with experimental core temperature during pre-heating stage (a) parameter estimation using 4-layer sample (b) parameter validation using 6-layer sample .....	30
Figure 3-10: Simulated core temperature compared with experimental core temperature during open-mold cooling stage (a) parameter estimation using 4-layer sample (b) parameter estimation using 6-layer sample.....	32
Figure 3-11: Simulated core temperature compared with experimental core temperature during closed-mold cooling stage (a) parameter estimation using 4-layer sample (b) parameter validation using 6-layer sample .....	33
Figure 3-12: Simulated through-thickness temperature profile for studied process conditions (a) single layer sample and 110 °C mold temperature (b) 3-layer sample and 110 °C mold temperature (c) 2-layer sample and 150 °C mold temperature (d) 2-layer and 70 °C mold ...	35
Figure 4-1: Draping and flowing phases of the compression molding process .....	38
Figure 4-2: Intra-ply shearing when material is draping [17] .....	38
Figure 4-3: Fixtures and specimens to characterize intra-ply shearing presented by (a) Saches et al. [24] and (b) Haanappel et al. [17] .....	39
Figure 4-4: Machine pattern on Tepex Flowcore and the two objective directions .....	40
Figure 4-5: Squeezed charge from test #1 .....	41
Figure 4-6: Fiber orientation distribution of Tepex Flowcore blank sheet.....	42

Figure 4-7: One of the micro-CT stitch images taken on the sample (view through the thickness) .....	42
Figure 4-8: Two intra-ply shearing mechanisms distinguished by (a) longitudinal shearing and (b) transversal shearing .....	43
Figure 4-9: Torsion bar specimen dimensions.....	44
Figure 4-10: (Left) picture of sample being installed on the fixtures, (Right) equipment schematic drawing reproduced from the user manual .....	44
Figure 4-11: Example strain and stress data collected from experiments .....	46
Figure 4-12: Stress against strain plot using data from Figure 4-11 .....	48
Figure 4-13: Stress against strain rate plot using data from Figure 4-11 .....	48
Figure 4-14: Elastic stress decomposed from Figure 4-12 using equation 4.6.....	49
Figure 4-15: Viscous Stress decomposed form Figure 4-13 using equation 4.7 .....	50
Figure 4-16: Elastic modulus characterized for 0 and 90 direction samples under (a) 230 °C (b) 250 °C and (c) 260 °C.....	53
Figure 4-17: Temperature dependency of elastic modulus on (a) 90 direction specimen and (b) 0 direction specimen.....	55
Figure 4-18: Viscosities characterized for 0 and 90 direction samples under (a) 230 °C (b) 250 °C and (c) 260 °C .....	56
Figure 4-19: Temperature dependency of viscosity on (a) 90 direction specimen and (b) 0 direction specimen .....	57
Figure 4-20: Fitting of 0 direction properties (left) Cross-WLF for viscosity and (right) WLF for elastic modulus .....	60
Figure 4-21: Fitting of 90 direction properties (left) Cross-WLF for viscosity and (right) WLF for elastic modulus .....	60

Figure 4-22: Comparison of elastic modulus with RB test.....	62
Figure 4-23: Comparison of viscosity with RB test.....	62
Figure 5-1: 1-D flow characterization set-up developed by Kalaidov et al. [57] .....	64
Figure 5-2: Experimental set-up for 1-D squeeze flow of Tepex Flowcore .....	65
Figure 5-3: Example data sets collected from press during squeeze flow experiments .....	67
Figure 5-4: Coordinates and variables in the 1-D flow problem .....	68
Figure 5-5: Newtonian (red) and non-Newtonian (blue) velocity profiles at flow front during squeeze flow.....	69
Figure 5-6: Press viscosity estimation using the data in Figure 5-3 .....	69
Figure 5-7: Summary of press viscosity at all tested conditions (a) 300 °C and (b) 260 °C...	70
Figure 5-8: Frictional interfaces in a 6x2 (6-layer) stack .....	71
Figure 5-9: Temperature dependency of press viscosity (a) 90 direction (b) 0 direction.....	72
Figure 5-10: Fitted power-law curves for 4x3 stack charge in 90 direction.....	74

## List of Appendices

Appendix A: Temperature dependency (normal scale) of elastic modulus characterized from torsion bar (a) 90 direction and (b) 0 direction .....	84
Appendix B: Temperature dependency (normal scale) of viscosity characterized from torsion bar (a) 90 direction and (b) 0 direction .....	85

# Chapter 1

## 1 Introduction

### 1.1 Background

In the modern automotive industry, polymer composites have been widely used in automobile parts, which enables light-weighting while still maintaining required performance properties. Glass mat thermoplastic (GMT) composites are a widely chosen material category for this purpose. In general, GMT describes sheet-like composites with chopped, randomly oriented fiber reinforcement in a thermoplastic polymer matrix. This type of material system, when compared to alternatives such as sheet molding compounds (SMC) and thermoplastic pellets, possesses the feature of both a re-meltable matrix and potentially long-fiber reinforcement. Usually, compression molding, resin transfer molding or thermoforming can be used to process the material into desired parts [1], [2]. Of all these forming techniques, compression molding offers the highest potential to preserve the long fibers and thus lead to better mechanical property of the part [3], [4]. Furthermore, the combination of compression molding and GMT material allows high-volume manufacturing with cycle times on the order of one minute. The compression molding process for thermoplastic composites generally consists of the following stages in sequence: the preheating of charge to its molten state, the transfer of charge, the placement of charge, and the forming of parts. The mold is usually controlled at a much lower temperature than the recrystallization temperature of the composite. Therefore, after forming, the part stays in the mold for an extended amount of time until it vitrifies. Afterwards, the molds open and the part is taken out. Figure 1-1 gives a graphical illustration of the stages.

The development of a process chain for the mass production of thermoplastic composite parts is a complex task. Often, it is required to establish a continuous and functional virtual process chain by means of computer simulation, including Computer Aided Engineering (CAE) or Computational Fluid Dynamics (CFD) software. With the help of this virtual twin, development of the real process chain can be accelerated and optimized

[5]. Reliable simulation results depend not only on the selection of the appropriate thermomechanical model, but also the input of accurate material and process model parameters. Therefore, the characterization of these parameters is increasingly gaining interest in terms of industrial application. In terms of thermoplastic composite compression molding processes two perspectives are considered — the thermal and the mechanical. From the thermal perspective, heat transfer parameters between the charge and the environment/tool help to model charge temperature evolution during the molding process. The use of material mechanical properties allows prediction of deformation behavior when the charge is molded.

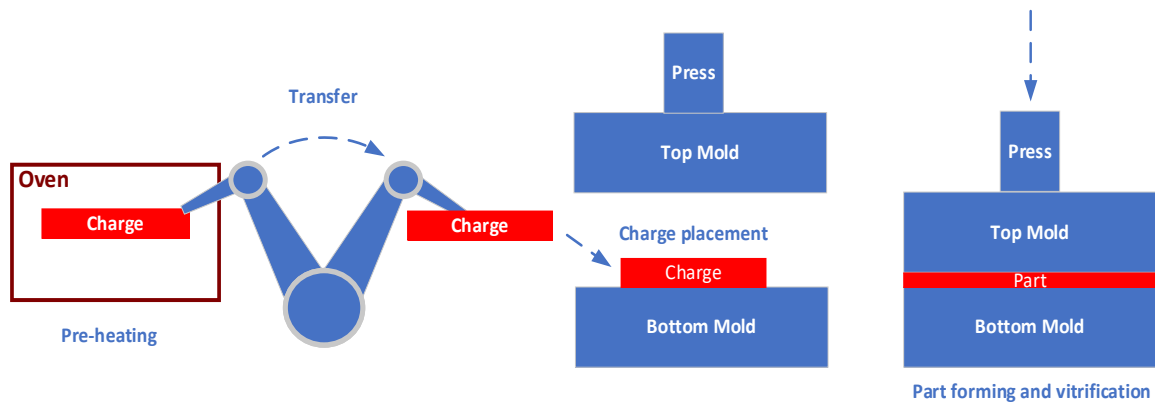


**Figure 1-1: General stages of the compression molding process for thermoplastic composites**

## 1.2 Objectives

This thesis aims at developing experimental methods to characterize the heat transfer parameters during the compression molding process, as well as the mechanical properties of GMT materials in the deformable state (prior to vitrification). The combined heat transfer and the material property parameter sets serve as inputs for numerical simulation of the GMT compression molding process. By means of the experimental studies, a better understanding is gained on composite forming and its related thermal and deformation mechanisms. The experimental results were generated from a selected commercial GMT material. The experimental methods, however, can be expanded for use on other sheet-like thermoplastic composites.



## 1.3 Thesis Structure

This thesis is divided into six chapters. Followed by the brief introduction in this chapter, Chapter 2 is a short literature review on relevant characterization studies. The importance of each characterization perspective (heat transfer and material property) is also further discussed. The material property characterization is further divided into two categories — the draping characterization and the flow characterization. Chapter 3 develops an experimental set-up and a simulation-fitting method to characterize the heat transfer parameters during compression molding of GMT materials. Chapter 4 develops a large amplitude oscillatory method on a torsion bar fixture to characterize the viscoelastic properties relating to the draping of molten state GMT materials. Chapter 5 adopts an existing 1-D squeeze flow method to characterize the flowing behavior of a GMT stacked charge. Chapter 6 gives a summary, conclusions and comments on future work.

## Chapter 2

### 2 Review

This chapter reviews some existing characterization studies for the forming process of thermoplastic composites, which have inspired the technique development or experimental design discussed in chapters 3, 4 and 5.

#### 2.1 Heat Transfer in Thermoplastic Composite Forming Process

Charge temperature is an important process parameter in composite forming process. It can directly affect material mechanical properties and therefore, impact final forming outcomes [6], [7]. Various modes of heat transfer take place in the process cycle, which contribute to the charge temperature distribution. Many efforts have been made to investigate heat transfer and estimation of the charge temperature distribution. For example, Cunningham et al [7] studied radiative heat transfer when pre-heating the charge in an infra-red oven, and convective heat transfer when moving the charge from the heating oven to the mold. In their study, analytical methods were used to calculate the net radiation from oven and net heat loss during moving. The results were used in a finite element thermal model to predict charge core temperature, which were then compared with experimental measurements. Chy [6] also studied a feedback-control system for charge temperature distribution by modeling heating thermoplastic sheets with infra-red oven. In comparison with Cunningham et al. [7], Chy's model introduced the effect of air convection in the oven.

Heat transfer between plastic melts and mold surfaces is another often studied topic. Thermal contact conductance at the plastic-metal interface is commonly estimated to characterize this type of heat transfer [8], [9], [10], [11], but most of the studies have been for injection molding.

By definition, thermal conductance is characterized by a coefficient that relates the heat transfer flux with the temperature difference between the two contacting surfaces, in this case the sheet and mold surfaces, such that:

$$Q_{transfer} = h_c \cdot (T_{s1} - T_{s2}) \quad (2.1)$$

Where  $Q_{transfer}$  is the transferring heat flux ( $\text{W}/\text{m}^2$ ) and  $h_c$  is the thermal conductance ( $\text{W}/\text{m}^2 \cdot \text{K}$ ).

Bendada et al. [8] studied the positive correlation between contact conductance value and normal pressure at the interface. Somé et al. [10] further described this correlation with a mathematical model that was derived from basic topographical, mechanical and heat transfer principles. All the studies above focused on injection molding situations. The contact conductance varied from 400-5000  $\text{W}/\text{m}^2 \cdot \text{K}$ , depending on the pressure applied (0-25 MPa) and materials used.

Kugule et al. [12] investigated the contact conductance for thermoforming situations. Two conditions were considered — the open-mold condition where the charge sits on static bottom mold with no external pressure, and the closed-mold condition where the upper mold closes to apply pressure to the charge. These two conditions represent two necessary stages after pre-heating in the thermoforming process. Due to the additional pressure (0.6 bar), the closed-mold contact conductance (600-700  $\text{W}/\text{m}^2 \cdot \text{K}$ ) was found to be much greater than the open-mold one (100-300  $\text{W}/\text{m}^2 \cdot \text{K}$ ).

## 2.2 Draping Behavior of Thermoplastic Composite Sheets

In thermoforming or stamp-forming processes, a thermoplastic composite sheet is placed between two mold halves, where limited pressure is applied [13]. The sheet would deform into the mold geometry due to the pressure, where no flow or little flow of the material would take place [5], [14]. This deformation behavior is typically referred to as ‘draping’ of the material. In compression molding using sheet-like material, draping is also predominant in the initial phase of compression, where the mold pressure is not enough to generate material flow [14]. After the draping phase, the increasing pressure forces the material to flow and fill the entire mold. Accurate characterization and modeling of the draping behavior allows prediction of production defects such as wrinkling and folding in forming [5]. The draping behavior of thermoplastic composite sheets includes deformation micro-mechanisms [15], [16]. For multiple sheets with good

laminations, intra-ply shear is the main mechanism [17]. For stacked or delaminated sheets, however, inter-ply friction should also be considered [18].

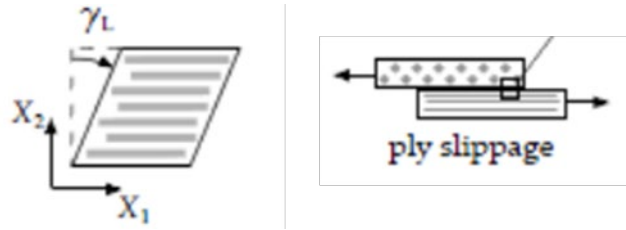


**Figure 2-1: Deformation micro-mechanisms contributing to draping (left) intra-ply shear and (right) inter-ply friction [13]**

For intra-ply shear, studies include Groves et al. [19], [20], Wheeler and Jones [21], McGuinness and Ó Brádaigh [22] and Stanley and Mallon [23]. Various set-ups were used in these studies, which also lead to very different shear rates or shear magnitudes for the results. Parameters such as shear viscosity and elastic modulus were characterized to describe the material draping behavior. However, these studies all had certain shortcomings, such as ignoring the effect of fiber orientation and distribution, or not eliminating inter-ply slippage in the shearing tests. This also led to large deviations between the viscoelastic parameters characterized from different set-ups (up to two orders of magnitude). Recently, Haanappel et al. [17] and Sachs and Akkerman [24] each developed a custom fixture based on use of a rotational rheometer to characterize the intra-ply shear of thermoplastic UD tapes. The fixtures support a rectangular torsion bar specimen [17] and a bending specimen [24], respectively (Figure 2.2). Both fixtures could induce intra-ply shearing of the specimens by rotation. By setting the rheometer to a constant speed rotation, the fixtures were able to deform the specimens to a large strain magnitude. The response torque was recorded by the rheometer, generating torque vs. deformation angle curves (Figure 2-4). Finite element software (Abaqus CAE) was used to simulate the experiments by means of a Kelvin-Voigt or Generalized Maxwell viscoelastic model [25]. The model parameters were adjusted in order to fit the simulated torque vs angle curve to the experimental data. In this way an elastic parameter and a viscous parameter were characterized using the model. These types of set-ups have the

advantage of controlling shear rate and magnitude, as well as testing in the desired fiber reinforcement direction.



**Figure 2-2: Intra-ply shearing fixtures developed by (left) Haanappel et al. [17] and (right) Saches and Akkerman [24]**

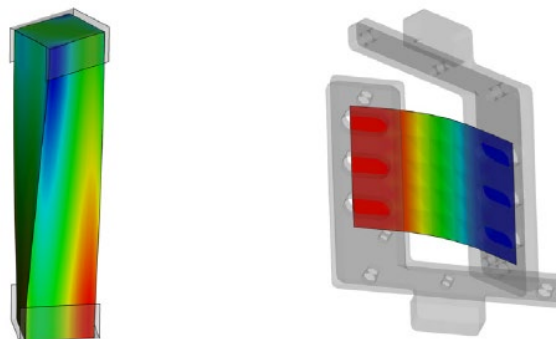


**Figure 2-3: Abaqus simulation of the experiments in Figure 2-2 [25]**

Dörr et al. [5] further applied these methods on glass mat thermoplastics (GMT). By using the parameter set generated from the tests, they successfully simulated the draping of the GMT sheet on a complex mold geometry, and predicted local wrinkling of the draped parts.

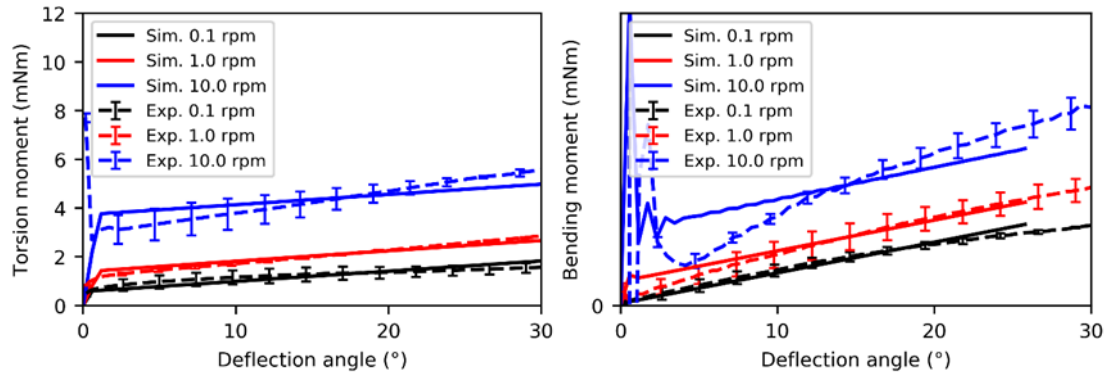


**Figure 2-4: Torque vs. deformation angle curves for the GMT material in (left) torsion experiment and (right) bending experiment [5]**

The inter-ply friction is another important topic in studies that aimed at characterizing draping behavior of thermoplastic composite sheets. Apart from inter-ply friction, the friction between sheet and the tool/mold (tool-ply friction) is often characterized at the same time in these studies. A thorough understanding of these frictional mechanisms would help developing modeling or computer simulation technologies to predict the draping behavior, thus minimize production defects [18].

Many research studies have been conducted to characterize the inter-ply and/or tool-ply frictional behavior. Various experimental methods were developed to perform these characterizations on thermoplastic composite sheets. Groves et al. [19] tested the resistance against inter-ply motions by placing a stack of continuous fiber thermoplastic laminates between the two rotating plates of a Rheometrics Dynamic Spectrometer. Groves represented such resistance by general terms of shear stress and shear viscosity. Scherer et al. [26] tested inter and intra-ply stresses of laminates by pulling one piece of polypropylene carbon UD tape out of a stack between two heated plates. No temperature or normal pressure dependence was investigated in these studies (Figure 2-5).

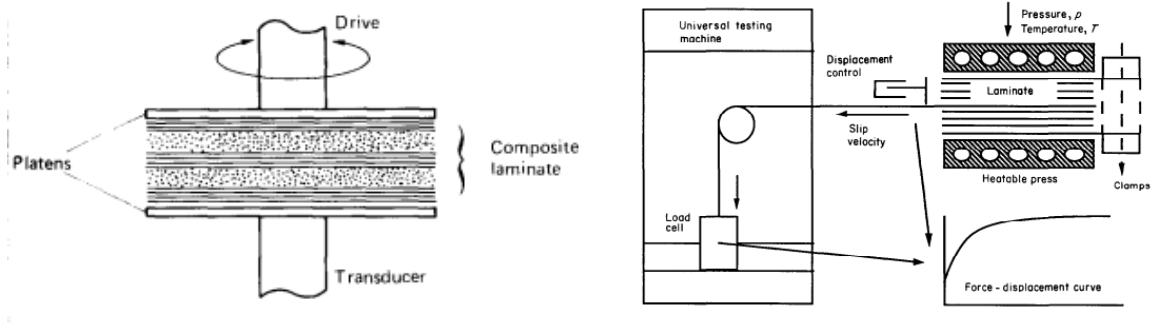


**Figure 2-5: Experimental set-up developed by (left) Groves et al. [19] and (Right) Scherer et al. [26]**

Murtagh et al. [27] developed a similar set-up with Scherer, but started to characterize the inter-ply slippage in a more quantitative manner, in terms of coefficient of friction (CoF). CoF is defined as the ratio of pulling force to normal load, such that:

$$\mu = \frac{F_f}{N} \quad (2.2)$$

Where  $\mu$  is the CoF,  $F_f$  is the pulling force and  $N$  the normal load (force).

In cooperation with other research institutions, Saches [28] from University of Twente conducted a benchmark study of different testing set-ups. All participants used their own testing apparatus to measure the tool-ply friction using Twintex® PP material under same predefined conditions. The basic principle of all participating set-ups was a pull-out/through test. The test involves either pulling a piece of steel foil out of two plies, or pulling a piece of ply out of two metal blocks. Despite the same basic principle, all set-ups can be divided into two main categories: horizontal set-up and vertical set-up. In general, horizontal set-ups may use a simple dead weight to apply normal load, but require preheating of the material to testing temperature. On the other hand, vertical set-ups may employ electrically heated pressure blocks, but need additional equipment to apply and monitor normal pressure (e.g. pneumatic bellows and load cells). Figure 2-6 illustrates typical examples of horizontal and vertical set-ups from TU Dresden and University of Twente.

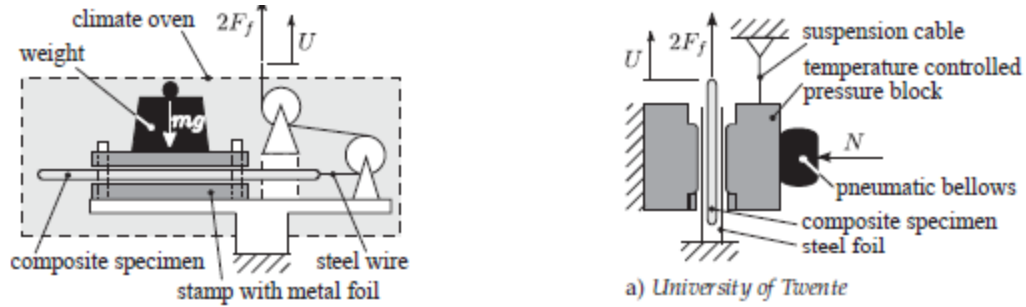


**Figure 2-6: Experimental set-ups to measure tool-ply and inter-ply friction: (left) horizontal apparatus from TU Dresden and (right) vertical apparatus from University of Twente [28]**

By analyzing the results from all participating set-ups, Saches et al. [28] concluded several points from a design perspective to help improve accuracy of friction measurement:

1. Using a large contacting surface and round-edges of contacting block help preventing edge effects during the pulling.
2. Stretch of the specimen need to be limited.
3. Uniform distribution of normal pressure and temperature is essential for tests conducted above melting temperature.
4. Pull-through test is preferred than pull-out test, as it provides a constant contacting area.

The results from all participants of this benchmark study also proved that tool-ply friction of Twintex® PP material follows a simple Amontons-Coulomb model under room temperature. The CoF was independent of pulling speed and normal pressure under such conditions. But when the test temperature went above melting temperature, hydrodynamic frictional behaviors started to be observed. The CoF started to be dependent on material viscosity, pulling speed and normal pressure through Hersey Number and Stribeck Curve.

Hersey Number is defined as below:

$$He = \frac{\eta \cdot v}{p} \quad (2.3)$$



where  $\eta$  is the viscosity,  $v$  the pulling velocity and  $p$  the normal pressure. Stribeck Curve is the correlation curve between CoF and Hersey Number.

By using the same set-up in Figure 4, Akkerman et al. [29] Successfully characterized the tool-ply frictional behaviors of UD-C/PEEK and 8HS-G/PPS materials above their melting temperature. Similar to results obtained by Saches et al. [28], the characterized frictions were also recognized as hydrodynamic lubrication (i.e. follows equation 2.3).

## 2.3 Flow Behavior of Thermoplastic Composites

In the compression molding of thermoplastic composites, the material is eventually forced to flow and fill the mold by increasing mold pressure. In the flowing phase, bulk viscosity of the charge is an important parameter to help predict the flow pattern and molding forces [30].

Typical methods for viscosity characterization include cone and plate viscometer, oscillatory shear (rotational rheometer) and squeeze flow tests. However, for long-fiber reinforced thermoplastic materials, a cone and plate viscometer cannot provide accurate results, as fibers tend to align with the motion direction [30]. Oscillatory shear is also not an appropriate option for this type of material, because it may be difficult to induce true shear flows [31].

Squeeze flow, on the other hand, has been an often used and constantly developed method for rheological characterization of GMT or SMC materials. SMC is another sheet-like composite material often used for molding automobile parts, similar to GMT material but with thermoset polymer matrix. In general, the method involves isothermally squeezing the material between two heated parallel plates, typically a circular shape. The squeezing plate can be either force control or speed control [30]. The pressing force is recorded against distance between the two closing plates. Then, a constitutive flow model can be fitted into the measured data to extract material viscosity or other parameters. The constitutive flow model is typically Generalized-Newtonian (Newtonian, power law, Herschel-Bulkley, or Bingham) depending on the material type [30]. For long-fiber GMT

materials, the most commonly used rheology model in previous studies are the power law models.

Kotsikos et al. [31] conducted squeeze flow tests on two commercial GMT materials with 30% and 40% glass content by weight, respectively. The tests were performed at constant closing speed using a set of 150 mm diameter heated plates, mounted on a universal testing machine. In order to characterize the flow, Kotsikos et al. [31] used two separate flow models, namely pure shear flow and pure extensional flow to describe the squeeze flow behavior. Extensional flow was predominant in squeeze flow, with shear near the plate wall. In later research, Kotsikos and Gibson [32], a more complex flow model which combines extensional and shear flow was developed for squeeze flow of SMC materials.

Dweib and O Br'adaigh [33] developed the method to characterize GMT material with anisotropic flow behavior. They discovered in previous studies that the originally round specimen deformed into an elliptical shape as shown in Figure 2-6:

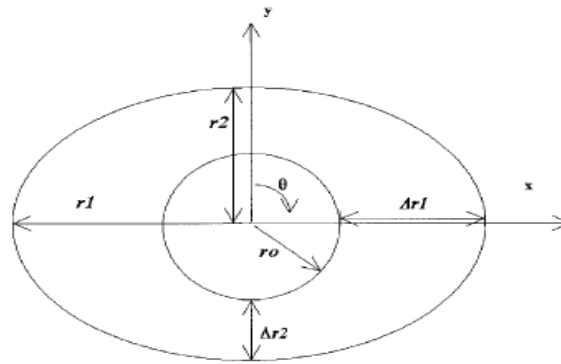


**Figure 2-7: Ellipse formed by squeeze flow of anisotropic GMT materials (Dweib and O Br'adaigh [33])**

Dweib and O Br'adaigh used the transversely isotropic power law model developed by Rogers [34] to characterize the tested material. Their model allowed the calculation of extensional viscosities in three directions:  $\lambda_1$  in  $x$  direction,  $\lambda_2$  in  $y$  direction, and  $\lambda_3$  in the normal direction.

Assuming incompressibility of the material, the strain rates in these three directions can be represented as:

$$\dot{\epsilon}_{xx} = \frac{fu}{(e+f)h} \quad (2.4)$$

$$\dot{\epsilon}_{yy} = \frac{eu}{(e+f)h} \quad (2.5)$$

$$\dot{\epsilon}_{zz} = -\frac{u}{h} \quad (2.6)$$

Where:

$$f = \frac{r1}{r2} \quad (2.7)$$

$$e = \frac{\Delta r1}{\Delta r2} \quad (2.8)$$

$u$  represents the closing speed of plates and  $h$  represents the distance between the two plates. Dweib and O Br'adaigh assumed pure extensional flow and used lubricant to create full slip at the plate walls. Thus, the extensional viscosities are calculated to be:

$$\lambda1 = \lambda3 = \frac{\bar{p}}{\left(\frac{u}{h}\right)} \quad (2.9)$$

$$\lambda2 = \frac{\bar{p}}{\left(\frac{u}{h}\right)} \left(\frac{e+f}{2e}\right) \quad (2.10)$$

Where  $\bar{p}$  is the average pressure over the squeeze area.

These models mentioned above all neglected the pressure distribution over the squeeze area. Kotsikose et al [35] in later studies developed a model to predict the radial pressure distribution during the squeeze process. The model was improved from the combined (extensional and shear) flow model in their early works [32]. Pressure cells over the squeezing plate were used to record pressure data and validate the model.

An important assumption of all the early studies was the incompressibility of GMT material during the press molding process. Recent research on SMC material observed

bubbles generated and transported when material filled the mold [36]. The release and growth of these bubbles could lead to a macroscopic compressibility on SMC materials [37]. A similar situation could be considered for GMT materials as well.

Hohberg et al. [38] developed a compressible squeeze flow model by using an 1-D flow rheological tool. Unlike earlier tools, which were mostly round plates, the equipment developed by Hohberg et al. was a plaque molding tool of rectangular shape, with dimensions 800 mm x 250 mm. The tool was able to produce plates with thickness between 1 mm to 5 mm. 7 pressure sensors were located along horizontal center line of the tool. A schematic of the tool is given by Figure 2-7.

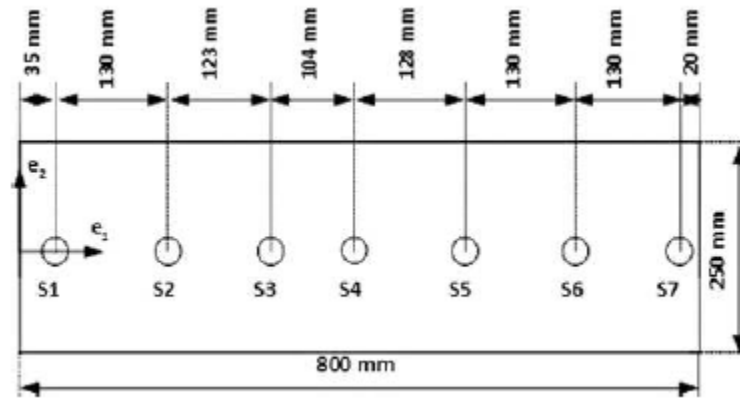


**Figure 2-8: The rheology tool developed by Hohberg et al. [24]**

As is shown in figure 2-7, the pressure sensors are aligned with  $e_1$  direction, which is the main flow direction during the squeeze flow test. This arrangement allows the characterization of the pressure distribution along the flow direction. The initial charge placed at sensor 1 location was squeezed at constant closing speed of the mold. The pressure values gathered by the 7 sensors were plotted against distance between the molds. A compressible flow model was developed by Hohberg et al. [38] to fit the experimental data. The fitting of this power law model allowed the extraction of hydrodynamic friction coefficient and extensional viscosity from the data:

$$\varepsilon_{33}(x1) = \eta \frac{1}{D_0^{n-1}} \left| \frac{\dot{h}}{h} \right|^{n-1} \frac{\dot{h}}{h} - \left( \frac{2\lambda}{m+1} \right) \frac{\dot{h}}{h^{m+1}} \left( \frac{|\dot{h}|}{V_0} \right)^{m-1} \left[ x1^{m+1} - \left( \frac{l_0 h_0}{h} (\Delta t \beta(t) + 1) \right)^{m+1} \right] \quad (2.11)$$

Where  $\varepsilon_{33}(x1)$  represents the local pressure measurement at position  $x1$ ,  $\eta$  represents the extensional viscosity,  $\lambda$  represents the hydrodynamic friction coefficient, and  $m$  as well as  $n$  are power law coefficients.  $D_0$  represents the reference deformation rate.  $h$  and  $\dot{h}$  are distance between the molds and the mold closing speed, respectively.

Subtracting measurements from two different sensors would yield the following equation:

$$\lambda = \frac{m+1}{2} \left( \frac{|\dot{h}|}{V_0} \right)^{-m+1} \frac{h^{m+1}}{\dot{h}} \frac{\varepsilon_{33}(x2) - \varepsilon_{33}(x1)}{[x2^{m+1} - x1^{m+1}]} \quad (2.12)$$

Data from four sensors yield a set of two equations in the form of equation 2.12. The values of  $m$  and  $\lambda$  can thus be determined from this equation set.

After knowing the values of  $m$  and the hydrodynamic friction coefficient  $\lambda$ ,  $n$  can be fitted by plotting  $\varepsilon_{33}$  against  $D_0$ . Afterwards, the extensional viscosity can be calculated. The authors [24] validated the accuracy of this model by performing squeeze flow test on three different SMC materials.

## Chapter 3

### 3 Characterize Heat Transfer Parameters in Compression Molding of Glass Mat Thermoplastics

In the thermoplastic composites forming process, charge temperature is an important process parameter that can eventually contribute to forming outcomes [39], [40], [6], [7]. Generally, charge temperature directly affects charge viscoelastic properties such as viscosity or elastic modulus, which then dominate the behavior of charge when it is deformed [6] and may affect ultimate final part properties. Final component properties can heavily depend on the charge temperature profile when it is formed [12]. At each stage of the process chain, the temperature profile of the charge is determined by heat transfer with either the ambient environment or the mold. In thermal modeling, the amount of heat exchange can be calculated once heat transfer parameters have been estimated for the various forms of heat transfer (i.e. conductive, convective and radiative). The compression molding process chain of GMT (Glass Mat Thermoplastics) material can be divided into four stages, in sequence: pre-heating, charge transfer from oven to mold, open-mold cooling of the charge, and closed-mold cooling after compression. Open-mold cooling is the period of time when the charge sheet is in the mold cavity before the mold closes, and closed-mold cooling refers to the compression molding phase before ejection.

At each stage, the GMT sheet exchanges heat with the surroundings. The flat geometry of the sheet means that the dominant heat transfer takes place at its top and bottom surfaces, making the through thickness temperature profile the main point of interest. Consequently, this chapter focuses on investigating heat transfer from the sheet top and sheet bottom during the process chain. Table 3-1 below summarizes the types of heat transfer at both sides of sheet during each process stage.

**Table 3-1: Heat transfer types at sheet surfaces during each process stage**

Process Stage	Heat Transfer at Top Surface	Heat Transfer at Bottom Surface
Pre-heating	Forced Convection	Forced Convection
Transfer	Forced/Natural Convection	Forced/Natural Convection
Open-Mold Cooling	Natural Convection	Contact Conduction with Mold
Closed-Mold Cooling	Contact Conduction with Mold	Contact Conduction with Mold

Natural and forced convection coefficients on flat geometries have been well studied and can be easily calculated with Nusselt Number correlations. On the other hand, thermal contact conductance between tool and sheet remains a challenge. Some researchers have studied the contact conductance between metal and polymer melts in injection molding [8], [9], [10], [11]. However, differences in the material and forming mechanism can cause the magnitude of heat transfer to be very different in injection molding compared to compression molding. Kugele et al. [12] studied contact heat transfer for thermoforming, which shares some similarities to compression molding. Therefore, based on their approach, an experimental setup was designed to characterize the tool-sheet contact conductance during open-mold and closed-mold cooling.

Due to complex flow pattern in the convection oven, the forced convection coefficient during pre-heating cannot be estimated by usual Nusselt Number equations which deal with uni-directional flow. Therefore, a similar approach was developed to also characterize forced convection coefficient within the oven.

## 3.1 Methods

### 3.1.1 Materials and Sample Preparation

The GMT sheet used in this study was Tepex Flowcore from Lanxess. Characteristics of the material are summarized in table 3-2 below.

**Table 3-2: Characteristics of Tepex Flowcore**

<b>Characteristic</b>	<b>Unit</b>	<b>Value</b>
Product Name	-	Tepex® Flowcore 102-RGR2400/47%
Fiber	-	E-Glass Roving
Weaving style	-	Random Mat
Fiber Length	mm	50
Fiber Content	vol.%	47
Polymer Matrix	-	Polyamide 6 (PA 6)
Bulk Density	kg/m <sup>3</sup>	1800
Thickness	mm	2

Pre-consolidated samples were prepared from several sheets of Tepex Flowcore. During consolidation of each sample, a thermocouple was embedded between middle layers to monitor the core temperature of the sample as a function of time. The thermocouple was also centered in the plane directions, so that it would not be affected by sidewall heat transfer. Two types of samples were prepared for each process stage: 4-layer consolidated samples and 6-layer consolidated samples. Each layer of Flowcore was 2 mm in thickness. However, the consolidation process resulted in fusion between the layers of Flowcore, and the thickness of the consolidated sheet was reduced to around 6 mm for the 4-layer samples, and around 9 mm for the 6-layer samples. The consolidated sheets had near square geometry with roughly 400 mm side length (300 mm squares before consolidation). Figure 3-1 below schematically illustrates the preparation process and the location of thermocouple in each type of sample.



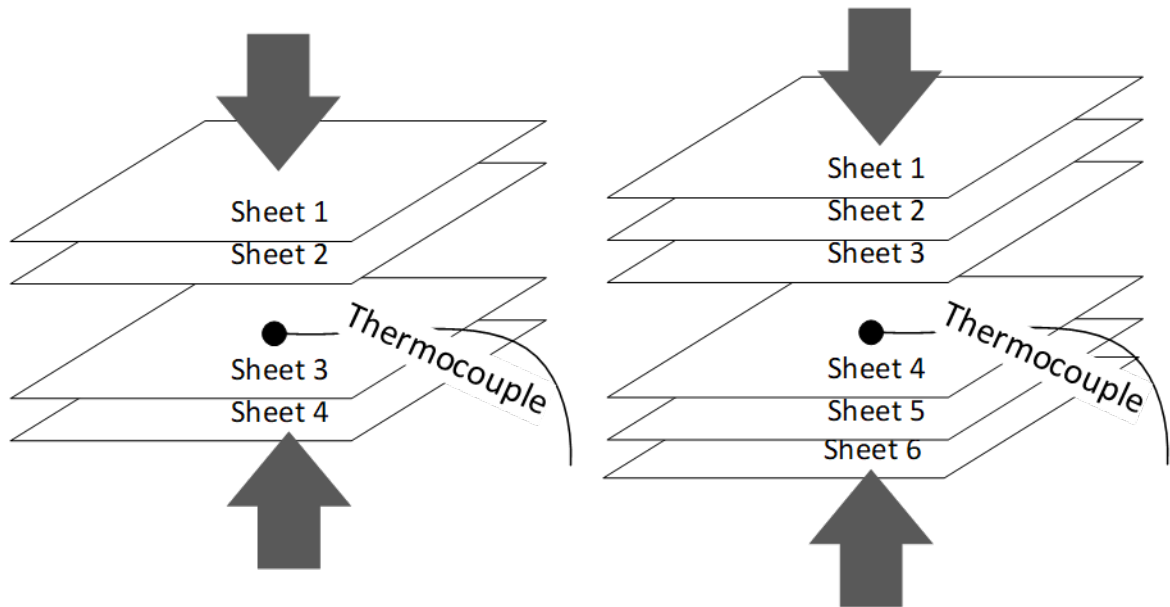


**Figure 3-1: Thermocouple placement during consolidation of experimental samples**

### 3.1.2 Experimental Set-up

The experimental procedure involved recording sample core temperature over time during process stages of interest.

For the pre-heating stage, each sample was heated in a forced convection oven (HK--Präzisionstechnik) from room temperature (typically between 20 and 25 °C). The oven was set at 300 °C. The sample core temperature was measured by the embedded thermocouple. A laptop was connected to the type K thermocouple wire through a transducer (Phidget TMP1101-0) for recording time evolution of measurements (Figure 3-4(a)).



**Figure 3-2: Forced convection oven (opened)**

For open-mold cooling and closed mold cooling, each sample was first pre-heated for 15-20 minutes so that it reached as close as possible to homogenous temperature distribution (no obvious increase of the core temperature). After pre-heating, the sample was transferred to a press (Dieffenbacher DCP-U 2500/2200) in the immediate vicinity of the oven (5-6 meters distance and 6-8 seconds transfer time). The sample then cooled due to heat transfer between its bottom surface and the mold, as



**Figure 3-3: Flat mold used (bottom half)**

well as the natural convection at its top surface. The mold used for these experiments had flat geometry, which was temperature controlled at 150 °C. For open-mold cooling situation, only the bottom mold was in contact with sample. The upper half of the mold remained open (Figure 3-4(b)). In closed-mold cooling, the upper mold closed and was in contact with the sample. The upper mold was set to stop pressing once the force build-up reached 400 kN (Figure 3-4(c)). Based on sample area, this force equates to a pressure of approximately 16 bar. In both types of cooling experiments, the sample core temperature was measured by embedded thermocouple and was recorded by a laptop. Schematics of the pre-heating experiment, open-mold and closed-mold cooling experiments are shown in Figure 3-4.

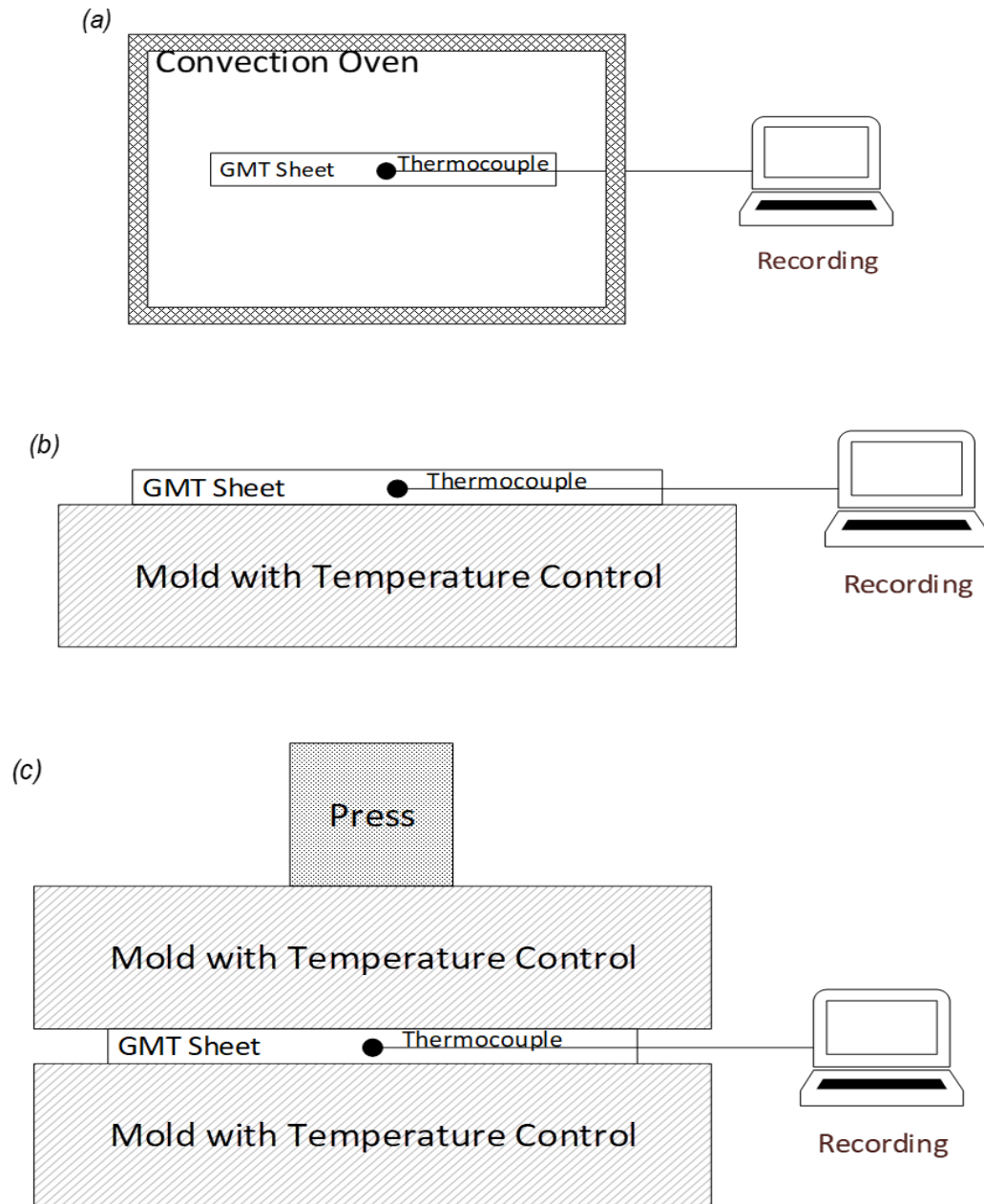


**Figure 3-4: Experimental set-up to collect sample core temperature during (a) pre-heating stage (b) open-mold cooling stage and (c) closed-mold cooling stage**

### 3.1.3 Thermal Modeling

The through-thickness temperature profile within the sample sheet was predicted using a 1-D transient conduction model. The heat transfer at sheet surfaces during each process stage was also modeled by applying corresponding boundary conditions.

According to Fourier's Law, (conductive) heat flux is proportional to the negative temperature gradient and to the area normal to the temperature gradient through which the heat flows. In a 1-D model, only heat transfer along the through-thickness direction is considered. If  $x$  is denoted as the thickness direction, the heat flux through any cross section along this axis is given by equation 3.1.

$$q(x) = -k \cdot \frac{dT}{dx} \quad (3.1)$$

where  $k$  is the bulk thermal conductivity of the material.

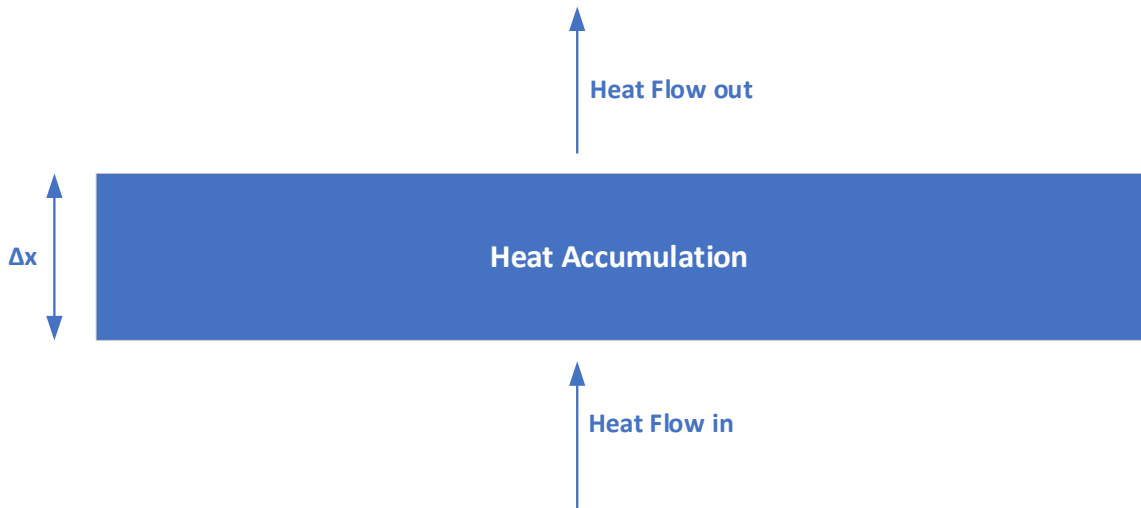


**Figure 3-5: A section of the sample along  $x$  axis with thickness  $\Delta x$**

Heat balance analysis can be performed by dividing the sample into infinitely many segments with thickness  $\Delta x$  and considering one of them (Figure 3.5). Under transient state, heat flowing into the segment must be equal to the sum of heat flowing out and heat accumulation [41]:

$$-k \cdot a \cdot \frac{\partial T}{\partial x(x)} = \rho \cdot a \cdot C_p \cdot \Delta x \cdot \frac{\partial T}{\partial t} - k \cdot a \cdot \frac{\partial T}{\partial x(x+\Delta x)} \quad (3.2)$$

Where  $a$  is area of the cross section and  $C_p$  is bulk heat capacity of the material.

The term on left side of the equation represents heat flowing into the segment, whereas the terms on right side represents heat accumulation and heat flowing out,

respectively. Dividing both sides by  $a \cdot \Delta x$  and rearranging, the 1-D transient conduction model can be obtained (equation 3.3).

$$k \cdot \frac{\partial^2 T}{\partial x^2} = C_p \cdot \rho \cdot \frac{\partial T}{\partial t} \quad (3.3)$$

For the model to be able to predict charge temperature profile, correct boundary conditions with respect to each process stage must be applied at top and bottom surfaces of the sample. In general, the boundary conditions are based on continuity of heat flux.

For the pre-heating stage, a forced convection boundary condition was applied at both surfaces of the sheet. In this case, the magnitude of convection coefficient was assumed to be the same at both the top and bottom surfaces. The boundary conditions are given as:

$$-k \cdot \frac{\partial T}{\partial x}(L, t) = h_f \cdot (T_{s-top} - T_{oven}) \quad (3.4)$$

$$-k \cdot \frac{\partial T}{\partial x}(0, t) = h_f \cdot (T_{oven} - T_{s-bottom}) \quad (3.5)$$

Where  $L$  represents the entire thickness of the sheet, and  $h_f$  is the forced convection heat transfer coefficient inside the oven.

For the transfer stage, natural convection in combination of radiation boundary conditions are applied (equations 3.6 and 3.7). In this case, the magnitudes of heat transfer at the top and bottom surfaces can be different because hot air always tend to flow upward.

$$-k \cdot \frac{\partial T}{\partial x}(L, t) = h_{n-top} \cdot (T_{s-top} - T_{air}) + \sigma \epsilon \cdot (T_{s-top}^4 - T_{air}^4) \quad (3.6)$$

$$-k \cdot \frac{\partial T}{\partial x}(0, t) = h_{n-bottom} \cdot (T_{air} - T_{s-bottom}) + \sigma \epsilon \cdot (T_{air}^4 - T_{s-bottom}^4) \quad (3.7)$$

In the equations above,  $h_{n-top}$  and  $h_{n-bottom}$  are natural convection coefficients at top and bottom surfaces, respectively. Furthermore,  $\sigma$  is the Stefan-Boltzmann constant, and  $\epsilon$  is the emissivity.

During open-mold cooling, the top surface of sheet exchanged heat with the environment in the mold cavity area. Therefore, a combined radiation and natural convection boundary condition was used (equation 3.8). The bottom surface of sheet contacted with the mold, thus the heat transfer here was modeled by thermal contact conductance (equation 3.9).

$$-k \cdot \frac{\partial T}{\partial x}(L, t) = h_{n-top} \cdot (T_{s-top} - T_{air}) + \sigma \epsilon \cdot (T_{s-top}^4 - T_{air}^4) \quad (3.8)$$

$$-k \cdot \frac{\partial T}{\partial x}(0, t) = h_{c-open} \cdot (T_{mold} - T_{s-bottom}) \quad (3.9)$$

In equation 3.9,  $h_{c-open}$  is the contact conductance at sheet-mold interface under open-mold condition, i.e. not compressed.

During closed-mold cooling, both sides of the sheet were in contact with the mold. Therefore, equation 3.10 and equation 3.11 were applied at top and bottom surfaces respectively in this case. Here,  $h_{c-close}$  was the sheet-mold contact conductance under closed-mold condition and was assumed same in magnitude at both sides.

$$-k \cdot \frac{\partial T}{\partial x}(L, t) = h_{c-close} \cdot (T_{s-top} - T_{mold}) \quad (3.10)$$

$$-k \cdot \frac{\partial T}{\partial x}(0, t) = h_{c-close} \cdot (T_{mold} - T_{s-bottom}) \quad (3.11)$$

Homogeneous temperature distribution was used as initial condition for modeling of all the stages mentioned above. Room temperature was used for pre-heating stage. Core temperature measured after pre-heating was used for cooling stages.

### 3.1.4 Parameter Estimation

The parameters to be estimated were the heat transfer coefficients given in previous section, i.e.  $h_f$  during pre-heating stage,  $h_{n-top}$  and  $h_{n-bottom}$  during transfer,  $h_{c-open}$  during open-mold cooling and  $h_{c-close}$  during closed-mold cooling stage.

As was mentioned, theory of natural convection around plate geometry has been well studied. Nusselt Number correlations are typically used to estimate the natural convection coefficient. Therefore, values of  $h_{n-top}$  and  $h_{n-bottom}$  are determined by this method. Here, the correlation from [41] is taken for the purpose.

The Nusselt Number is given as:

$$Nu = c \cdot (Gr \cdot Pr)^n \quad (3.12)$$

Where  $Gr$  is the Grashof number defined as:

$$Gr = \frac{g \cdot \beta (T_s - T_{air}) L^3}{\nu^3} \quad (3.13)$$

and  $Pr$  is the Prandtl Number defined by:

$$Pr = \frac{c_p \cdot \mu}{k} \quad (3.14)$$

In equation 3.13,  $L$  is the characteristic length of the plate. The rest parameters showing in equations 3.13 and 3.14 are air properties at film temperature, i.e. the average between surface temperature and room temperature. In equations 3.12, parameters  $c$  and  $n$  can be determined by the following ranges of applicability [41]:

**Table 3-3: Rules for determining values of  $n$  and  $c$** 

Side of Horizontal Plate	Range of $(Gr \cdot Pr)$	Value of $c$	Value of $n$
Top Side	$10^5$ to $2 \times 10^7$	0.54	1/3
	$2 \times 10^7$ to $3 \times 10^{10}$	0.14	1/4
Bottom Side	$3 \times 10^5$ to $3 \times 10^{10}$	0.27	1/4

After Nusselt Number is determined, the natural convection coefficient can be calculated by equation 3.15.

$$h_n = \frac{Nu \cdot k}{L} \quad (3.15)$$

Although the natural convection coefficients can be estimated from literature correlations, other heat transfer parameters must be estimated from experimental data. The estimation was done by fitting experimental data to the model developed in section 3.1.3.

In a first step, initial values were assigned for these coefficients, based on which the transient temperature modeling of 4-layer samples were solved using finite element method (FEM) simulation software (Abaqus CAE). Uncoupled heat transfer analysis and element type DC3D8 were defined for the Abaqus simulations. Sheet surface emissivity was input at 0.8 based on literatures reporting [42], [43], [44], [45]. Other necessary material thermal properties were measured by the Moldex3D Material Testing Lab and are summarized in Tables 3-4, 3-5 and Figure 3-6. The data belongs to and was kindly shared by General Motors. Figures 3-7 and 3-8 illustrate example simulations created for the open-mold and closed-mold cooling stages. The simulated core temperature-time curve was then compared to the experimental measurement. Afterwards, the values of the coefficients to be estimated (  $h_f$ ,  $h_{c-open}$  and  $h_{c-close}$  ) were iteratively altered until the simulation curves matched the experimental ones.



**Table 3-4: Heat capacity of Tepex Flowcore measured at Moldex3D Material Testing Lab**

Temperature (°C)	Heat Capacity (J/kg·K)
35	1067
90	1384
110	1484
160	1702
170	1809
175	1973
180	2671
185	4134
190	2016
195	1684
230	1687
290	1657

**Table 3-5: Thermal conductivity of Tepex Flowcore measured at Moldex3D Material Testing Lab**

Temperature (°C)	Thermal Conductivity (W/m·K)
30	0.423
100	0.473
200	0.397

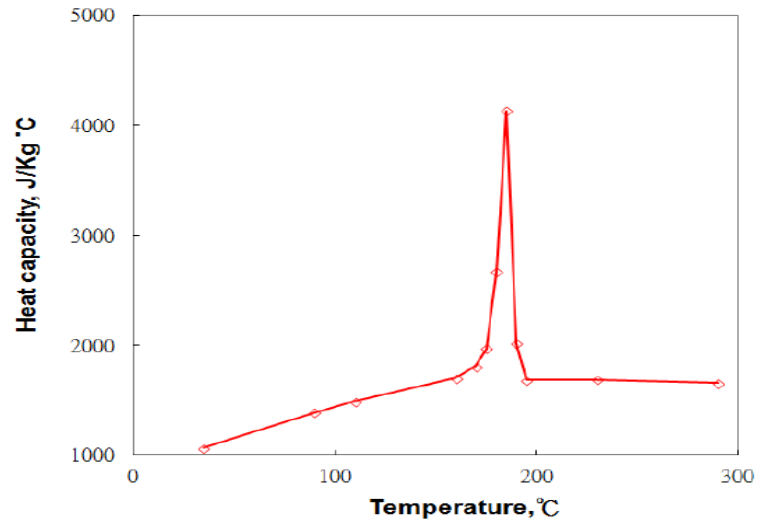


**Figure 3-6: Plot of heat capacity data in Table 3-4, peak indicates the recrystallization temperature range of the material**

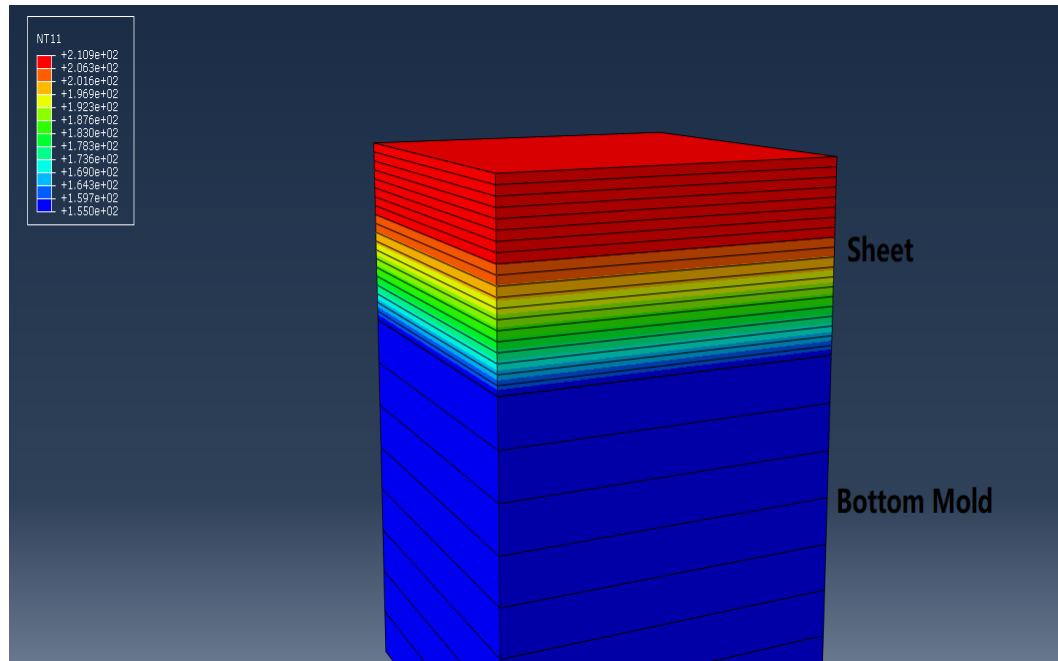


**Figure 3-7: Abaqus simulation for open-mold cooling stage**

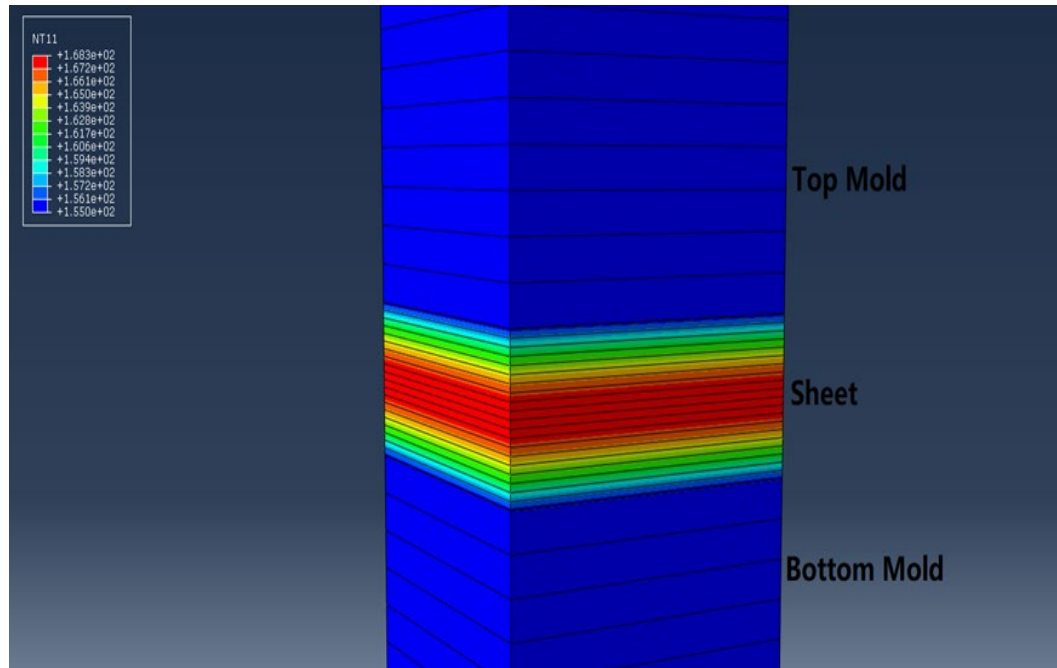


**Figure 3-8: Abaqus simulation of closed-mold cooling stage**

### 3.1.5 Parameter Validation

As was mentioned, two types of samples were used for each process stage. The main difference between the two was the number of consolidated layers, and therefore the thickness and mass. The heat transfer coefficients estimated using 4-layer samples were then applied to the modeling of 6-layer samples. These coefficients can then be validated by checking if they predict well the thermal behavior of the 6-layer sample. All the fittings and validations use RMSE (root mean square error) as evaluation function. The fittings were optimized by slope-based approach, i.e. the concept of response surface methodology however with single input variable.

## 3.2 Results and Discussion

### 3.2.1 Pre-Heating Stage

Figure 3-9 compares the experimental temperature-time curve and simulated temperature-time curve for pre-heating sample sheets in the oven. Figure 3-9(a) shows the results after fitting forced convection ( $h_f$ ) coefficient using 4-layer sample. Figure 3-9(b) shows the validation by applying this coefficient on 6-layer sample.

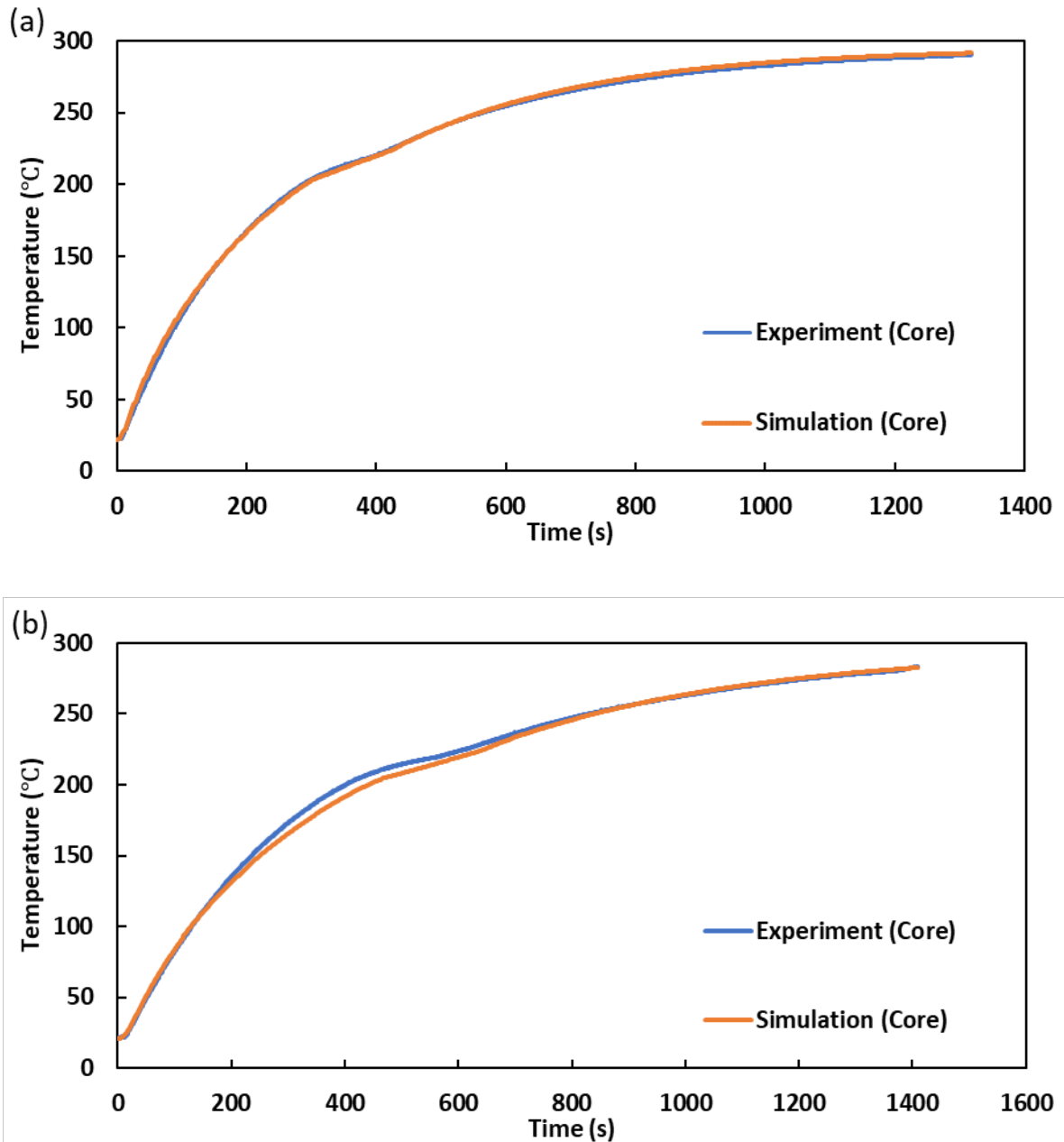


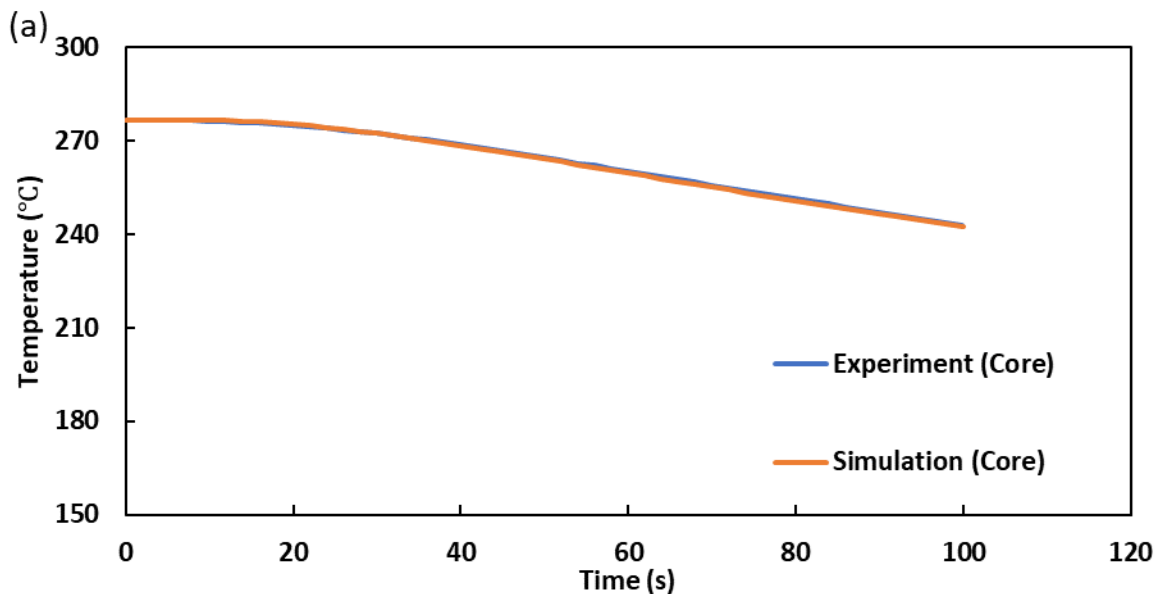
**Figure 3-9: Simulated core temperature compared with experimental core temperature during pre-heating stage (a) parameter estimation using 4-layer sample (b) parameter validation using 6-layer sample**

In both cases, the simulation matches well with experiment over the entire heating period. In experimental curve, the melting of the polymer matrix (the sudden drop of curve slope

near 220 °C) has been captured. This was predicted by including latent heat (21.4 kJ/kg, calculated from heat capacity data in Table 3-4) in the simulation.

### 3.2.2 Cooling Stages

Figure 3-10(a) presents the simulated curve and experimental curve for the 4-layer sample in the case of open-mold cooling. Good agreement was obtained by fitting the thermal contact conductance value between the sheet and mold interface. However, after applying this value to the 6-layer sample, the simulation predicted significantly higher core temperature than experiment (not shown in Figure 3-10). This suggested that the contact conductance fitted from 4-layer sample does not apply to 6-layer sample. It is possible that the heavier sample created more pressure on the lower mold surface and led to a better contact at the interface. This phenomenon was also observed by Kugule et al. [12] in their study for thermoforming process. Consequently, in the case of open-mold cooling, a separate fitting was performed for the 6-layer sample to determine a different conductance value. Figure 3-10(b) compares the predicted cooling curve against experiment after performing the fitting for 6-layer sample.



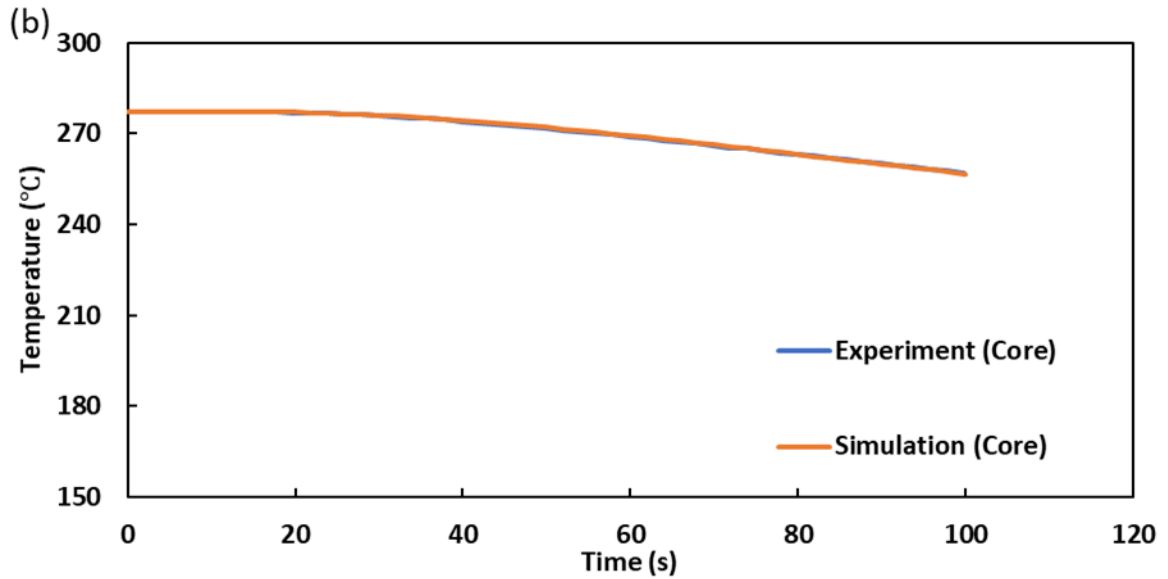


**Figure 3-10: Simulated core temperature compared with experimental core temperature during open-mold cooling stage (a) parameter estimation using 4-layer sample (b) parameter estimation using 6-layer sample**

During closed-mold cooling, the press exerted additional force on sample that was much greater than sample weight (400 kN vs. 0.013-0.019 kN), making the difference between the two sample types negligible. In other words, the sheet-mold contact conductance can be considered equal for 4-layer and 6-layer samples in this case. Figure 3-11(a) shows the estimation of the conductance using 4-layer sample and Figure 3-11(b) shows the validation using a 6-layer sample. Again here, simulation predictions match well with experimental measurements for both types of samples.

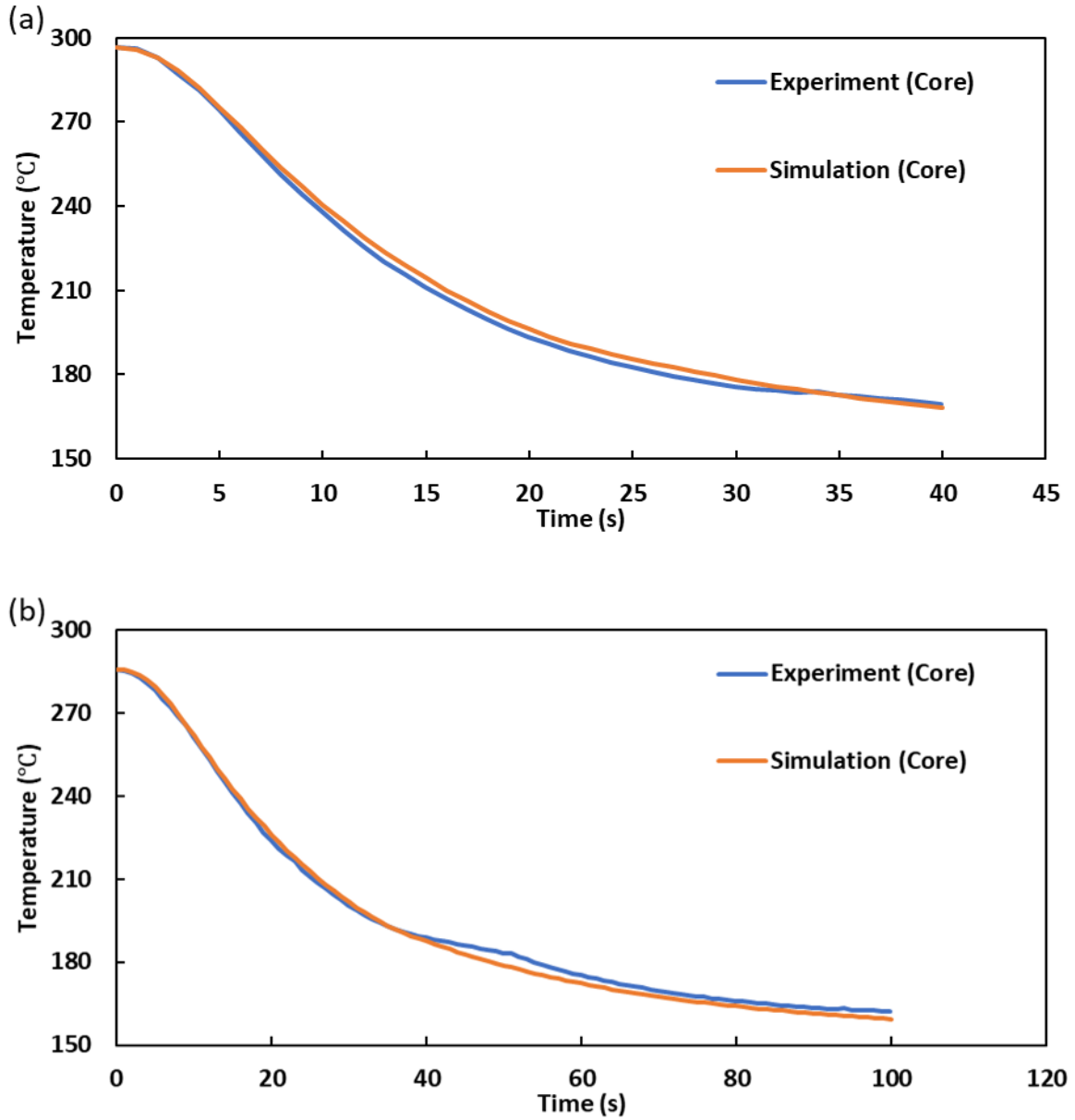


**Figure 3-11: Simulated core temperature compared with experimental core temperature during closed-mold cooling stage (a) parameter estimation using 4-layer sample (b) parameter validation using 6-layer sample**

### 3.2.3 Estimated Parameters

Table 3-6 summarizes the estimated heat transfer coefficients in each studied process stage, where  $h_{n-top}$  and  $h_{n-bottom}$  are natural convection coefficients calculated directly

from correlations (marked with asterisks),  $h_f$ ,  $h_{c-open}$ , and  $h_{n-close}$  are heat transfer parameters estimated by the model-fitting method compared to experimental data.

**Table 3-6: Summary of estimated heat transfer parameters**

Process Stage	Value of Heat Transfer Parameter	
Pre-Heating	$h_f = 36 \text{ W/m}^2 \cdot \text{K}$	
Transfer	Top Side*	$h_{n-top} = 8.5 \text{ W/m}^2 \cdot \text{K}$
	Bottom Side*	$h_{n-bottom} = 4.5 \text{ W/m}^2 \cdot \text{K}$
Open-Mold Cooling	4-Layer Sample	$h_{c-open} = 280 \text{ W/m}^2 \cdot \text{K}$
	6-Layer Sample	$h_{c-open} = 490 \text{ W/m}^2 \cdot \text{K}$
Closed-Mold Cooling	$h_{c-close} = 7500 \text{ W/m}^2 \cdot \text{K}$	

As can be seen in open-mold cooling, heavier samples lead to greater sheet-mold contact conductance due to the reason explained in Section 3.2.2. In the cases of pre-heating and closed-mold cooling, a single heat transfer coefficient value was adequate for modeling sheets with different thicknesses. Additionally, the closed-mold  $h_{c-close}$  value was found to be much higher than open-mold  $h_{c-open}$  values because of the press force applied. This would explain the rapid cooling of sheet usually observed during the forming (closed-mold) stage [46].

### 3.3 Applications in Process Chain

Characterizing these heat transfer parameters enables accurate prediction of through-thickness temperature profile within charge, which further enables better process optimization. Sensitivity analysis is an essential step in process optimization, as it studies the impact of process conditions on process outcomes. In compression molding process, conditions such as mold temperature and sheet thickness can significantly affect the evolution of charge temperature distribution which directly impacts the final molding



outcome. Knowing the heat transfer parameters, the effects of these process conditions can be easily analyzed by varying them in the thermal modeling. To illustrate this application, a sensitivity analysis was performed by simulation with several combinations of sheet thicknesses and mold temperatures, while keeping all other process conditions (e.g. heating time, transfer cooling time, on-mold cooling times) the same. The resulting sheet temperature profiles at the final closed-mold stage are plotted in Figure 3-12. In the figure, the recrystallization temperature of polymer matrix was marked with a vertical red line (at 190 °C).

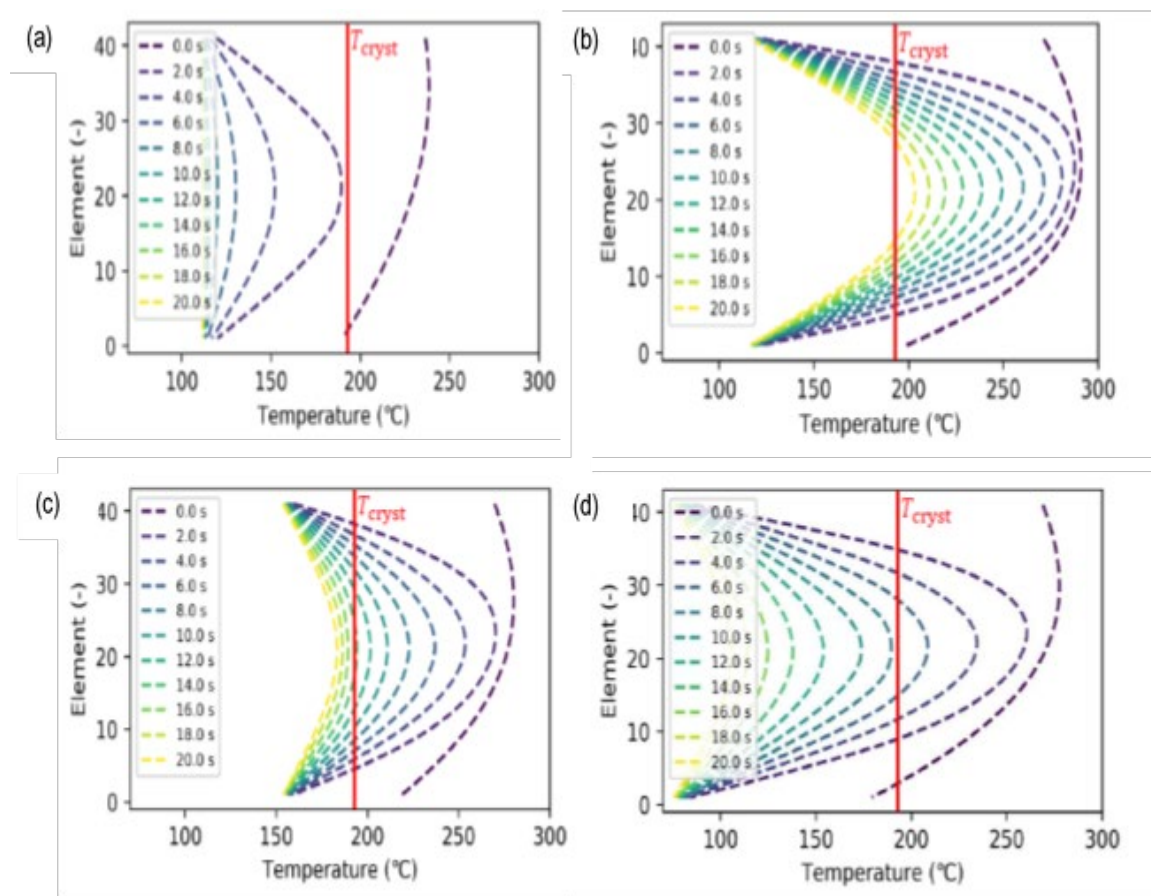


**Figure 3-12: Simulated through-thickness temperature profile for studied process conditions (a) single layer sample and 110 °C mold temperature (b) 3-layer sample and 110 °C mold temperature (c) 2-layer sample and 150 °C mold temperature (d) 2-layer and 70 °C mold**

In all conditions, the sheet temperature profiles are initially asymmetric as a result of open-mold cooling prior to mold closure. After the mold closes, large  $h_{c-close}$  values at both sides of sheet lead to rapid cooling of surfaces to mold temperature, and consequently an evolution toward a symmetric temperature profile. The main effect of the studied process conditions is considered at core of the sheet. Figure 3-12(a) shows that a single layer sheet will solidify completely in 2 seconds at 110 °C mold temperature. The core of a thicker 3-layer sheet can remain above recrystallization temperature for much longer at the same mold temperature (Figure 3-12(b)). Figures 3-12(c) and 3-12(d) suggest that elevated mold temperature (150 °C vs. 70 °C) can significantly lengthen the time to solidify the core of sheet. A complete summary of all simulated conditions and the resulting time to solidify the core of sheet are given in Table 3-7. For thickest sheets and highest mold temperature (Table 3-7), the sheet core can remain molten (over 190 °C) for over 20 seconds. In the case of thinnest sheet and lowest mold temperature (Table 3-7), however, complete solidification takes place in 2 seconds. Based on this data, the time window of forming can be estimated accordingly with respect to different mold temperatures and types of sheet used.

**Table 3-7: Simulated conditions and corresponding time to complete solidification after the mold closes**

Sample Thickness	Mold Temperature (°C)	Time to Complete Solidification After Mold Closes (s)
Single Layer	70	1.7
Single Layer	110	2.5
Single Layer	150	3.5
2-Layer	70	9.2
2-Layer	110	13.0
2-Layer	150	>20.0
3-Layer	70	>20.0
3-Layer	110	>20.0
3-Layer	150	>20.0

### 3.4 Conclusions

In this chapter, an experimental setup was designed to measure the core temperature of GMT sheets at each stage of the compression molding process. A one-dimensional thermal model was used to predict the through thickness temperature profiles of sheets. Natural convection heat transfer coefficients at sheet surfaces during transfer and open-mold cooling stages were directly calculated by Nusselt Number correlations. By fitting model prediction to experimental data, other important heat transfer parameters during different process stages were characterized. With these heat transfer parameters, the evolution of charge temperature profile through process chain can be accurately simulated. The application of accurate thermal modeling can further assist in the optimization of the molding process, for example sensitivity analyses and time window determination. In addition, the thermal modeling can be coupled with mechanical modeling, developing thermomechanical approaches to simulate the material forming behavior [47].

## Chapter 4

### 4 Material Characterization for Draping Simulations

Computer simulation is a powerful tool to help develop compression molding processes. With accurate prediction of material behavior during forming, the process development can be accelerated and optimized [5], [14]. In the case when a sheet-like charge is used in compression molding, the forming process can be divided into two phases, namely a draping phase and flowing phase [14]. In the draping phase, the sheet drapes into mold cavity with slight pressure applied on the mold, where little or no flow behavior takes place. In the flowing phase, the mold pressure increases and forces the material to flow and fill the entire cavity. Figure 4-1 illustrates the two phases in the compression molding of thermoplastic sheets.

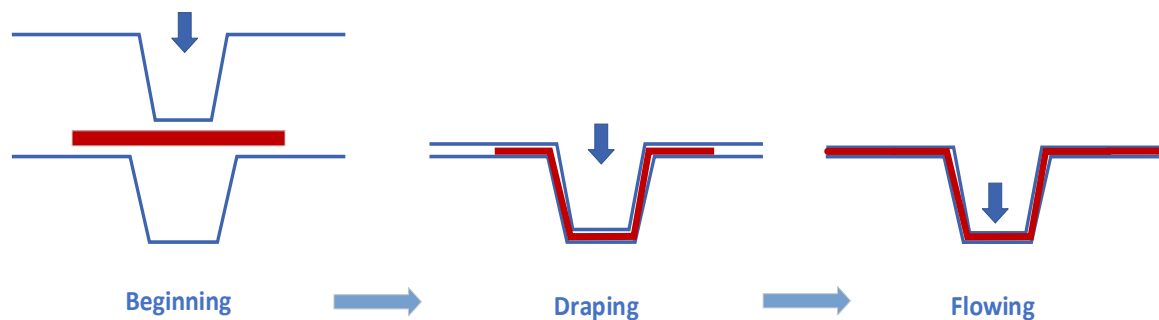


**Figure 4-1: Draping and flowing phases of the compression molding process**

Modeling the draping phase is an important part of compression molding simulation, as it predicts forming defects such as local wrinkling and part distortion [5], [13], [14], [48]. In the draping phase, the molten state sheet barely flows, but deforms into the structured shape due to contact mold pressure. The material deformation is dominated by the behavior called intra-ply shearing (Figure 4-2,  $X_2$  is the thickness direction,  $X_1$  is the shearing direction). To model this shear behavior, viscoelastic

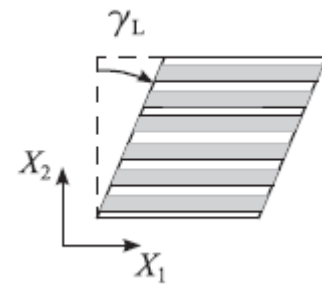


**Figure 4-2: Intra-ply shearing when material is draping [17]**

properties of the molten state material must be characterized.

Many set-ups have been developed to characterize the shear behaviors of thermoplastic composites. For example, Haanappel et al. [17] developed an oscillatory torsion bar method on a rotational rheometer. Margossian et al. [49] used dynamic mechanical analysis system (DMA) and a bending fixture to investigate the viscoelastic properties of thermoplastic UD tapes. However, both their methods were conducted under small strain conditions, where the material was in its linear viscoelastic regime (LVE). In LVE, the microstructure of material remains unchanged, and therefore the properties such as shear modulus or viscosity is constant or independent of strain amplitude. However, when material undergoes large strain deformation, such as in the case of compression molding, its microstructure breaks and would lead to change of shear properties depending on strain amplitude. Characterization methods under large strain conditions include the rheometer bending presented by Sachs et al. [24] and the modified torsion bar presented by Haanappel et al. [17]. The two methods shared similar concepts but had different specimens and fixtures (figure 4-3).

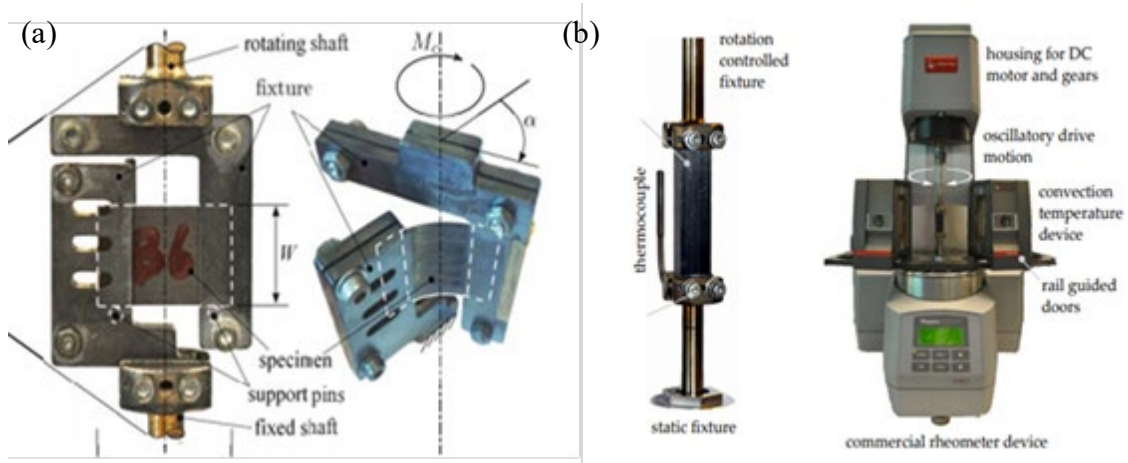


**Figure 4-3: Fixtures and specimens to characterize intra-ply shearing presented by (a) Sachs et al. [24] and (b) Haanappel et al. [17]**

In both methods, steady rotation of the rheometer was conducted up to a maximum angle of  $60^\circ$ . This large rotational angle enabled capture of non-linear viscoelastic behavior of the material. By fitting experimental data to nonlinear viscoelastic models, the methods

were able to characterize shear properties used for thermoforming simulations, which is very similar to the draping phase of compression molding. However, these methods require building custom fixtures that are not part of the standard equipment set of a commercial rheometer. Furthermore, some rheometer types do not provide the function of steady rotation. In this chapter, a large strain method was developed to characterize the viscoelastic properties of selected glass mat thermoplastic (GMT) sheet. The method was based on large amplitude oscillatory shear (LAOS), which is convenient to set up on most commercial rotational rheometers. The fixture was torsion bar set-up provided in the rheometer equipment set. Using the LAOS theory developed by Ewoldt et al. [50], the shearing data was analyzed to decouple and estimate shear modulus and shear viscosity of the GMT material. The properties were then fitted into Cross-WLF viscosity and WLF modulus models to generate materials card that can be used as input for draping simulation during compression molding the GMT. Finally, characterization methods presented by Sachs et al [24] and Haanappel et al [17] were also conducted for the same material at Fraunhofer ICT (Pfinztal, Germany). The properties characterized by the three methods were compared and validated.

## 4.1 Material and Property Anisotropy Examination

The main characteristics of the Tepex Flowcore material were given in Table 3-2. For fiber reinforced materials, it is possible that the mechanical properties are anisotropic due to factors such as fiber orientation. Uni-directional machine patterns were found to appear on blank Tepex Flowcore sheets (Figure 4-4). This might suggest that the sheet had passed through rollers when it was manufactured, which could lead to slight deviation from the intended random fiber orientation, and consequently anisotropic mechanical properties. To test this hypothesis, a simple squeeze

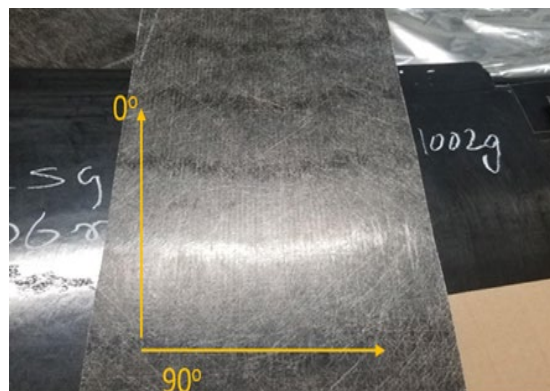


**Figure 4-4: Machine pattern on Tepex Flowcore and the two objective directions**

flow test was performed. Two objective directions were specified with respect to the pattern direction (Figure 4-4).

The material was cut into 10 cm x 10 cm squares, stacked into 10 layers and squeezed at molten state by the press (Dieffenbacher DCP-U 2500/2200). The squeezed flow length in the two objective directions were found to be constantly different in all 6 repeated tests. The after-flow dimensions of sample in each test were measured and are summarized in Table 4-1. A graphical comparison is illustrated in Figure 4 using results from test #1 (yellow square represents the original charge location).

**Table 4-1: After-flow dimensions measured in two objective directions**

Test Number	Length in 0 direction (cm)	Length in 90 direction (cm)
1	25.755	30.370
2	24.945	31.589
3	29.164	36.005
4	29.155	37.695
5	33.003	40.442
6	33.135	45.034

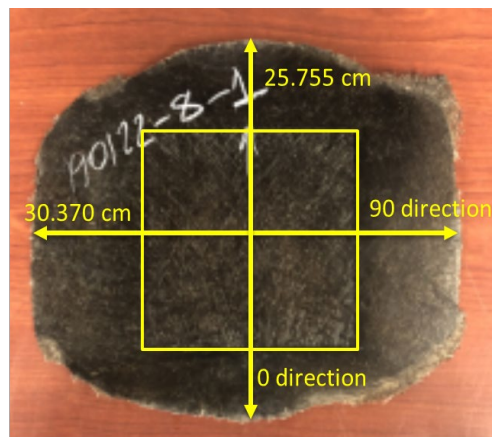


**Figure 4-5: Squeezed charge from test #1**



The flow length in 0 direction being constantly lower could suggest that fibers orient slightly more in this direction in the blank sheet. To further validate this point, a micro-CT analysis was performed on Tepex Flowcore to study the fiber orientation distributions. The test was performed on a Zeiss Xradia 410 Versa Micro-CT. Rectangular sample (49 mm x 11 mm) was cut from the 2 mm thick Flowcore blank (as received, not molded) sheet. The sample was scanned at voxel sizes of 5  $\mu\text{m}$  with beam energy of 40 kV. The results are given in Figure 4-6.

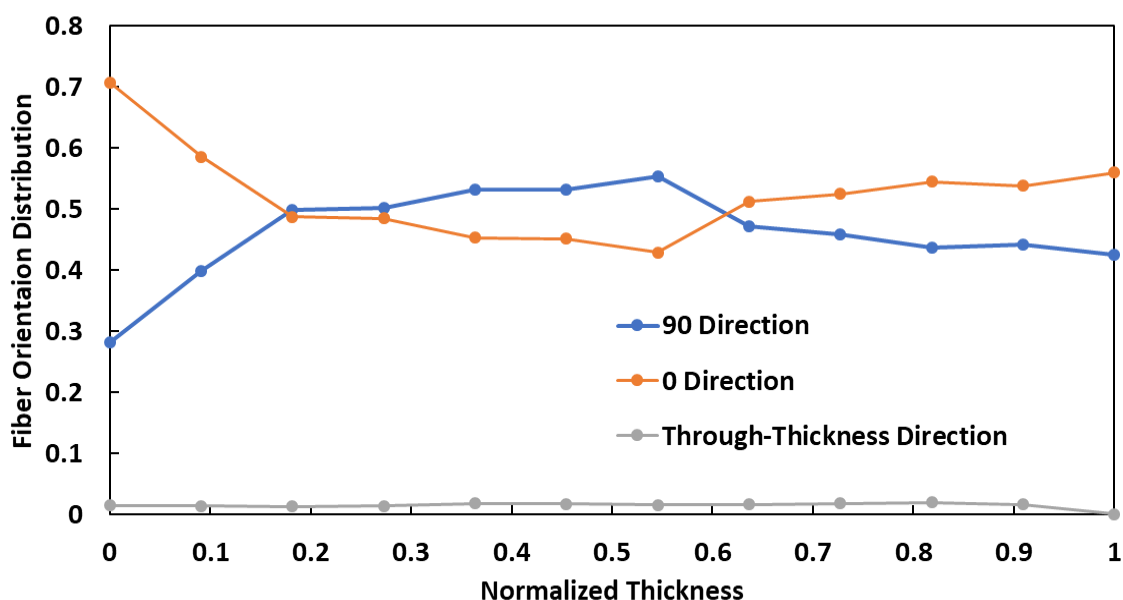


**Figure 4-6: Fiber orientation distribution of Tepex Flowcore blank sheet**

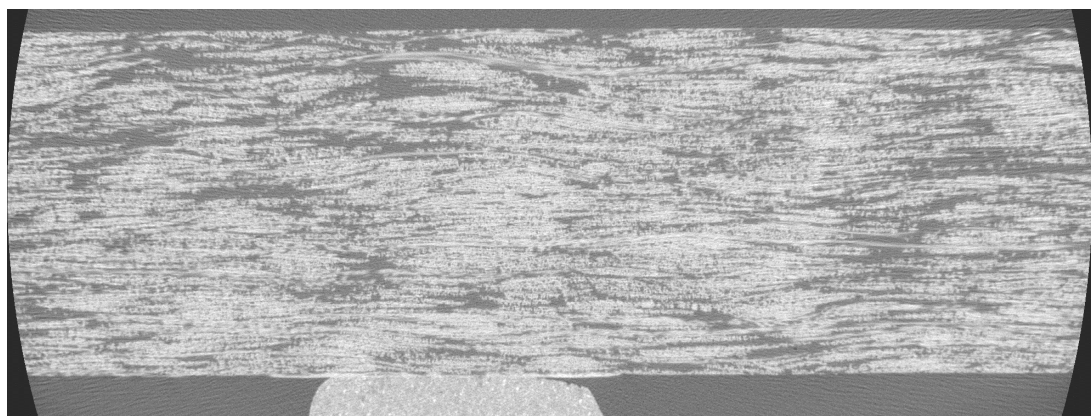


**Figure 4-7: One of the micro-CT stitch images taken on the sample (view through the thickness)**



As can be seen in figure 4-6, the fiber orientation of Tepex Flowcore is random in the two objective directions through most of the thickness. However, near one side of the sheet, the fibers tend to orient more toward the 0 direction and eventually lead to a highly uneven distribution at the surface. This finding explains the different flow lengths found in squeeze flow test. Furthermore, it can cause anisotropic shear properties of the material. In fiber reinforced materials, the intra-ply shearing is typically distinguished into two micro-mechanisms [17], [48], [13]. The first is longitudinal shearing which considers fibers sliding parallel to their orientation. The second is transversal shearing which considers relative fiber movement normal to the orientation direction (Figure 4-8). The two micro-mechanisms can result in very different shear properties. For instance, uni-directional composites such as thermoplastic UD tapes can be highly anisotropic with respect to the fiber orientation. In Tepex Flowcore, longitudinal and transversal mechanisms co-exist when intra-ply shearing takes place. With ideally random fiber orientation, contributions of the two mechanisms should be exactly same at 0 and 90 directions, creating isotropic shear properties. However, current fiber orientation analysis (Figure 4-6) suggests that longitudinal shearing can contribute more at 0 direction, while contributing less at 90 direction. In other words, intra-ply shearing behavior can be different in 90 and 0 directions. This reasoning leads to necessity of conducting shear characterization experiments toward both of the two objective directions.

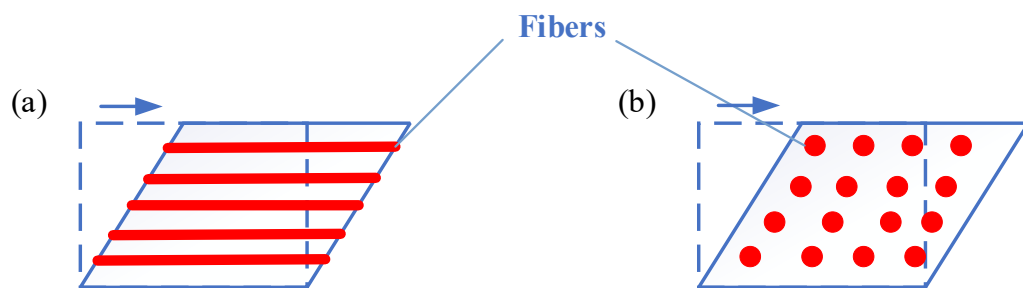


**Figure 4-8: Two intra-ply shearing mechanisms distinguished by (a) longitudinal shearing and (b) transversal shearing**

## 4.2 Sample Preparation and Experimental Procedures

Torsion bar specimens were cut from a single layer of Flowcore blank sheet. The specimens measure 60 mm in length, 12.7 mm in width and 2 mm in thickness (Figure 4-9). Due to the reasons explained in Section 4.1, two types of specimens were prepared — length along the 0 direction and length along the 90 direction. In this sense, the intra-ply shearing behavior can be characterized in these two directions. The torsion bar experiments were carried out on a rotational rheometer (Rheometrics Dynamic Spectrometer Model RDS II) with its standard fixture. The rheometer was also equipped with environmental chamber that allows testing at elevated temperatures. Figure 4-10 (Left) shows a specimen being fixed on equipment. Figure 4-10 (Right) presents a schematic drawing of the equipment (reproduced from user manual).

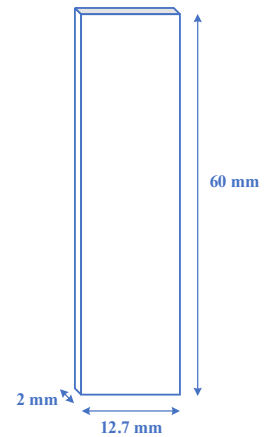


**Figure 4-9: Torsion bar specimen dimensions**

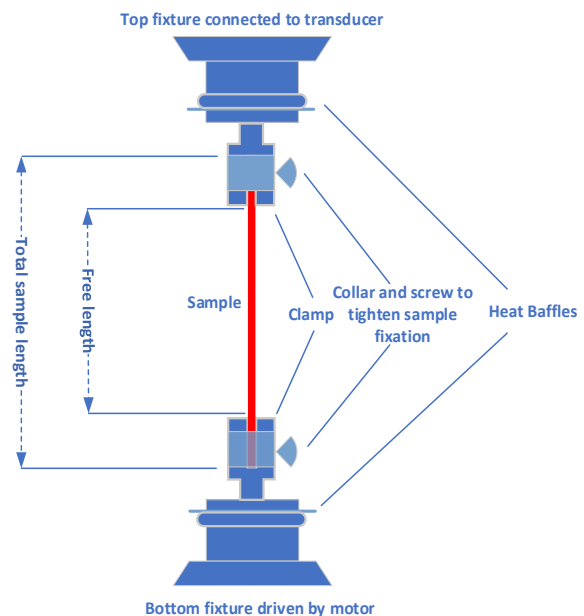


**Figure 4-10: (Left) picture of sample being installed on the fixtures, (Right) equipment schematic drawing reproduced from the user manual**

After a specimen was set up to the fixture, it was heated to and maintained in the molten state. Afterwards, large amplitude oscillatory shear (LAOS) tests were carried out. The function of arbitrary waveshape tests were used. The motor drove the bottom fixture to perform sinusoidal rotation periods under pre-fixed frequencies and amplitude angles. Based on amplitude angles, the machine was able to calculate corresponding strain amplitudes. For each rotational period, the transducer at top fixture measured and recorded the response torque curve, then automatically converted it to the stress curve. For each specimen, three strain amplitudes were each tested at three different frequencies. Moreover, to capture temperature-dependency of material properties, three testing temperatures were performed using more specimens. The detailed test matrix is given in table 4-2.

**Table 4-2: Detailed test matrix for oscillatory torsion bar tests**

	230 °C	250 °C	260 °C
<b>1% Strain Amplitude</b>	0.5 rad/s	0.5 rad/s	0.5 rad/s
	1 rad/s	1 rad/s	1 rad/s
	10 rad/s	10 rad/s	10 rad/s
<b>1.7% Strain Amplitude</b>	0.5 rad/s	0.5 rad/s	0.5 rad/s
	1 rad/s	1 rad/s	1 rad/s
	10 rad/s	10 rad/s	10 rad/s
<b>2.3% Strain Amplitude</b>	0.5 rad/s	0.5 rad/s	0.5 rad/s
	1 rad/s	1 rad/s	1 rad/s
	10 rad/s	10 rad/s	10 rad/s

Each test condition in Table 4-2 was repeated for three specimens cut in the 0 direction and three specimens cut in the 90 directions.

### 4.3 Data Analysis

Time domain data was collected from the experiments, which composed of strain vs. time and measured stress vs. time curves of each rotational period. Figure 4-11 shows a segment of strain curve and the corresponding stress curve in one of the tests. As can be seen from the figure, there is a phase lag between the strain and stress waves. The phase angle, however, is obviously smaller than  $90^\circ$  or  $\frac{1}{2}\pi$ . The phase angle within the range of  $0^\circ$  to  $90^\circ$  indicates viscoelastic behavior of the material. Furthermore, the shape of the stress curve is apparently distorted from a perfect sinusoidal wave (e.g. the strain curve in same graph). This distortion typically means that the material is within the large strain amplitude regime, thus having non-linear viscoelastic behaviors [50]. In fact, the distorted stress curves were observed among all three tested strain amplitudes. This phenomenon was anticipated, as the objective was to characterize material properties under large deformation.

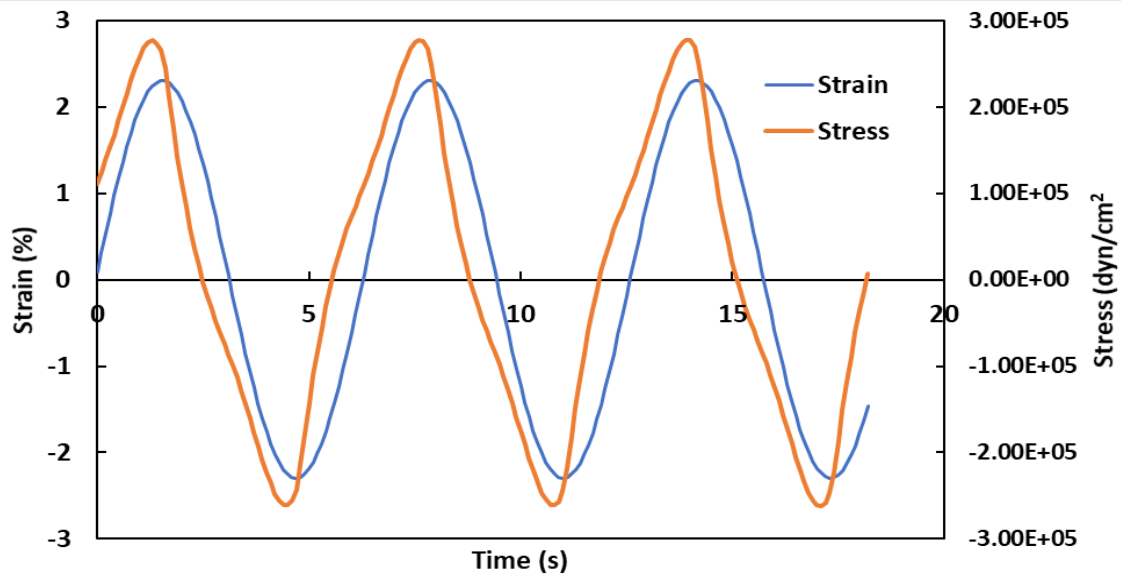


**Figure 4-11: Example strain and stress data collected from experiments**

In oscillatory rheometry, equations 4.1 and 4.2 are usually used for small strain tests to calculate storage and loss modulus, respectively. However, these equations were derived from the premise that stress curve is a sinusoidal wave in the form of equation 4.3.

$$G' = \frac{\sigma_0}{\gamma_0} \cdot \cos(\delta) \quad (4.1)$$

$$G'' = \frac{\sigma_0}{\gamma_0} \cdot \sin(\delta) \quad (4.2)$$

$$\sigma(t) = \sigma_0 \cdot \sin(\omega \cdot t + \delta) \quad (4.3)$$

This premise does not apply for the large strain regime, where the stress curve is no longer a purely sinusoidal function of time. Therefore, a different method needs to be developed.

The stress curve for LAOS data, although not purely sinusoidal, is still a periodic function of time. The function can be completely represented by a Fourier series given in equation 4.4 [51].

$$\sigma(t, \omega, \gamma) = \gamma_0 \cdot \sum_{n \text{ (odd)}} [G'_n \cdot \sin(n\omega t) + G''_n \cdot \cos(n\omega t)] \quad (4.4)$$

where  $\sigma$  is the stress,  $\gamma_0$  is the strain amplitude,  $G'_n$  and  $G''_n$  are Fourier series coefficients, and  $\omega$  the oscillatory frequency of strain signal. Here, only odd terms of the series are taken, because stress is assumed oddly symmetrical with respect to directionality of strain or strain rate [52]. Even terms would typically be considered for transient tests [53].

Furthermore, Cho et al. [54] has developed a method to decompose the total viscoelastic stress into superposition of two portions — the elastic portion and the viscous portion. In general, the time domain stress and strain data can be replotted with stress against strain, and also stress against strain rate. For example, Figure 4-12 and Figure 4-13 are plotted in this way using the data from Figure 4-11.

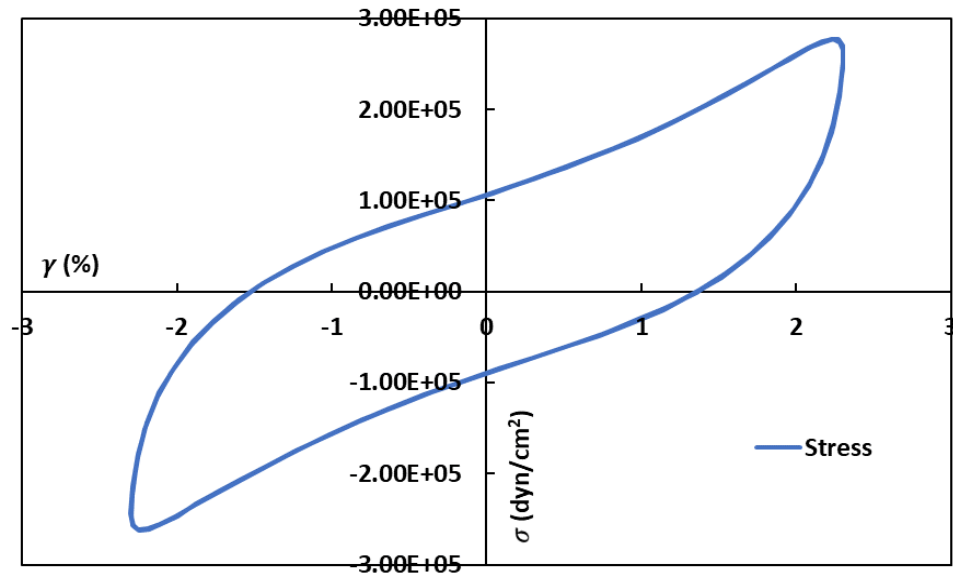


**Figure 4-12: Stress against strain plot using data from Figure 4-11**

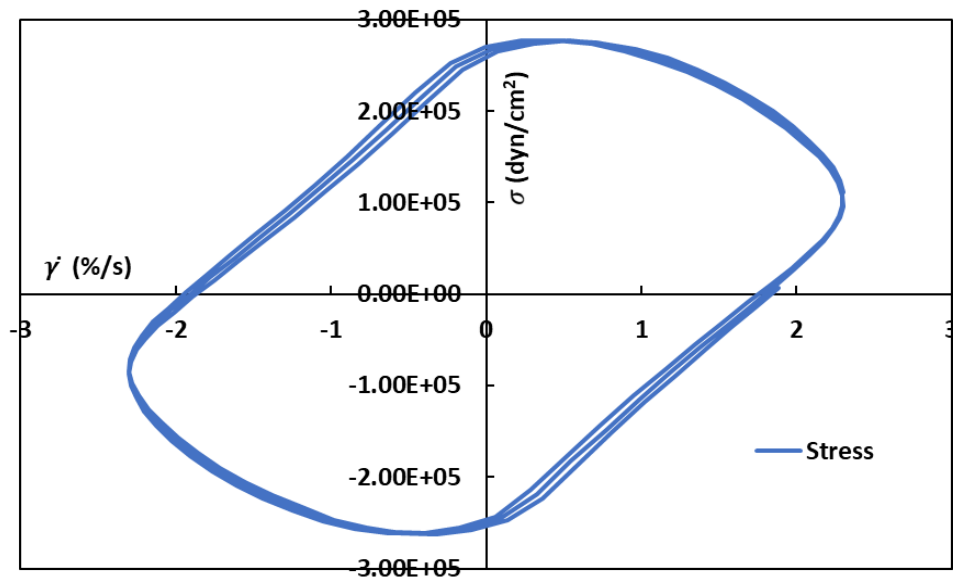


**Figure 4-13: Stress against strain rate plot using data from Figure 4-11**

Using the idea that elastic stress should be oddly symmetrical with respect to strain (or vertical axis in Figure 4-12) and evenly symmetrical with respect to strain rate (or vertical axis in Figure 4-13), whereas viscous stress should do the opposite, the two portions can be decomposed from total stress by the following equations [54]:

$$\sigma = \sigma' + \sigma'' \quad (4.5)$$

$$\sigma' = \frac{\sigma(\gamma, \dot{\gamma}) - \sigma(-\gamma, \dot{\gamma})}{2} \quad (4.6)$$

$$\sigma'' = \frac{\sigma(\gamma, \dot{\gamma}) - \sigma(\gamma, -\dot{\gamma})}{2} \quad (4.7)$$

Where  $\sigma$  is the total stress,  $\sigma'$  is the elastic stress portion,  $\sigma''$  is the viscous stress portion,  $\gamma$  the strain and  $\dot{\gamma}$  the strain rate.

Performing equation 4.6 to all data points in Figure 4-12 will generate a new set of data, representing elastic stress as a function of strain. It can be plotted as shown on Figure 4-14. Similarly, performing equation 4.7 to all data points in Figure 4-13 generates viscous stress as a function of strain rate, which is plotted in Figure 4-15.

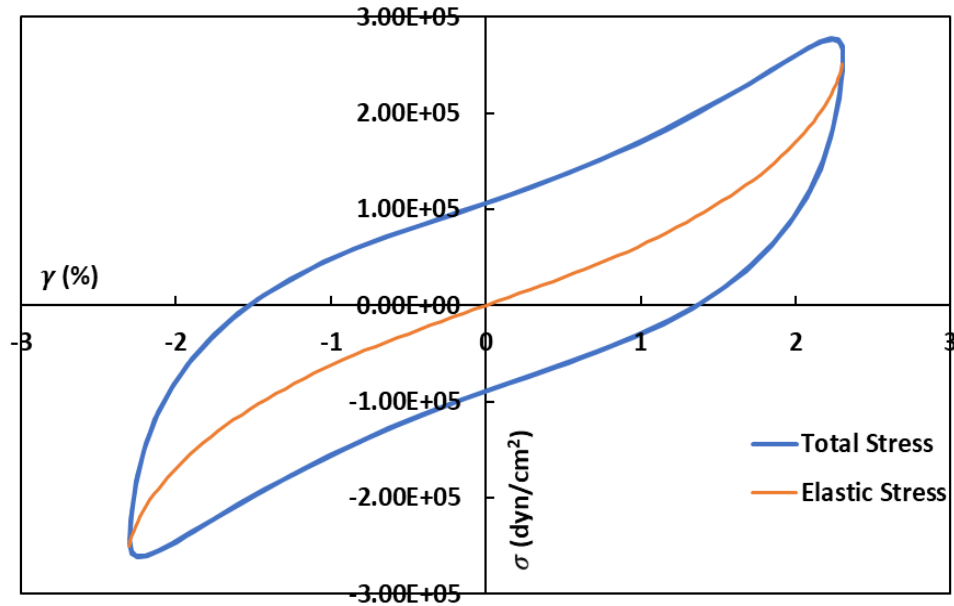


**Figure 4-14: Elastic stress decomposed from Figure 4-12 using equation 4.6**

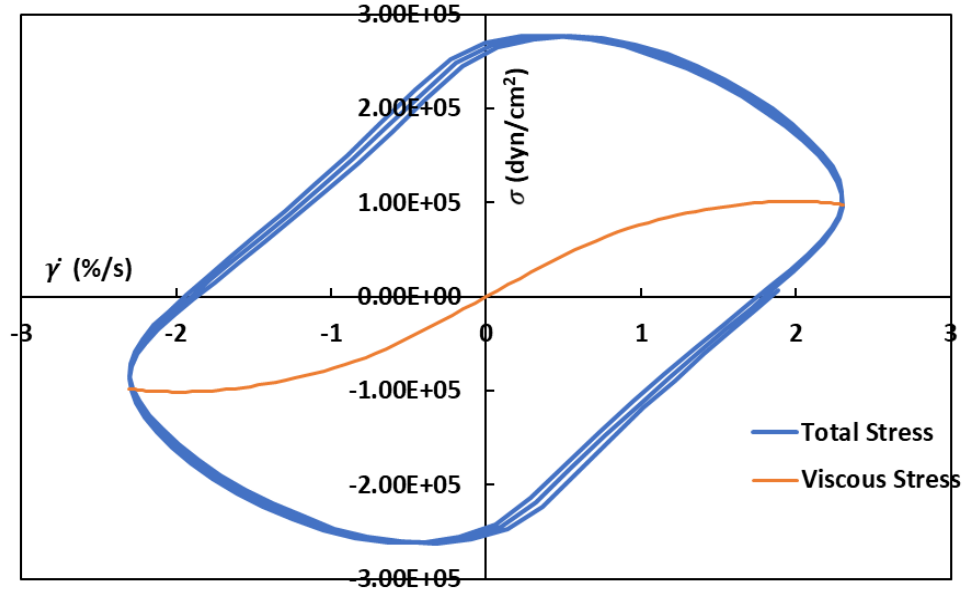


**Figure 4-15: Viscous Stress decomposed form Figure 4-13 using equation 4.7**

With elastic and viscous stress being decomposed as functions of strain and strain rate, the estimation of viscoelastic parameters can be performed. Recall that equation 4.4 transforms the stress signal into a Fourier series. Ewoldt et al. [50] found the Fourier series to be equivalent to the stress decomposition by relating to equations 4.6 and 4.7, such that:

$$\sigma' = \frac{\sigma(\gamma, \dot{\gamma}) - \sigma(-\gamma, \dot{\gamma})}{2} = \gamma_0 \cdot \sum_{n \text{ (odd)}} G'_n \cdot \sin(n\omega t) \quad (4.8)$$

$$\sigma'' = \frac{\sigma(\gamma, \dot{\gamma}) - \sigma(\gamma, -\dot{\gamma})}{2} = \gamma_0 \cdot \sum_{n \text{ (odd)}} G''_n \cdot \cos(n\omega t) \quad (4.9)$$

By doing so,  $G'_n$  can be viewed as elastic parameters linking elastic stress to the strain, while  $G''_n$  can be viewed as viscous parameters relating viscous stress and the strain rate. Fitting equations 4.8 and 4.9 with Chebyshev polynomials (equations 4.10 and 4.11, respectively) of the first kind allows the estimation of these parameters.

$$\sigma' = \gamma_0 \cdot \sum_{n \text{ (odd)}} e_n \cdot T_n(\sin(\omega t)) \quad (4.10)$$

$$\sigma'' = \dot{\gamma}_0 \cdot \sum_{n \text{ (odd)}} v_n \cdot T_n(\cos(\omega t)) \quad (4.11)$$



Ewoldt et al. [50] has developed software (MITlaos) to perform such fitting. The software was freely available and was used in this study. MITlaos was able to fit the polynomial to the third harmonic order. In other words,  $G'_1$ ,  $G'_3$ ,  $G''_1$  and  $G''_3$  were estimated.  $G'_3$  and  $G''_3$  are indicators of intra-cycle nonlinear behaviors under oscillatory conditions. These two parameters are of less importance to the draping simulation which considers a continuous deformation. On the other hand,  $G'_1$  and  $G''_1$  reflect the average viscoelastic properties within the cycle, which are equivalent to the often referred “elastic modulus” and “loss modulus” [50]. By dividing  $G''_1$  with the oscillatory frequency, the average viscosity  $\eta_1$  within the oscillatory cycle can be obtained (equation 4.12).

$$\eta_1 = \frac{G''_1}{\omega} \quad (4.12)$$

The parameters  $G'_1$  and  $\eta_1$  can now be regarded as the shear modulus and shear viscosity, which are typically characterized and used in viscoelastic models (e.g. the Kelvin Voigt model) to predict draping behavior of thermoplastic composites [5]. For the purpose of this study, it is also necessary to identify the shear rate dependency of the two parameters. Since  $G'_1$  and  $\eta_1$  represent average elasticity and viscosity during oscillation, it is reasonable to match them with an average shear rate extracted from the oscillatory cycle. Just like shear strain, the shear rate during oscillation is a sinusoidal function of time given in equation 4.13.

$$\dot{\gamma} = \dot{\gamma}_0 \cos(\omega t) \quad (4.13)$$

To extract an average shear rate, the root mean square average (RSMA) of equation 4.13 is used. For sinusoidal functions, the RSMA is the amplitude divided by  $\sqrt{2}$ , therefore:

$$\dot{\gamma}_{ave} = \frac{\dot{\gamma}_0}{\sqrt{2}} \quad (4.14)$$

For each set of test frequency and strain amplitude, equation 4.14 was used to find an average shear rate that matches the characterized elastic modulus and viscosity.

## 4.4 Characterization Results and Discussions

Using the data analysis method explained in section 4.1, the elastic modulus and viscosity were characterized for all conditions listed by table 4-2. As was mentioned, each test condition was repeated on three 0 direction specimens and three 90 direction specimens. For each specimen type, the finalized material properties were obtained as the arithmetic means of the results generated by the three experimental replicates. As an example, table 4-3 summarizes the characterization results from all 90 direction specimens tested at 230 °C, as well as the finalized material properties under this temperature. In addition, the RSMA shear rate is included for each combination of frequency and strain amplitude.

**Table 4-3: Results from all 90 direction specimens tested at 230 °C**

230 C, 90 Degree Samples							
		0.5 rad/s		1 rad/s		10 rad/s	
		G (Mpa)	Viscosity (Mpa.s)	G (Mpa)	Viscosity (Mpa.s)	G (Mpa)	Viscosity (Mpa.s)
1% Strain Amplitude	#1	1.41	2.10	1.42	1.11	2.07	0.23
	#2	0.90	1.70	0.91	0.93	1.45	0.22
	#3	1.02	1.52	1.02	0.82	1.53	0.19
	Avg	1.11	1.77	1.12	0.95	1.68	0.21
	RMSA Shear Rate (1/s)	0.00354		0.00707		0.0707	
1.7% Strain Amplitude	#1	1.17	1.56	1.20	0.86	1.82	0.20
	#2	0.70	1.25	0.71	0.72	1.25	0.2
	#3	0.82	1.15	0.84	0.66	1.34	0.18
	Avg	0.90	1.32	0.92	0.75	1.47	0.19
	RMSA Shear Rate (1/s)	0.00601		0.0120		0.120	
2.3% Strain Amplitude	#1	1.29	1.41	1.30	0.78	1.97	0.18
	#2	0.65	1.09	0.68	0.64	1.24	0.19
	#3	0.81	1.03	0.84	0.60	1.37	0.17
	Avg	0.92	1.18	0.94	0.67	1.53	0.18
	RMSA Shear Rate (1/s)	0.00813		0.0163		0.163	

As can be seen, the RSMA shear rate increases with greater frequencies or greater strain amplitudes. The combination of these two test conditions has generated many data points for studying shear rate dependency of material properties. After finalizing material properties for all specimen types and test conditions, the complete characterization results of elastic modulus are plotted against shear rate in Figure 4-16.

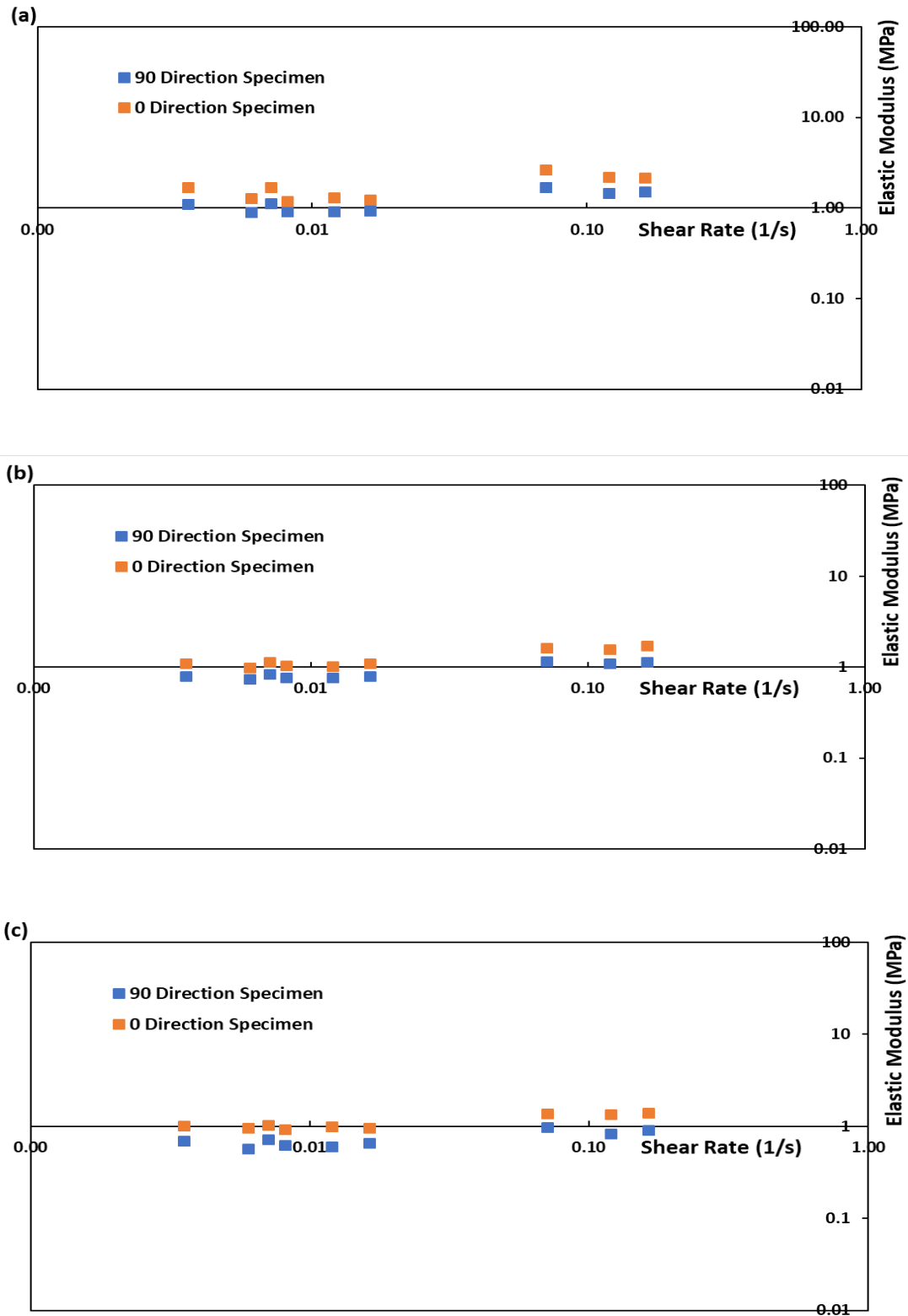
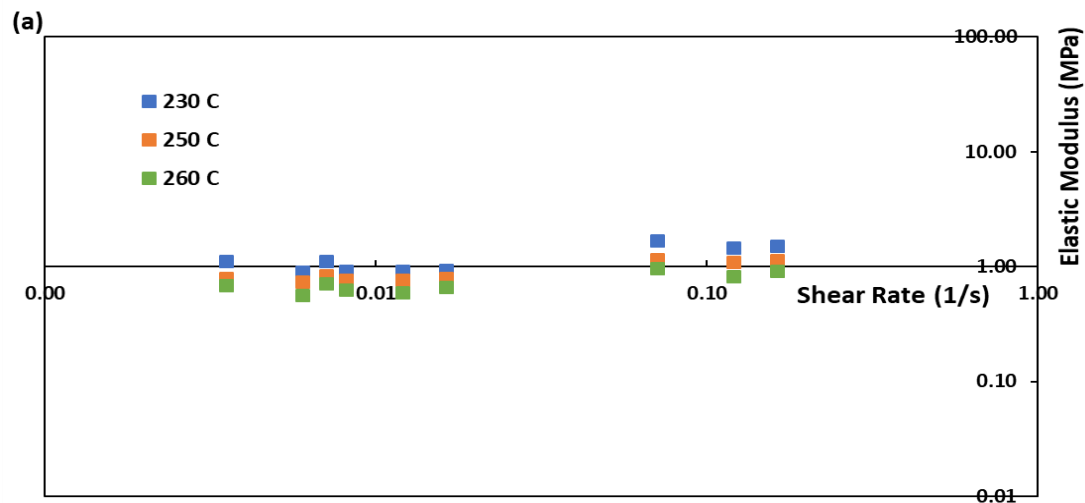
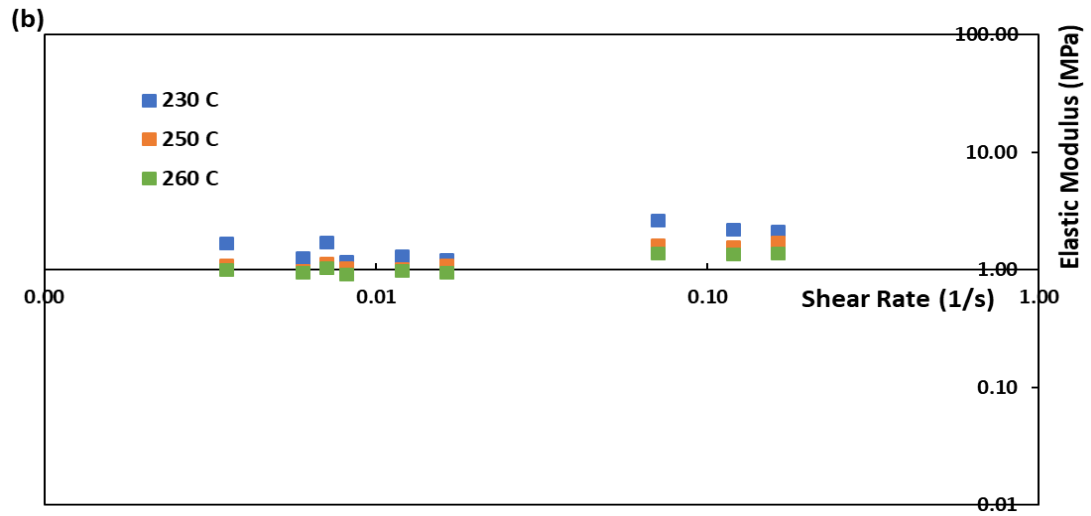


Figure 4-16: Elastic modulus characterized for 0 and 90 direction samples under (a) 230 °C (b) 250 °C and (c) 260 °C

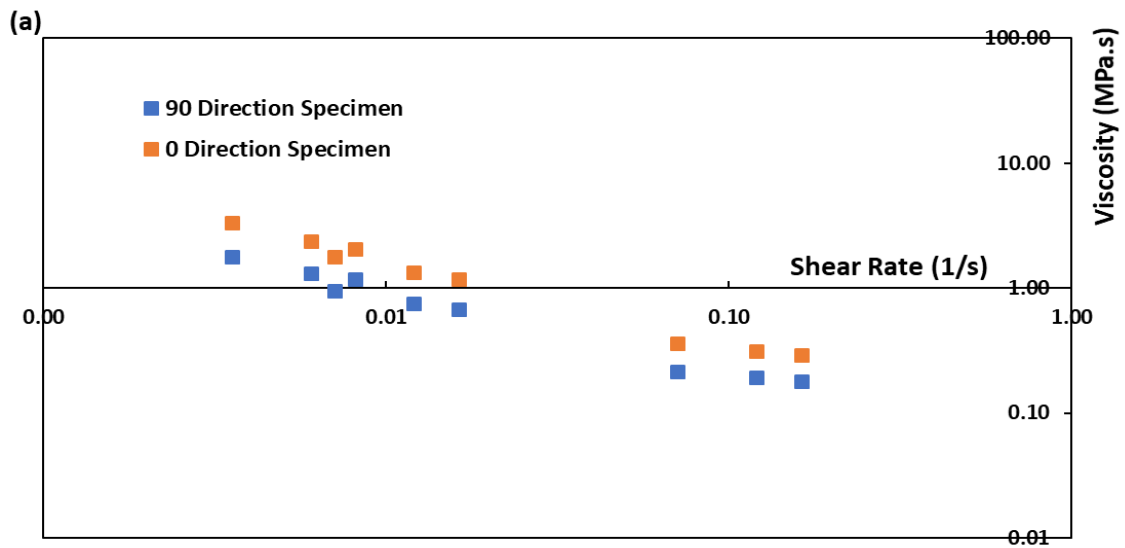
Relatively low values have been characterized for the elastic modulus. At all three tested temperatures, the elastic modulus presents an increasing trend with increasing shear rate. However, the trend is not pronounced, especially at higher temperatures and relatively low shear rate range. Another noticeable point is the elastic modulus in 0 direction being consistently higher than elastic modulus in 90 direction. This fits the reasoning in section 4.1, that more fibers oriented in the 0 direction resulted in greater contributions from longitudinal shearing than transversal shearing, and consequently larger shear properties in this direction. Nevertheless, for elastic modulus at this magnitude, the viscoelastic modelling (e.g. Kelvin Voigt model) of draping behavior can be less sensitive to its impact [5]. Therefore, it is possible to just consider a constant elastic modulus by taking the average value of data points at each temperature. In this case, one could take the options to distinguish or ignore the differences between 0 and 90 directions. The temperature dependency of elastic modulus, however, is necessary to be considered as it can be obviously seen in Figure 4-17 (on log scale plots, normal scale plots are also given in appendices as a reference). Furthermore, the material temperature can change dramatically during forming stage (studies in Chapter 3), which can create much more variations on material properties.





**Figure 4-17: Temperature dependency of elastic modulus on (a) 90 direction specimen and (b) 0 direction specimen**

The viscosity values were also characterized at all test conditions and plotted against the shear rate, given in Figure 4-18.



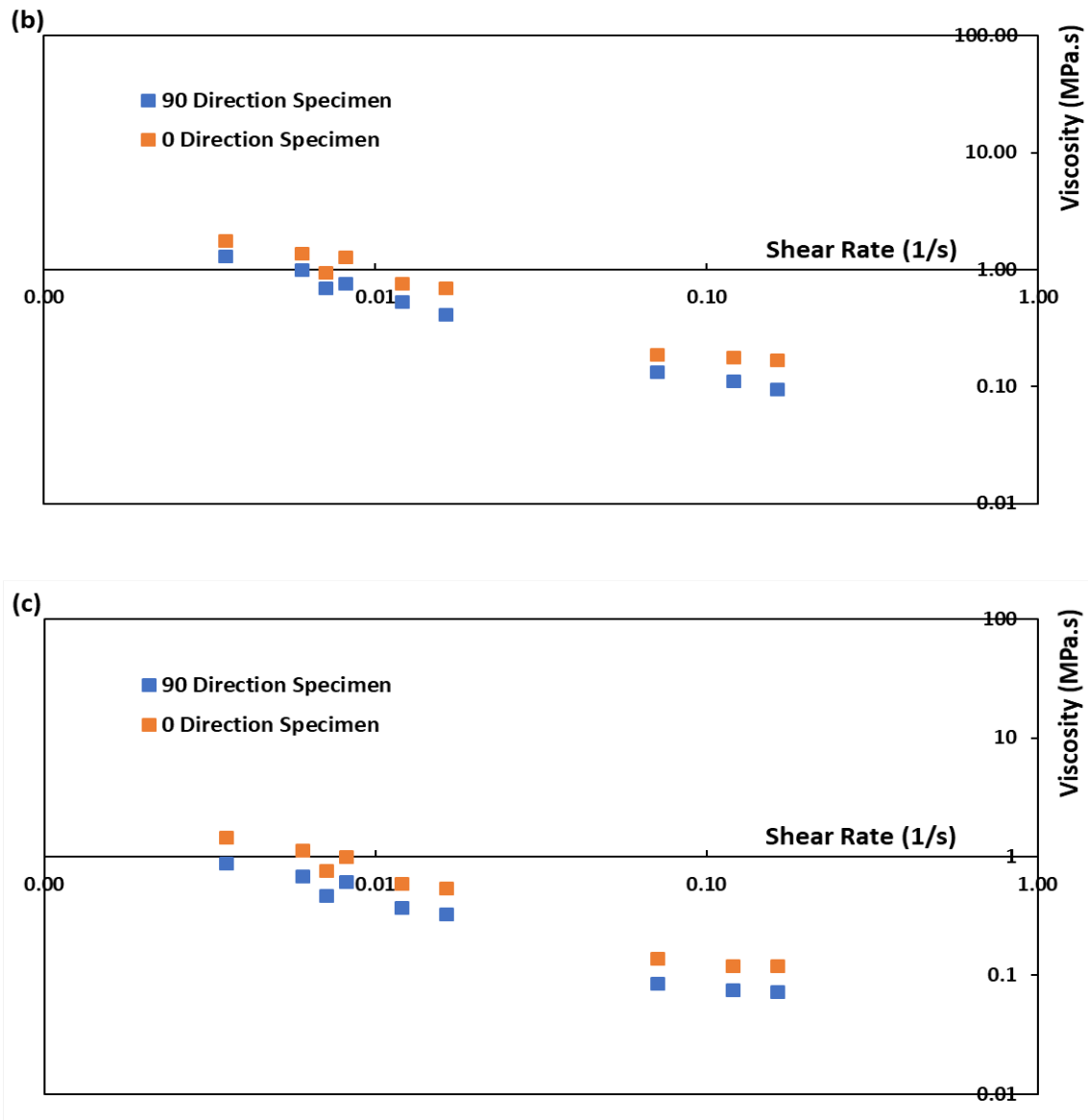


**Figure 4-18: Viscosities characterized for 0 and 90 direction samples under (a) 230 °C (b) 250 °C and (c) 260 °C**

The viscosity, unlike elastic modulus, has exhibited large dependency on the shear rate. The decreasing viscosity values with higher shear rates can be characterized as a shear thinning behavior. It is a common phenomenon observed for polymer melts. Typically, polymer chains tend to disentangle and align toward the shear direction, which lead to drops in apparent viscosity. In the case of thermoplastic composites, fibers can have similar behavior and contribute to shear thinning, especially when material is forced to

flow [55]. Within the tested shear rate range, the decline of viscosity appears almost linear on logarithmic plots (Figure 4-18). This means the characterized viscosity values can be approximated by a power-law or Cross model, which allows extrapolation to a broader range of shear rate.

Similar to the case of elastic modulus, the viscosity of 0 direction specimen is constantly higher than the viscosity of 90 direction specimen under all temperatures. This again validates the assumption of anisotropic shear properties made in section 4.1. Furthermore, the temperature dependency of viscosity is clearly observed for both types of specimen (Figure 4-19), thus must be considered for modeling and simulation.

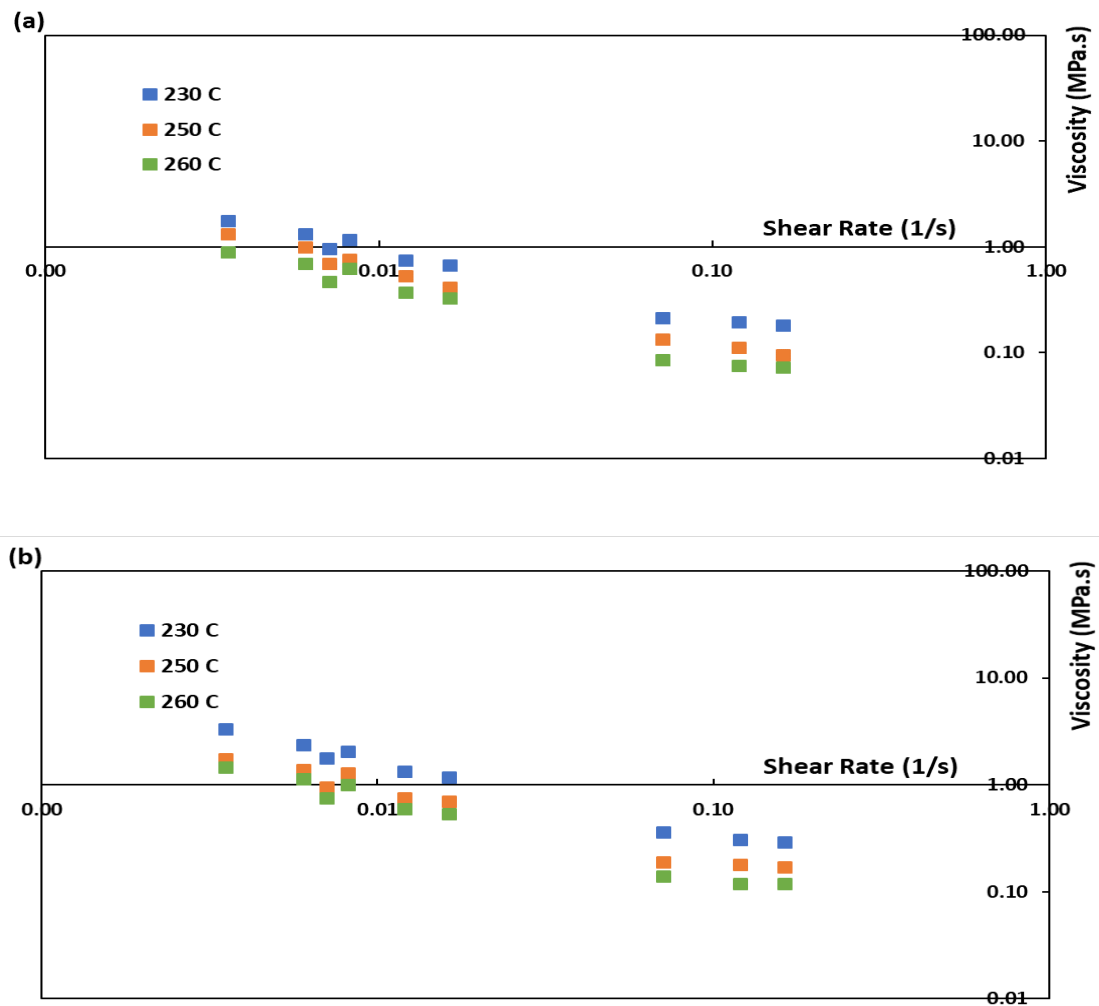


**Figure 4-19: Temperature dependency of viscosity on (a) 90 direction specimen and (b) 0 direction specimen**

## 4.5 Generation of Material Cards

The elastic modulus and viscosity values characterized in previous sections can be used to create material cards that serve as input of forming simulations. Instead of direct input as tabulated data, a more commonly used method is to fit property models and generate model parameters. As was discussed in section 4.4, the elastic modulus of Tepex Flowcore can be considered independent of shear rate. The temperature dependency is a more important factor. In this consideration, the elastic modulus was fitted to the Williams–Landel–Ferry (WLF) equation (equation 4.15), which is a commonly used model for temperature dependency.

$$G(T) = D_1 \cdot \exp \left( - \left( \frac{A_1 \cdot (T - D_2)}{A_2 + T - D_2} \right) \right) \quad (4.15)$$

where  $G(T)$  is the temperature dependent modulus,  $T$  is the temperature,  $A_1$ ,  $A_2$ ,  $D_1$  and  $D_2$  are model parameters.

The Cross model has been widely used for fitting viscosity. It is well known for being able to include both the Newtonian regime and shear thinning regime of polymer melts. In combination of the WLF equation, a Cross-WLF approach was used to capture both shear rate and temperature dependency of the viscosity data. (equations 4.16 and 4.17).

$$\eta(\dot{\gamma}) = \frac{\eta_0}{1 + \left( \frac{\eta_0 \cdot \dot{\gamma}}{\tau^*} \right)^{1-n}} \quad (4.16)$$

Where

$$\eta_0(T) = D_1 \cdot \exp \left( - \left( \frac{A_1 \cdot (T - D_2)}{A_2 + T - D_2} \right) \right) \quad (4.17)$$

Equation 4.16 is the Cross model which describes shear rate dependency of viscosity. The parameter  $n$  is the flow index in shear thinning regime, parameter  $\tau^*$  is the critical stress at the Newtonian plateau and  $\eta_0$  is the constant viscosity in this regime. Equation 4.17 determines the value of  $\eta_0$  based on temperature, which adds temperature dependency to the cross model.



In this study, the temperature dependency of elastic modulus was only characterized with three data points (three test temperatures). Fitting all four parameters of the WLF equation to the elastic modulus data would be difficult and might create overfitting problems. Fixing some of the parameters with reasonable values would help address this issue. For polymer melts,  $D_2$  can usually use the glass transition temperature [56]. Given this premise,  $A_1$  and  $A_2$  can also be fixed at the values provided by Osswald et al. [56], leaving  $D_1$  the only parameter to be fitted.

When fitting of viscosity data, this technique was used again for the WLF part. In addition,  $\tau^*$  in the Cross part was fixed at specially selected values to prevent the viscosity value at Newtonian regime being too high. Details of fixed and fitted parameters for modulus and viscosity data are summarized in table 4-4. The fitting was evaluated and optimized by relative square error.

**Table 4-4: Fixed and fitted parameters used for elastic modulus and viscosity data**

Parameters	Elastic Modulus	Viscosity
$D_1$	fitted	fitted
$D_2$	60 °C (T <sub>g</sub> )	60 °C (T <sub>g</sub> )
$A_1$	31.141 [56]	31.141 [56]
$A_2$	51.6 °C [56]	51.6 °C [56]
$\tau^*$	-	0.001 MPa
$n$	-	fitted

The fitted models of elastic modulus and viscosity can be used to construct nonlinear viscoelastic models (e.g. Kelvin Voigt model) to simulate the draping behavior of Tepex Flowcore during compression molding process. When necessary, the models can also be extrapolated to predict material properties in a wider shear rate or temperature range. The fitted curves are summarized in Figures 4-20 and 4-21, the fitted parameters are given in

tables 4-5 and 4-6. It should be noted that the extrapolation of elastic modulus is only applicable above recrystallization temperature (around 190 °C or the red lines in Figures 4-20 and 4-21).

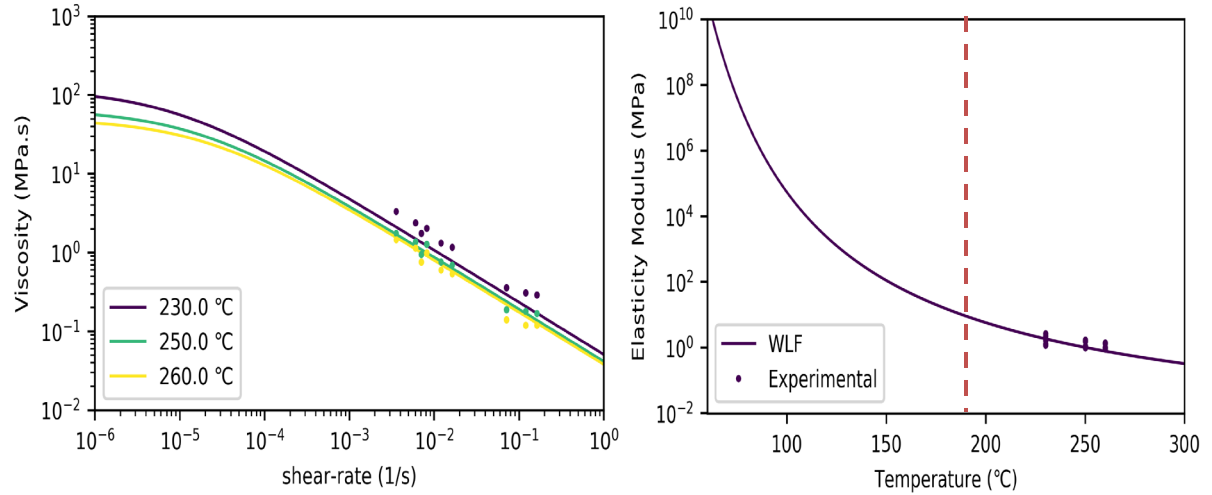


**Figure 4-20: Fitting of 0 direction properties (left) Cross-WLF for viscosity and (right) WLF for elastic modulus**

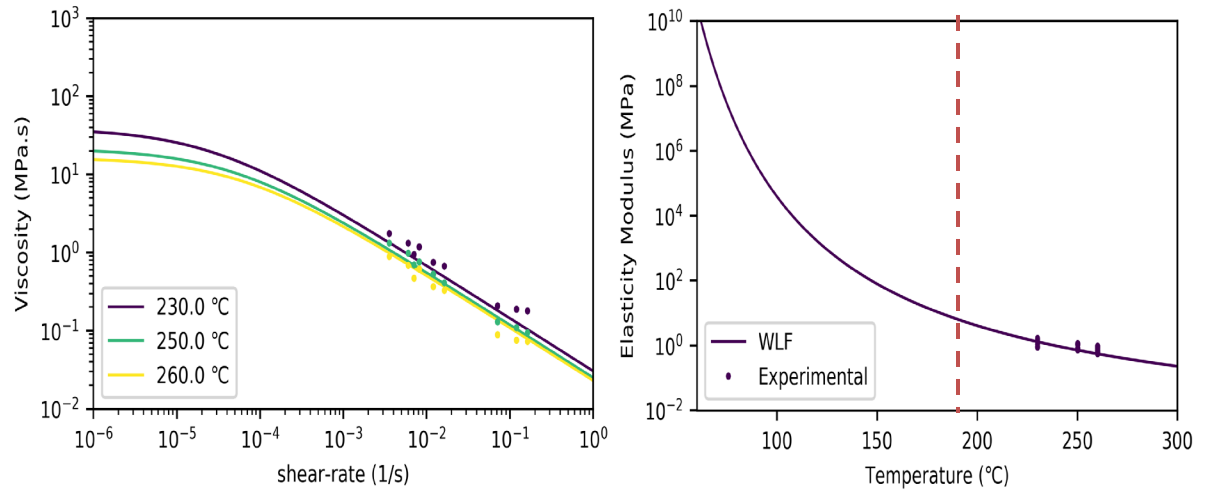


**Figure 4-21: Fitting of 90 direction properties (left) Cross-WLF for viscosity and (right) WLF for elastic modulus**

**Table 4-5: Fitted parameters for 90 direction and 0 direction**

Fitted Parameters	Elastic Modulus		Viscosity	
	90 Direction	0 Direction	90 Direction	0 Direction
$D_1$	$3.12 \times 10^{10}$ MPa	$4.39 \times 10^{10}$ MPa	$9.25 \times 10^{11}$ MPa·s	$2.83 \times 10^{12}$ MPa·s
$n$	-	-	0.32	0.34

## 4.6 Comparison of Different Methods

Apart from the characterization method developed in this chapter, Tepex Flowcore has been characterized for intra-ply shearing behaviors using different techniques, specifically, the torsion method presented by Haanappel et al [17] and the bending method presented by Saches et al [24]. These characterizations were completed by Susanne Lüssenheide and other collaborators at KIT and Fraunhofer ICT. Although using different fixtures, the two methods share similar concepts, which involves capturing torque vs. angle curve in a steady rotation. Afterwards, virtual experiments were simulated in finite element software (Abaqus CAE) with custom constitutive models (Kelvin-Voigt approach). Finally, elastic modulus and viscosity were characterized by reverse model fitting. Dörr et al. [5] found that the property set generated by bending method can successfully predict some local wrinkling on the draped parts. This suggests that the parameters characterized by the bending method are relatively accurate.

To examine the method developed in this study, the characterized material properties were compared with data from the bending (RB [5]) technique, which was generously provided by Dörr et al. and other collaborators at KIT/ICT. A graphical comparison of the data is given in Figures 4-22 and 4-23. The RB tests were only conducted in 90 direction. Therefore, the comparison was made using 90 direction properties generated in this study. As can be seen from the figures, elastic modulus characterized by the two methods are within the same order of magnitude (within the range 1-10 MPa), with this study being several times lower at same shear rates. The RB test indicates a more obviously increasing trend of the elastic modulus as shear rate increases. However, as

was mentioned in section 4.4, draping simulations would not be sensitive to elastic modulus of such small magnitudes. With regard to viscosity, the two tests both characterized a shear thinning behavior, and yielded very close values (with this study being only 1-2 times higher than the RB test at same shear rates). Overall, the viscoelastic properties characterized by this study are similar to those by the RB test. Obtaining close property values to a validated method from literature can be considered a validation aspect to the method from this study.

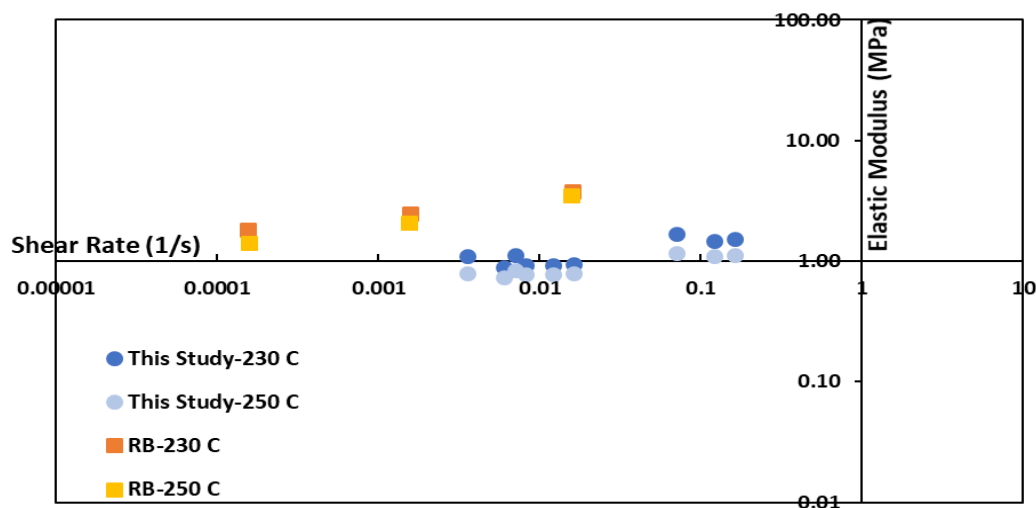


**Figure 4-22: Comparison of elastic modulus with RB test**

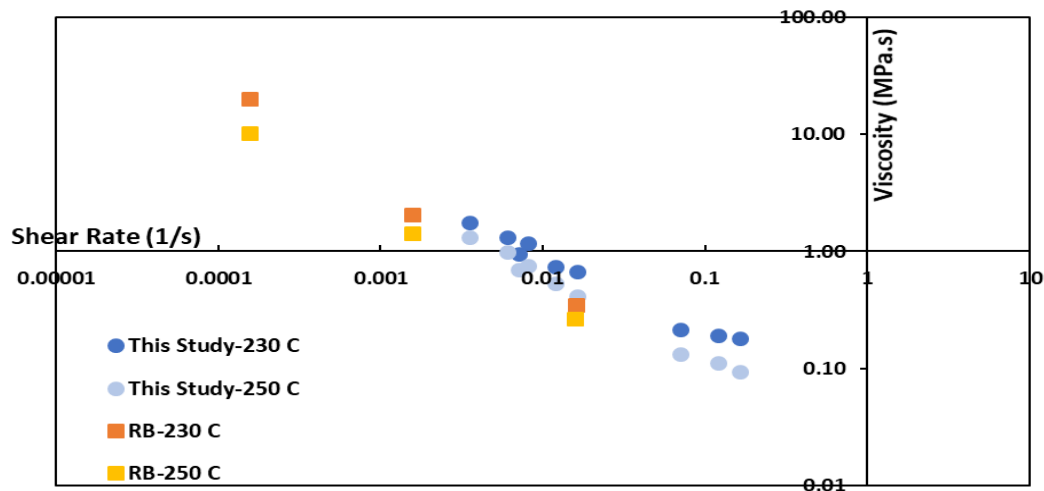


**Figure 4-23: Comparison of viscosity with RB test**

## 4.7 Conclusions

In this chapter, a method was developed to characterize the intra-ply shearing behavior of selected GMT material, and consequently, generate material properties used in draping simulations. Samples from two directions were prepared to address the anisotropy brought by uneven fiber orientation. Stress-Strain data was collected from large amplitude oscillatory torsion bar tests using a rotational rheometer. Different frequencies and strain amplitudes were used to create a range of shear rates. Three temperatures were tested to capture the temperature dependency of material properties. The collected data was analysis based on theories of Cho et al. [54] and Ewoldt et al. [50] to estimate viscoelastic properties under large deformation. The elastic modulus was found to be low in magnitude and having not much dependency on shear rate. The viscosity, however, was highly shear thinning. As a result, elastic modulus was fitted to a WLF approach to only capture the temperature dependency, whereas the viscosity was fitted to a Cross-WLF model that includes the impact of both shear rate and temperature. These fitted parameters generated materials card that can be used to construct constitutive models for draping simulation. Finally, the characterization results were compared with results from another method [5], [24] using the same material. The comparison could partly validate the method developed by this study. However, it is recommended to do further validation by inputting the characterization results into draping simulations, then comparing simulation results against draping experiments.

## Chapter 5

### 5 Material Characterization for Flow Simulations

As was discussed in Chapter 4, the compression molding of GMT sheets can be divided into two phases — draping and flowing. Compared to the draping phase, the flowing phase involves a much greater press force that squeezes the material to flow and fill the cavity. The accurate simulation of flowing phase helps predict warpage and fiber orientation in molded parts [14]. In simulations of compression molding, the material is usually considered a fluid. Therefore, the apparent viscosity of the composite under flow must be characterized as essential simulation input. To distinguish this viscosity parameter from the parameter characterized in Chapter 4, it is referred to as the ‘press viscosity’ in this chapter. Squeeze flow rheometry is a commonly used technique for this purpose. By measuring press force, press velocity and gap distance, the press viscosity of the squeezed material can be estimated. Radial flow is commonly used in many experimental set-ups, however this flow pattern is not suitable for anisotropic materials. On the other hand, 1-D flow set-ups have also been invented, which can target toward interested directions of an anisotropic material. For example, Kalaidov et al. [57] developed such a method for D-LFT (direct long fiber thermoplastic) materials by making use of the hydraulic press and plaque mold at Fraunhofer Project Center (Figure 5-1).

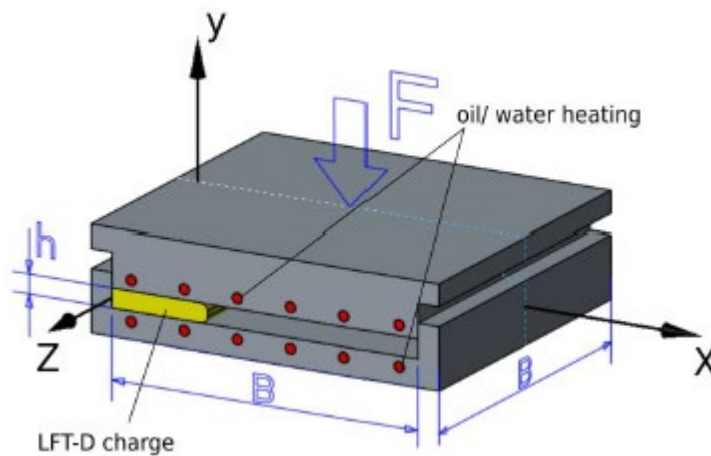


**Figure 5-1: 1-D flow characterization set-up developed by Kalaidov et al. [57]**

In this chapter, the same method and equipment will be adopted to perform flow characterization on the selected GMT sheet (Tepex Flowcore, features were given in Chapters 3 & 4). Afterwards, the estimated press viscosity will be fitted with a power-law model for flow simulation.

## 5.1 Sample Preparation and Experimental Set-up

The hydraulic press (Dieffenbacher DCP-U 2500/2200) and the plaque mold at Fraunhofer Project Center were used to perform the experiments. The mold has a square dimension with 457 mm side-length and 15 mm cavity depth. Rectangular pieces were cut from Flowcore sheets and were stacked to make squeeze flow charges. The length of the charge was made the same as the side-length of mold, the width was 150 mm and the stacked charge height was 12 mm. The charge was placed with its length along one side of the mold (Figure 5-2) to force a 1-D flow. Figure 5-2 illustrates the experimental set-up.

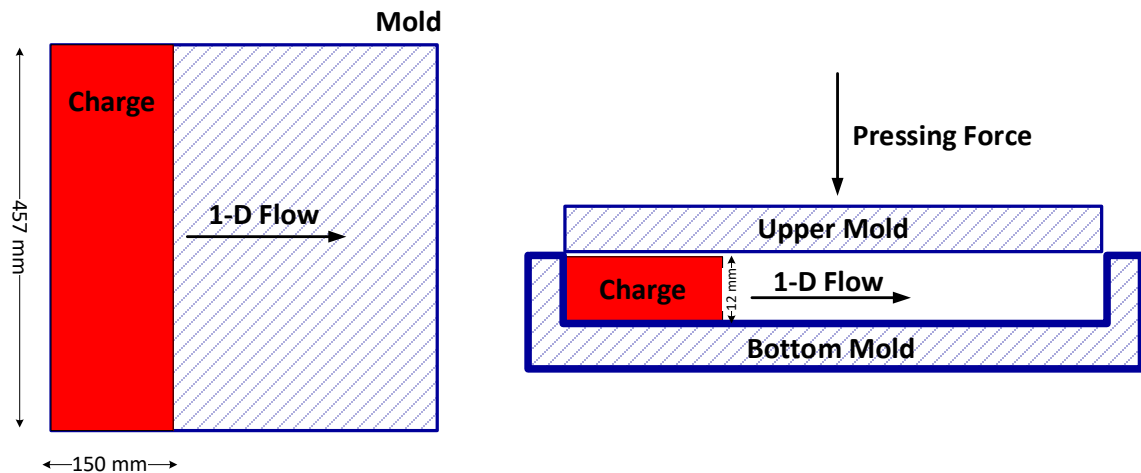


**Figure 5-2: Experimental set-up for 1-D squeeze flow of Tepex Flowcore**

Prior to the squeeze flow tests, the charges were heated in a forced convection oven to above its melting temperature. Two charge temperatures were tested — 260 °C and 300 °C. Thermal modeling results from Chapter 3 were used to determine heating times, which ensured the charge reached the target experimental temperatures (i.e. homogeneous temperature distribution).

Again here, the anisotropic material properties discovered in Chapter 4 makes it necessary to characterize flow behavior in both 0 and 90 directions of the sheet. All layers in one stack were placed to flow in the same target direction, i.e. all 0 or all 90. In addition, the possible effect of different stacking styles was examined. Two types of stacks were used to prepare the 12 mm charge height — 6 layers of 2 mm sheets and 4 layers of 3 mm sheets. A summary of the test matrix is given in table 5-1.

**Table 5-1: Test matrix of squeeze flow**

	6 x 2 mm Stack	4 x 3 mm Stack
<b>260 °C</b>	90/0	90/0
<b>300 °C</b>	90/0	90/0

Settings used on equipment during all the tests are summarized below:

- Fast mold closing (before mold contacted the charge): 550 mm/s
- Slow mold closing (initial speed after contact of the charge): 15 mm/s
- Maximum force build-up after contact of the charge: 3132 kN
- Mold temperatures (upper & lower): 150 °C

It is to be mentioned that the switch between ‘fast’ and ‘slow’ mold closing must be done manually to perform the experiments. The ‘fast’ closing also means the press is under speed control, whereas ‘slow’ closing also represents force control mode. Therefore, after upper mold contacts the charge and continues to squeeze, the actual closing speed can no longer be maintained at 15 mm/s. The actual closing speed during squeezing can only be read from press recordings (e.g. Figure 5-3).

## 5.2 Data Analysis

The press itself was able to measure and record three time-dependent data sets required by press viscosity estimation:

- Mold closing speed  $\dot{h}$



- Pressing force  $F$
- Ram position  $h$  (the gap distance between upper and bottom molds)

A relatively smooth portion needed to be selected from each data set for the estimation. An example is given in Figure 5-3.

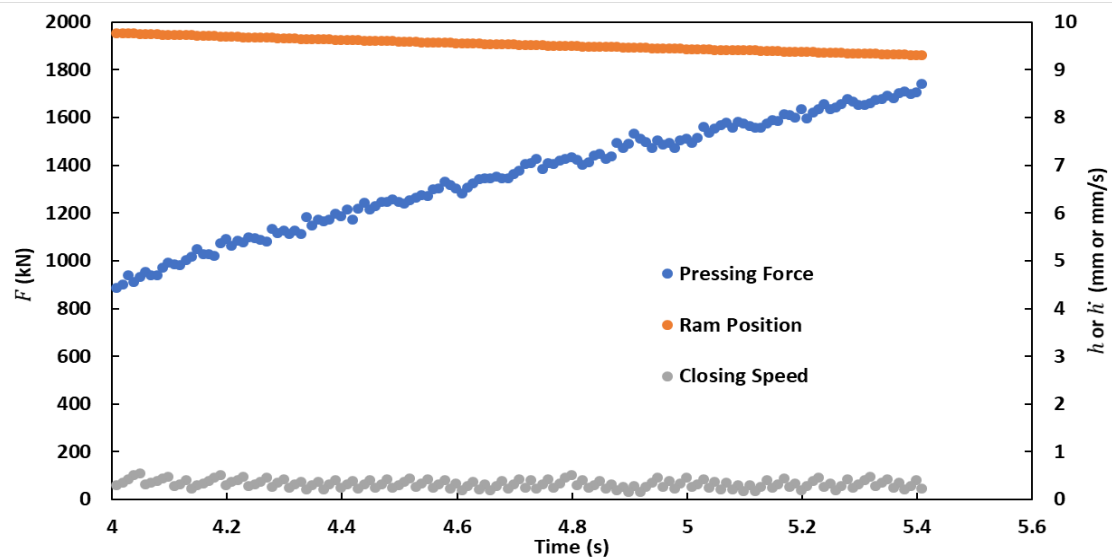


**Figure 5-3: Example data sets collected from press during squeeze flow experiments**

To perform the viscosity estimation method, some assumptions must be made for the 1-D flow problem. The assumptions are:

- The charge is an incompressible fluid
- The problem is assumed isothermal
- The pressing speed is low enough to ignore the inertia effects.
- The flow is purely one dimensional. In other words, flow is only toward positive  $x$  direction. No flow takes place in the  $z$  direction (Figure 5-4).
- No slip at walls (Figure 5-4).

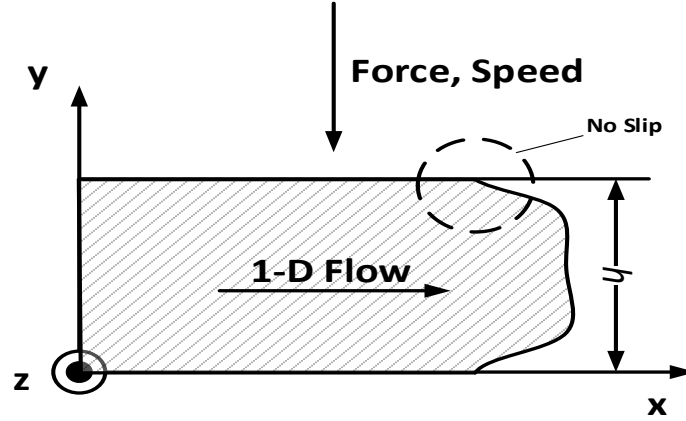


**Figure 5-4: Coordinates and variables in the 1-D flow problem**

With the above assumptions and the studies on the “fountain flow effect” of polymer melts [58], [59], [60], the wall shear rate and shear stress at the flow front can be derived for this 1-D flow. The detailed derivations can be found in the works of Klaidov et al. [57]. The wall shear stress is given as:

$$\tau_w = \frac{F \cdot B \cdot h^3}{2 \cdot k \cdot V^2} \quad (5.1)$$

In equation 5.1,  $B$  is the width of the flow which is simply the side-length of the mold (457 mm).  $V$  is the total volume of the flow. Since the charge was assumed incompressible,  $V$  remains constant at the initial charge volume (457 mm x 150 mm x 12 mm).  $k$  is an adjustable model parameter and is assumed a value of 1/3 here [57].

For Newtonian fluids, the velocity profile at flow front can be considered a parabola during squeeze flow (Figure 5-5). Based on this, the Newtonian wall shear rate  $\dot{\gamma}_{nw}$  under specified 1-D flow can be given in equation 5.2.

$$\dot{\gamma}_{nw} = \frac{6 \cdot V \cdot \dot{h}}{B \cdot h^3} \quad (5.2)$$

However, for non-Newtonian fluids like thermoplastic composites, the velocity profile deviates from a parabolic shape (Figure 5-5). Therefore, equation 5.2 must be corrected to get the true shear rate  $\dot{\gamma}_{tw}$  at wall. The Weissenberg-Rabinowitsch correction is used here for the purpose (Equation 5.3)

$$\dot{\gamma}_{tw} = \frac{\dot{\gamma}_{nw}}{3} \left( 2 + \frac{d(\ln \dot{\gamma}_{nw})}{d(\ln \tau_w)} \right) \quad (5.3)$$

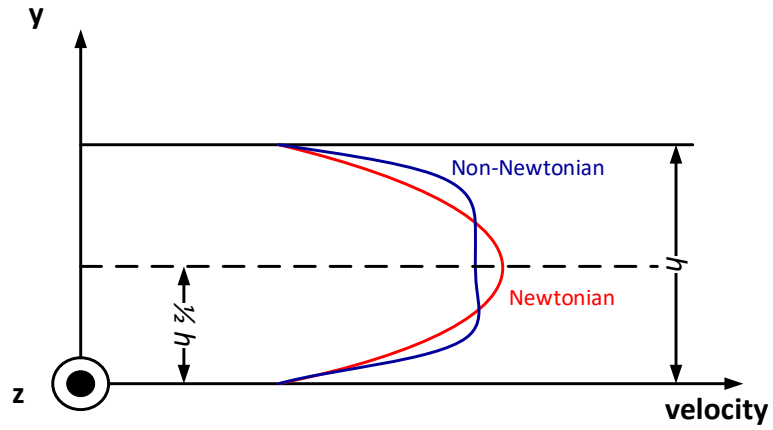


**Figure 5-5: Newtonian (red) and non-Newtonian (blue) velocity profiles at flow front during squeeze flow**

Finally, the viscosity can be calculated by its definition given in equation 5.4.

$$\eta = \frac{\tau_w}{\dot{\gamma}_{tw}} \quad (5.4)$$

By fitting equations 5.1, 5.2, 5.3 and 5.4 to the data set in Figure 5-3, a range of shear rate data points can be obtained with press viscosity calculated on each point. Figure 5-6 plots the viscosity estimation on logarithmic scale.

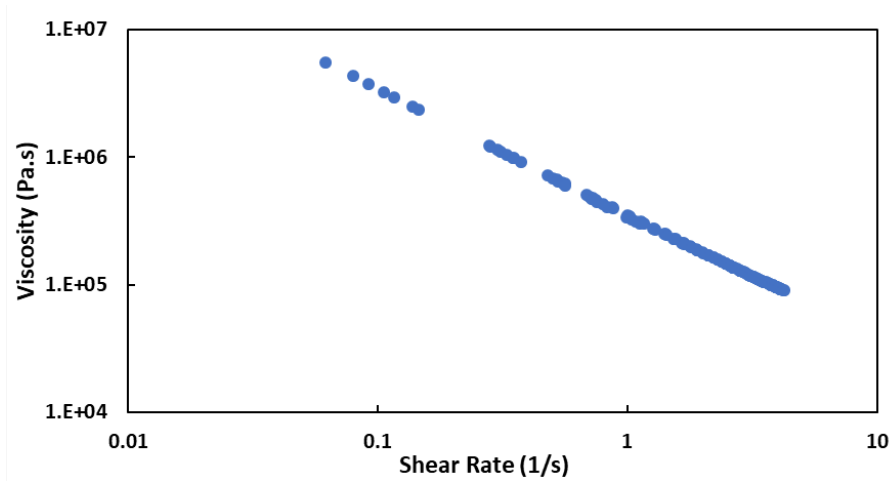


**Figure 5-6: Press viscosity estimation using the data in Figure 5-3**

### 5.3 Results and Discussion

Using the data analysis method explained in section 5.2, press viscosity was evaluated for each test condition. Figure 5-7 summarizes the results.

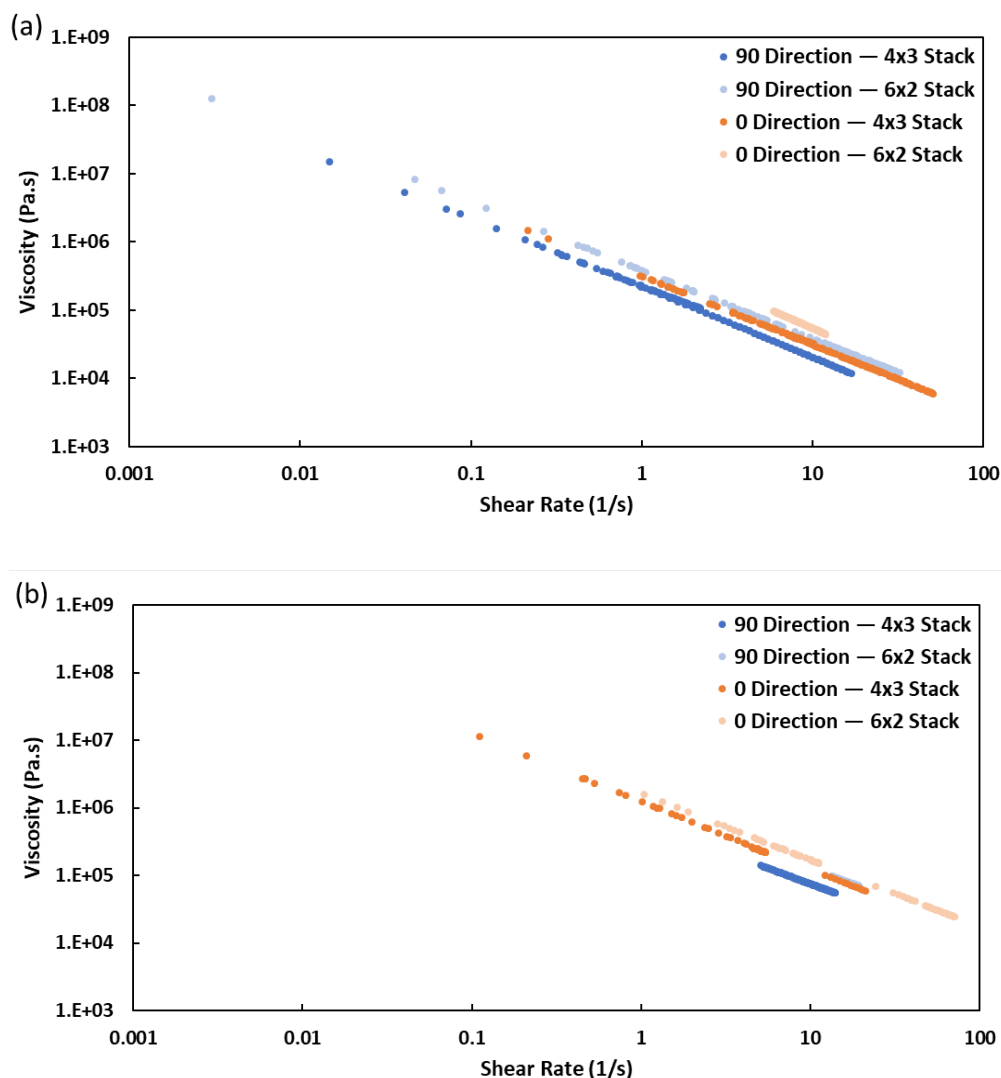


**Figure 5-7: Summary of press viscosity at all tested conditions (a) 300 °C and (b) 260 °C**

Shear thinning press viscosity of the material has been characterized. The captured shear rate range varies from test to test. This is due to different portions of raw data sets available for estimation. As was mentioned in section 5.2, only smooth portions of the raw data sets (e.g. Figure 5-3) can be analyzed. Several tests generated extremely noisy data sets, thus provided relatively shorter usable portion, and consequently narrower

shear rate range. However, most of the tests were able to capture press viscosity in a wide range ( $0.1$  to  $100 \text{ s}^{-1}$ ). This also indicates that observed shear rates can span a significant range during the flowing phase of compression molding. For the same type of stack, the press viscosity of the charge in the  $0$  degree direction is noticeably higher than the press viscosity in the  $90$  degree direction. This phenomenon is observed at both  $260^\circ\text{C}$  and  $300^\circ\text{C}$ . It can be explained by uneven fiber orientation distribution in the two directions (section 4.1). Interestingly, stack type is found to also impact the apparent press viscosity of the charge. It can be seen in Figure 5-7 that the press viscosity of a 6x2 stack charge is obviously higher than that of a 4x3 stack charge, which is true for both directions and both test temperatures. This is possibly caused by another mechanism often characterized in forming process of thermoplastic sheets — inter-ply friction [29]. There are 5 frictional interfaces in a 6x2 stack, whereas only 3 frictional interfaces in a 4x3 stack (Figure 5-8). More frictional interfaces may have added additional resistance to the flow of charge, and appeared as greater press viscosity in this experiment. Practically, this finding suggests that using fewer thicker layers in a stacked charge may be a better option for compression molding of GMT sheets.

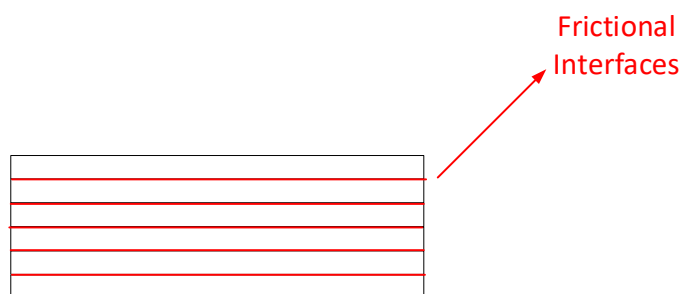


**Figure 5-8: Frictional interfaces in a 6x2 (6-layer) stack**

Temperature dependency of press viscosity is another important aspect to study. The press viscosity was found to decrease at higher temperatures, which is reasonable for thermoplastic composites. The temperature dependency is presented in Figure 5-9.

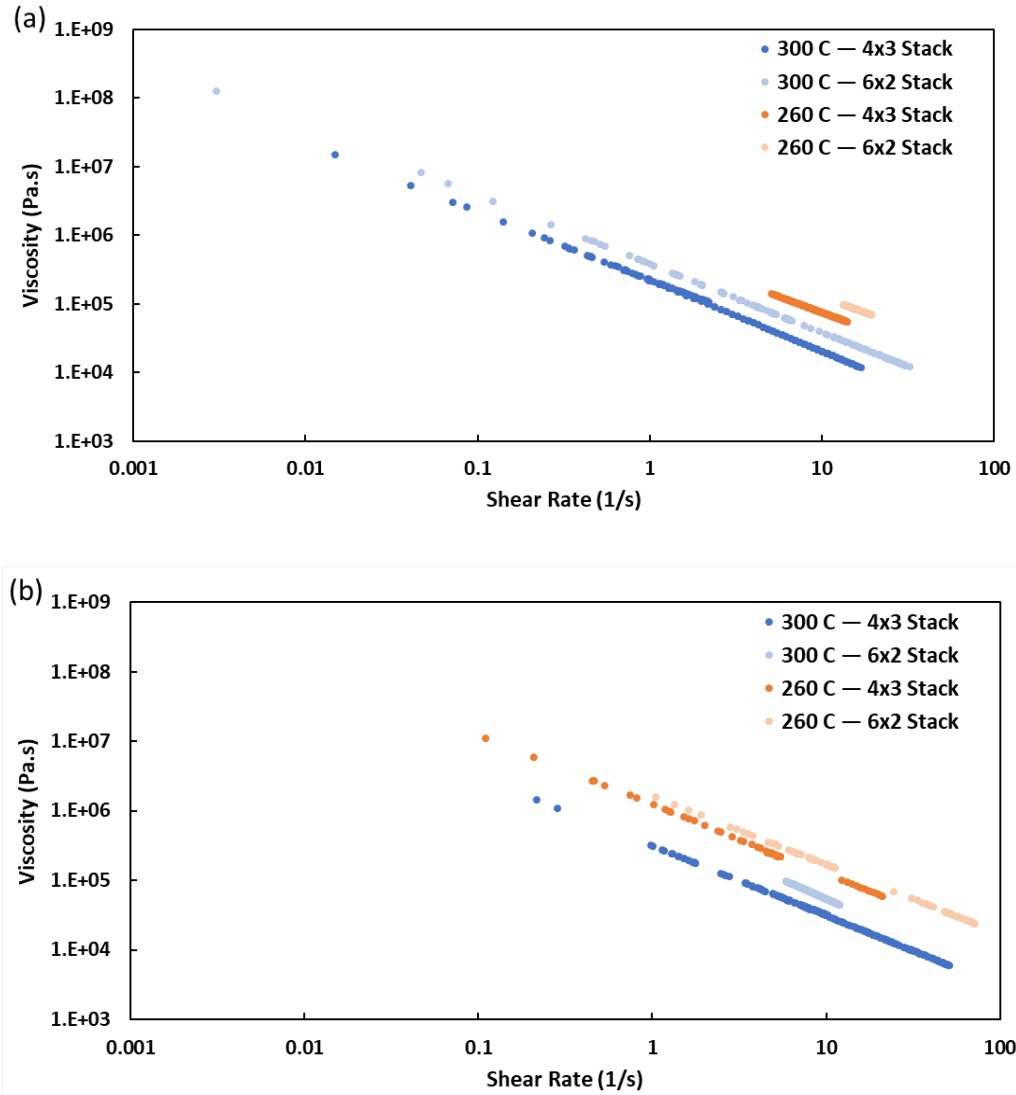


**Figure 5-9: Temperature dependency of press viscosity (a) 90 direction (b) 0 direction**

## 5.4 Generation of Materials Cards

The press viscosity can be used as an input of flow simulation. Creating property sets for both 90 and 0 directions allows capturing anisotropic material behavior in the simulation. On the other hand, property sets for different stack types provide options to choose from depending on the case (e.g. simulating a 6x2 stack or simulating a 4x3 stack). Therefore, a material card was generated for each combination of the direction and stack type. As was mentioned in Chapter 4, materials cards are typically created by fitting data to

viscosity models, then getting the model parameters. To also include the temperature effect, a temperature dependent power-law model was selected here for the press viscosity data. The model is given below:

$$\eta = \eta_0 \cdot (\dot{\gamma})^{n-1} \quad (5.5)$$

Here  $\dot{\gamma}$  is the shear rate,  $\eta$  is the viscosity and  $n$  is the flow index.  $\eta_0$  is the flow consistency index which involves temperature dependency:

$$\eta_0 = B \cdot \exp\left(\frac{T_b}{T}\right) \quad (5.6)$$

In equations 5.5 and 5.6,  $n$ ,  $B$  and  $T_b$  are model parameters to be fitted. More specifically,  $T_b$  determines temperature dependency,  $B$  determines the overall magnitude of viscosity values and  $n$  controls the shear rate dependency. As was discussed, several tests generated viscosity values over narrow shear rate ranges. When fitting the power-law model, this reduces the reliability of fitted parameters. 0 direction and 4x3 stack is the only combination that created broad shear rate ranges at both two test temperatures (260 °C and 300 °C). Therefore, the parameters fitted for this combination is of most statistical confidence. All other combinations of direction and stack type have at least one set of shear rate data being too narrow in range. Fittings were still performed for these combinations. However, the fitted parameters here should be considered less reliable. The fitted curve for 4x3 stack in 0 direction is plotted in Figure 5-10, including an extrapolation at 280 °C. All the fitted parameters are summarized in table 5-2. In the table, it can be seen that  $n$  values are around 0 in all the test conditions. In some conditions, the values are even slightly negative. Normally, it is not physically possible to create materials with negative  $n$  values. However, from a simulation point of view, this could simply represent very rapid drop of the bulk charge viscosity with increasing shear rate. The value of  $T_b$  varies slightly around 10000 K with different stacking types and flow directions. This suggests that temperature dependency of press viscosity is not impacted by the two factors. The value of  $B$ , however, is more sensitive to stacking types and flow directions. For example, the  $B$  value for 6x2 stack is around 3 times higher than that for 4x3 stack in the 90 direction.

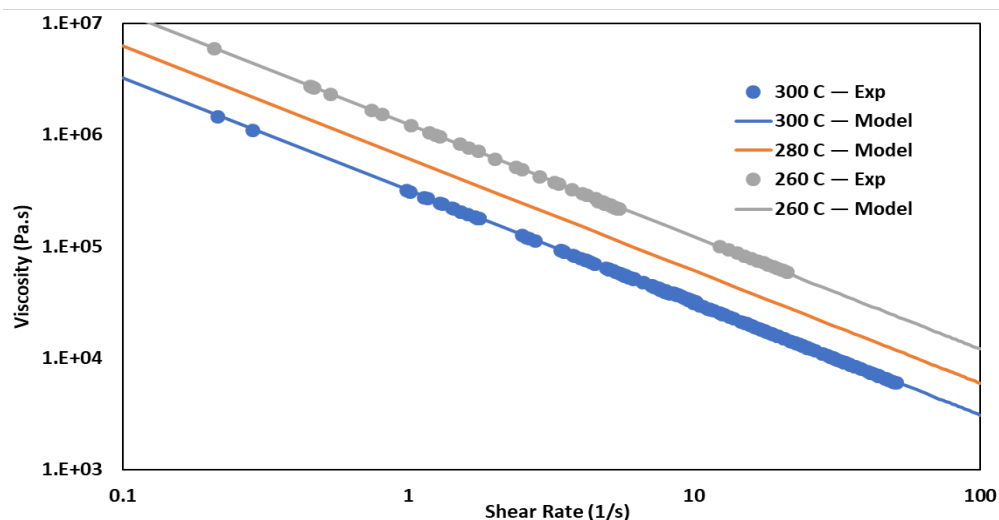


**Figure 5-10: Fitted power-law curves for 4x3 stack charge in 90 direction**

**Table 5-2: Fitted power-law parameters for all stack types and flow directions**

	90 Direction		0 Direction	
	4x3 Stack	6x2 Stack	4x3 Stack	6x2 Stack
<b><math>n</math> (-)</b>	-0.0225	0.00298	-0.00705	0.005414
<b><math>B</math> (Pa·s)</b>	0.00976	0.0265	0.00440	0.175
<b><math>T_b</math> (K)</b>	9705	9449	10371	8568.943

## 5.5 Conclusions

In this chapter, a squeeze flow method was adopted to characterize the apparent viscosity of Tepex Flowcore under flowing state. A hydraulic press and a plaque mold were used to squeeze the 1-D flow of stacked charges. The corresponding press force, press speed, and ram position (gap distance) were recorded and used for viscosity estimation. It was found that the press viscosity differs in 90 and 0 directions possibly due to uneven fiber orientation distribution. Stacking type was another fact that affect press viscosity. The 6x2 stack charges generally presented higher viscosity than the 4x3 stack charges. This could suggest stacking with less layers when preparing charges for actual compression



molding. In addition, temperature dependency of the press viscosity was captured. The experimental results were fitted to a temperature dependent power-law model. Model parameters were obtained for each combination of stacking type and flow orientation. However, due to data quality issues, only the parameters fitted from 4x3 stack in 0 direction can be considered reliable. The parameters for other combinations are questionable in reliability. Further experiments should be performed to repeat these test conditions, creating more shear rate data points which allows better fittings. Another possible issue with the method was the isothermal assumption, which could over-estimate viscosity values when charges actually lost heat to the mold, forming pronounced temperature profiles, e.g. studies in Chapter 3. Furthermore, the current power law model can be modified to include the effect of flow direction and stacking type (e.g. decompose  $B$  into more parameters to describe these dependency). Such way, a single parameter set can be obtained rather than the multiple parameter sets presented in section 5.4.

## Chapter 6

### 6 Conclusions and Future Work

A model-fitting approach was developed to characterize important heat transfer parameters during compression molding of GMT sheets. The estimated parameters, when applied in a 1-D conduction model, can accurately predict through-thickness charge temperature profile at process stage. The method could also be applied on other sheet-like thermoplastic composites in the case of compression molding. For flat sheets, heat transfer at the top and bottom surfaces is the main point of interest. However, when it comes to bulk charges (such as cubic geometry), a 3-D conduction model must be used and the heat transfer at side-walls must also be characterized. This can be an important perspective of future work.

A torsion bar set-up on rotational rheometer was used to characterize the draping behavior of selected GMT material. By using the LAOS data interpretation method [50], viscoelastic parameters were characterized. The parameters can be applied in simulating the draping phase of compression molding. This study, however, only focused on intra-ply shear mechanism. When GMT sheets are stacked, the frictional behavior between plies should also be considered. Future works could be characterizing the coefficient of friction between molten state GMT sheets.

The flow behavior of a stacked GMT charge was characterized with a 1-D squeeze flow method. Apparent press viscosity was estimated, which can be applied in flow simulations. An interesting finding was the effect of stack layer number on press viscosity. Current hypothesis for the cause is the different number of frictional interfaces between stack layers. However, this would require further investigation and validation. Furthermore, the current power-law model for fitting viscosity data can be modified to include impact of stack layer number and flow orientation.

## References

- [1] A. C. Long, *Composites forming technologies*. Elsevier, 2014.
- [2] D. G. Baird and D. I. Collias, *Polymer processing: principles and design*. John Wiley & Sons, 2014.
- [3] P. Dumont, L. Orgéas, D. Favier, P. Pizette, and C. Venet, “Compression moulding of SMC: In situ experiments, modelling and simulation,” *Compos. Part A Appl. Sci. Manuf.*, vol. 38, no. 2, pp. 353–368, 2007.
- [4] B. A. Davis and P. J. Gramann, *Compression molding*. Hanser Verlag, 2003.
- [5] D. Dörr, R. Gergely, S. Ivanov, L. Kärger, F. Henning, and A. Hrymak, “On the Applicability of Thermoforming Characterization and Simulation Approaches to Glass Mat Thermoplastic Composites,” *Procedia Manuf.*, vol. 47, pp. 118–125, 2020.
- [6] M. Chy, “Estimation and Control of Plastic Temperature in Heating Phase of Thermoforming Process,” McGill University Libraries, 2014.
- [7] J. E. Cunningham, P. F. Monaghan, and M. T. Brogan, “Predictions of the temperature profile within composite sheets during pre-heating,” *Compos. Part A Appl. Sci. Manuf.*, vol. 29, no. 1–2, pp. 51–61, 1998.
- [8] A. Bendada, A. Derdouri, M. Lamontagne, and Y. Simard, “Analysis of thermal contact resistance between polymer and mold in injection molding,” *Appl. Therm. Eng.*, vol. 24, no. 14–15, pp. 2029–2040, 2004.
- [9] S. Hong, J. Kang, and K. Yoon, “Correlation between thermal contact resistance and filling behavior of a polymer melt into multiscale cavities in injection molding,” *Int. J. Heat Mass Transf.*, vol. 87, pp. 222–236, 2015.
- [10] S. C. Somé, D. Delaunay, J. Faraj, J.-L. Bailleul, N. Boyard, and S. Quilliet, “Modeling of the thermal contact resistance time evolution at polymer--mold

interface during injection molding: Effect of polymers' solidification," *Appl. Therm. Eng.*, vol. 84, pp. 150–157, 2015.

- [11] M. Babenko, J. Sweeney, P. Petkov, F. Lacan, S. Bigot, and B. Whiteside, "Evaluation of heat transfer at the cavity-polymer interface in microinjection moulding based on experimental and simulation study," *Appl. Therm. Eng.*, vol. 130, pp. 865–876, 2018.
- [12] D. Kugele, J. Rausch, P. Müller, L. Kärger, and F. Henning, "Temperature Distribution in Thickness Direction of Thermoplastic Laminates During Thermoforming," in *Proceedings International Conference of Automotive Composites (IAUTOOC 2016)*, Lissabon, 2016.
- [13] K. Kouwonou, X. T. Pham, and G. Lebrun, "Modeling and characterization of thermoplastic composites peek/carbon," in *The 19th international conference on composite materials*, 2013.
- [14] Y. Song *et al.*, "A Novel CAE Method for Compression Molding Simulation of Carbon Fiber-Reinforced Thermoplastic Composite Sheet Materials," *J. Compos. Sci.*, vol. 2, no. 2, p. 33, 2018.
- [15] F. N. Cogswell, "The experience of thermoplastic structural composites during processing," *Compos. Manuf.*, vol. 2, no. 3–4, pp. 208–216, 1991.
- [16] S. G. Advani, *Flow and rheology in polymer composites manufacturing*, vol. 10. Elsevier science, 1994.
- [17] S. P. Haanappel and R. Akkerman, "Shear characterisation of uni-directional fibre reinforced thermoplastic melts by means of torsion," *Compos. Part A Appl. Sci. Manuf.*, vol. 56, pp. 8–26, 2014.
- [18] U. Sachs *et al.*, "Characterization of the dynamic friction of woven fabrics: experimental methods and benchmark results," *Compos. Part A Appl. Sci. Manuf.*, vol. 67, pp. 289–298, 2014.

- [19] D. J. Groves, "A characterization of shear flow in continuous fibre thermoplastic laminates," *Composites*, vol. 20, no. 1, pp. 28–32, 1989.
- [20] D. J. Groves and D. M. Stocks, "Rheology of thermoplastic-carbon fibre composite in the elastic and viscoelastic states," *Compos. Manuf.*, vol. 2, no. 3–4, pp. 179–184, 1991.
- [21] A. B. Wheeler and R. S. Jones, "A characterization of anisotropic shear flow in continuous fibre composite materials," *Compos. Manuf.*, vol. 2, no. 3–4, pp. 192–196, 1991.
- [22] G. B. McGuinness and C. M. ÓBrádaigh, "Characterisation of thermoplastic composite melts in rhombus-shear: the picture-frame experiment," *Compos. Part A Appl. Sci. Manuf.*, vol. 29, no. 1–2, pp. 115–132, 1998.
- [23] W. F. Stanley and P. J. Mallon, "Intraply shear characterisation of a fibre reinforced thermoplastic composite," *Compos. Part A Appl. Sci. Manuf.*, vol. 37, no. 6, pp. 939–948, 2006.
- [24] U. Sachs and R. Akkerman, "Viscoelastic bending model for continuous fiber-reinforced thermoplastic composites in melt," *Compos. Part A Appl. Sci. Manuf.*, vol. 100, pp. 333–341, 2017.
- [25] D. Dörr, F. Henning, and L. Kärger, "Nonlinear hyperviscoelastic modelling of intra-ply deformation behaviour in finite element forming simulation of continuously fibre-reinforced thermoplastics," *Compos. Part A Appl. Sci. Manuf.*, vol. 109, pp. 585–596, 2018.
- [26] R. Scherer and K. Friedrich, "Inter-and intraply-slip flow processes during thermoforming of CF/PP-laminates," *Compos. Manuf.*, vol. 2, no. 2, pp. 92–96, 1991.
- [27] A. M. Murtagh, J. J. Lennon, and P. J. Mallon, "Surface friction effects related to pressforming of continuous fibre thermoplastic composites," *Compos. Manuf.*, vol. 6, no. 3–4, pp. 169–175, 1995.

- [28] U. Sachs, *Friction and bending in thermoplastic composites forming processes*. University of Twente, 2014.
- [29] R. Akkerman, R. Ten Thije, U. Sachs, and M. De Rooij, “Friction in textile thermoplastic composites forming,” in *Proceedings of the 10th international conference on textile composites-TEXCOMP*, 2010, vol. 10, pp. 271–279.
- [30] A. C. Caba, “Characterization of carbon mat thermoplastic composites: flow and mechanical properties,” Virginia Tech, 2005.
- [31] G. Kotsikos, J. H. Bland, A. G. Gibson, and H. W. Chandler, “Squeeze flow testing of glass mat thermoplastic material,” *Compos. Part A Appl. Sci. Manuf.*, vol. 27, no. 12, pp. 1195–1200, 1996.
- [32] G. Kotsikos and A. G. Gibson, “Investigation of the squeeze flow behaviour of sheet moulding compounds (SMC),” *Compos. Part A Appl. Sci. Manuf.*, vol. 29, no. 12, pp. 1569–1577, 1998.
- [33] M. A. Dweib and C. M. ÓBrádaigh, “Extensional and shearing flow of a glass-mat-reinforced thermoplastics (GMT) material as a non-Newtonian viscous fluid,” *Compos. Sci. Technol.*, vol. 59, no. 9, pp. 1399–1410, 1999.
- [34] T. G. Rogers, “Rheological characterization of anisotropic materials,” *Composites*, vol. 20, no. 1, pp. 21–27, 1989.
- [35] G. Kotsikos, J. H. Bland, and A. G. Gibson, “Rheological characterization of commercial glass mat thermoplastics (GMTs) by squeeze flow testing,” *Polym. Compos.*, vol. 20, no. 1, pp. 114–123, 1999.
- [36] T. S. Lundström and A. Holmgren, “Dissolution of voids during compression molding of SMC,” *J. Reinf. Plast. Compos.*, vol. 29, no. 12, pp. 1826–1837, 2010.
- [37] M. Hohberg, L. Kärger, F. Henning, and A. Hrymak, “Rheological measurements and rheological shell model Considering the compressible behavior of long fiber reinforced sheet molding compound (SMC),” *Compos. Part A Appl. Sci. Manuf.*,

vol. 95, pp. 110–117, 2017.

- [38] M. Hohberg, L. Kärger, D. Bücheler, and F. Henning, “Rheological in-mold measurements and characterizations of sheet-molding-compound (SMC) formulations with different constitution properties by using a compressible shell model,” *Int. Polym. Process.*, vol. 32, no. 5, pp. 659–668, 2017.
- [39] H. Lessard, G. Lebrun, A. Benkaddour, and X.-T. Pham, “Influence of process parameters on the thermostamping of a [0/90] 12 carbon/polyether ether ketone laminate,” *Compos. Part A Appl. Sci. Manuf.*, vol. 70, pp. 59–68, 2015.
- [40] D. Kugele *et al.*, “Modeling of the non-isothermal crystallization kinetics of polyamide 6 composites during thermoforming,” in *AIP Conference Proceedings*, 2017, vol. 1896, no. 1, p. 30005.
- [41] M. N. Ozisick, “Heat transfer: a basic approach,” *Raleigh: MCGraw-Hill*, 1985.
- [42] B. G. Compton, B. K. Post, C. E. Duty, L. Love, and V. Kunc, “Thermal analysis of additive manufacturing of large-scale thermoplastic polymer composites,” *Addit. Manuf.*, vol. 17, pp. 77–86, 2017.
- [43] D. L. James and W. Z. Black, “Thermal analysis of continuous filament-wound composites,” *J. Thermoplast. Compos. Mater.*, vol. 9, no. 1, pp. 54–75, 1996.
- [44] X. Li and W. Strieder, “Emissivity of high-temperature fiber composites,” *Ind. Eng. Chem. Res.*, vol. 48, no. 4, pp. 2236–2244, 2009.
- [45] T. Okada, R. Ishige, and S. Ando, “Analysis of thermal radiation properties of polyimide and polymeric materials based on ATR-IR spectroscopy,” *J. Photopolym. Sci. Technol.*, vol. 29, no. 2, pp. 251–254, 2016.
- [46] J. Faraj, B. Pignon, J. L. Bailleul, N. Boyard, D. Delaunay, and G. Orange, “Heat transfer and crystallization modeling during compression molding of thermoplastic composite parts,” in *Key Engineering Materials*, 2015, vol. 651, pp. 1507–1512.

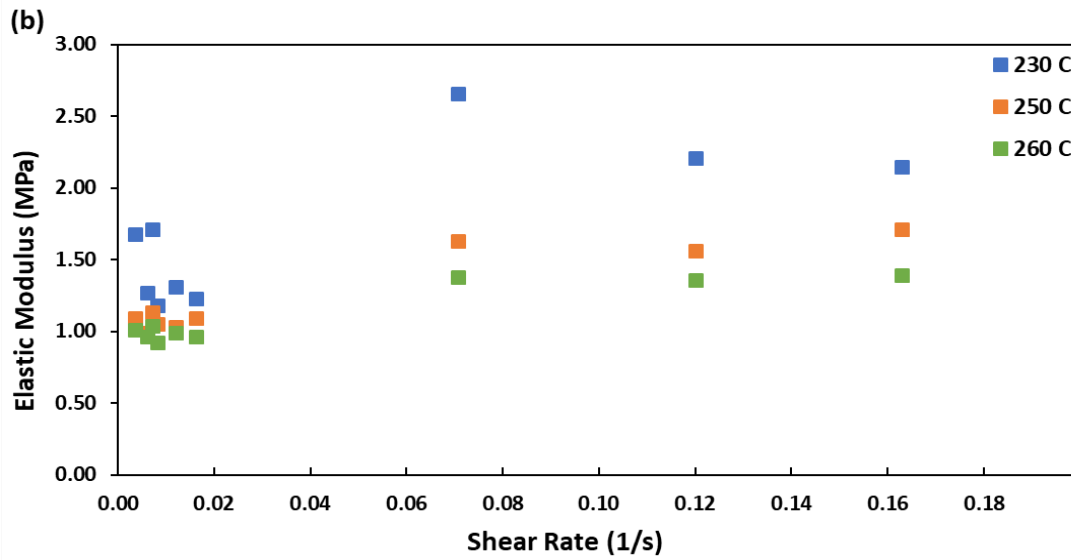
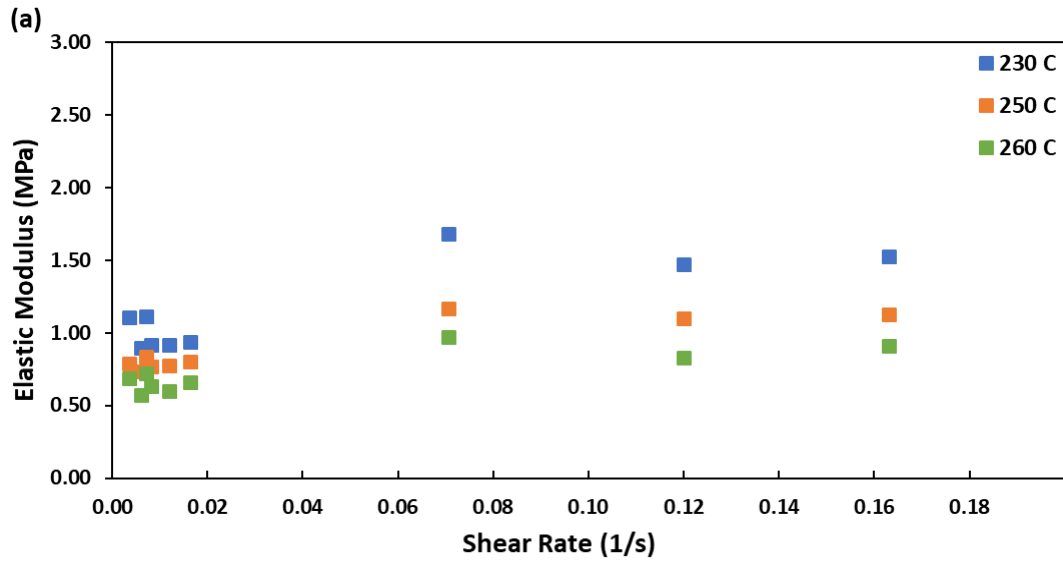
- [47] D. Dörr, T. Joppich, D. Kugele, F. Henning, and L. Kärger, “A coupled thermomechanical approach for finite element forming simulation of continuously fiber-reinforced semi-crystalline thermoplastics,” *Compos. Part A Appl. Sci. Manuf.*, vol. 125, p. 105508, 2019.
- [48] X. Yu, L. Zhang, and Y.-W. Mai, “Modelling and finite element treatment of intraply shearing of woven fabric,” *J. Mater. Process. Technol.*, vol. 138, no. 1–3, pp. 47–52, 2003.
- [49] A. Margossian, S. Bel, and R. Hinterhoelzl, “Bending characterisation of a molten unidirectional carbon fibre reinforced thermoplastic composite using a Dynamic Mechanical Analysis system,” *Compos. Part A Appl. Sci. Manuf.*, vol. 77, pp. 154–163, 2015.
- [50] R. H. Ewoldt, A. E. Hosoi, and G. H. McKinley, “New measures for characterizing nonlinear viscoelasticity in large amplitude oscillatory shear,” *J. Rheol. (N. Y. N. Y.)*, vol. 52, no. 6, pp. 1427–1458, 2008.
- [51] J. M. Dealy and K. F. Wissbrun, *Melt rheology and its role in plastics processing: theory and applications*. Springer Science & Business Media, 2012.
- [52] R. B. Bird, R. C. Armstrong, and O. Hassager, “Dynamics of polymeric liquids. Vol. 1: Fluid mechanics,” 1987.
- [53] K. Atalik and R. Keunings, “On the occurrence of even harmonics in the shear stress response of viscoelastic fluids in large amplitude oscillatory shear,” *J. Nonnewton. Fluid Mech.*, vol. 122, no. 1–3, pp. 107–116, 2004.
- [54] K. S. Cho, K. Hyun, K. H. Ahn, and S. J. Lee, “A geometrical interpretation of large amplitude oscillatory shear response,” *J. Rheol. (N. Y. N. Y.)*, vol. 49, no. 3, pp. 747–758, 2005.
- [55] K. S. Gandhi and R. Burns, “Rheological Properties of Glass Fiber-Reinforced Dough Molding Compounds,” *Trans. Soc. Rheol.*, vol. 20, no. 4, pp. 489–502, 1976.



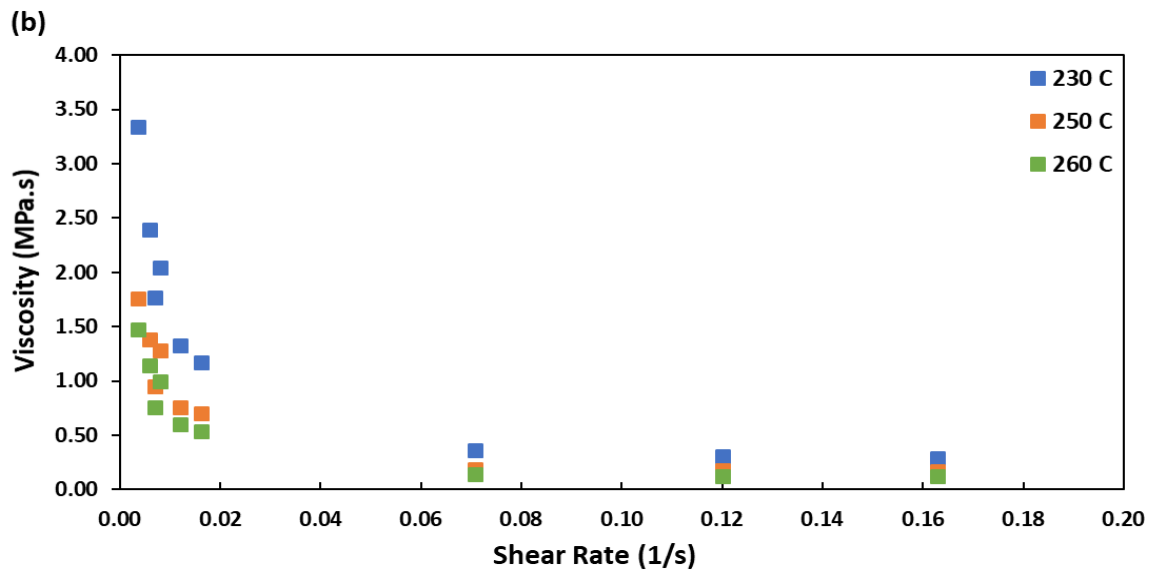
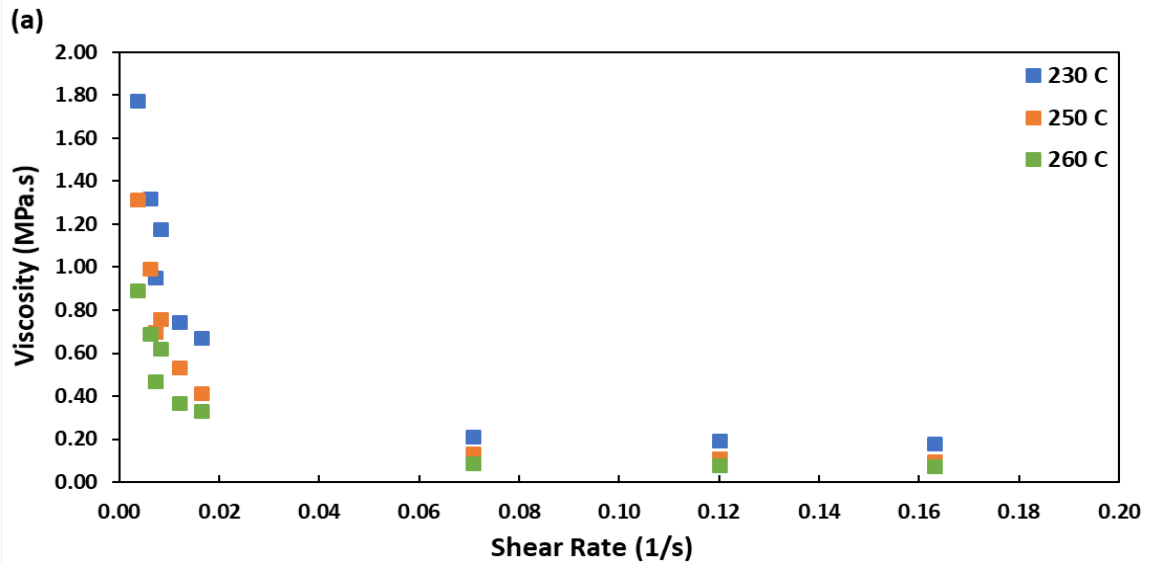
- [56] T. Osswald and N. Rudolph, “Polymer rheology,” *Carl Hanser, München*, 2015.
- [57] M. Kalaidov *et al.*, “Viscosity Measurement Technique for Long Fiber Thermoplastic Material,” in *SPE ACCE Proceedings*, 2019.
- [58] H. Mavridis, A. N. Hrymak, and J. Vlachopoulos, “The effect of fountain flow on molecular orientation in injection molding,” *J. Rheol. (N. Y. N. Y.)*, vol. 32, no. 6, pp. 639–663, 1988.
- [59] M. R. Kamal, S. K. Goyal, and E. Chu, “Simulation of injection mold filling of viscoelastic polymer with fountain flow,” *AIChE J.*, vol. 34, no. 1, pp. 94–106, 1988.
- [60] H. Mavridis, G. D. Bruce, G. J. Vancso, G. C. Weatherly, and J. Vlachopoulos, “Deformation patterns in the compression of polypropylene disks: experiments and simulation,” *J. Rheol. (N. Y. N. Y.)*, vol. 36, no. 1, pp. 27–43, 1992.

## Appendices

### Appendix A: Temperature dependency (normal scale) of elastic modulus characterized from torsion bar (a) 90 direction and (b) 0 direction



**Appendix B: Temperature dependency (normal scale) of viscosity characterized from torsion bar (a) 90 direction and (b) 0 direction**



## Curriculum Vitae

<b>Name:</b>	Cheng Xu
<b>Post-secondary Education and Degrees:</b>	University of Western Ontario London, Ontario, Canada 2013-2017 B.E.Sc. Chemical Engineering  University of Western Ontario London, Ontario, Canada 2017-2020 M.E.Sc.
<b>Honours and Awards:</b>	Dean's Honour List 2015-2016
<b>Related Work Experience</b>	Teaching Assistant University of Western Ontario 2018-2019